AD-A253 686

ADVANCED WAVEFORM RESEARCH METHODS
FOR GERESS RECORDINGS

H.P. Harjes
N. Gestermann
M. Jost
J. Schweitzer
J. Wuster

Ruhr-University-Bochum
D-4630 Bochum
FEDERAL REPUBLIC OF GERMANY

15 April 1992

DTIC
ELECTE
JUL 15 1992
S   D

Scientific Report No. 2

APPROVED FOR PUBLIC RELEASE; DISTRIBUTION UNLIMITED
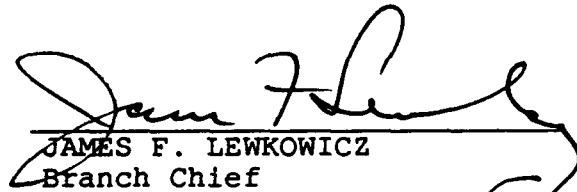
92-18415

SPONSORED BY
Defense Advanced Research Projects Agency
Nuclear Monitoring Research Office, and
Defense Sciences Office
ARPA ORDER NO 7847

MONITORED BY
Phillips Laboratory
AFOSR-90-0189

The views and conclusions contained in this document are those of the authors and should not be interpreted as representing the official policies, either expressed or implied, of the Defense Advanced Research Projects Agency or the U.S. Government.

This technical report has been reviewed and is approved for publication.

JAMES F. LEWKOWICZ
Contract Manager
Solid Earth Geophysics Branch
Earth Sciences Division

JAMES F. LEWKOWICZ
Branch Chief
Solid Earth Geophysics Branch
Earth Sciences Division

DONALD H. ECKHARDT, Director
Earth Sciences Division

REPORT DOCUMENTATION PAGE

Form Approved
OMB No. 0704-0188

1. AGENCY USE ONLY *(Leave blank)*	2. REPORT DATE 15 April 1992	3. REPORT TYPE AND DATES COVERED Scientific No. 2

4. TITLE AND SUBTITLE
Advanced Waveform Research Methods for GERESS Recordings

5. FUNDING NUMBERS
PE 62714E
PR 9A10   TA DA   WU AE

AFOSR-90-0189

6. AUTHOR(S)
H.P. Harjes   J. Schweitzer
N. Gestermann   J. Wuster
M. Jost

7. PERFORMING ORGANIZATION NAME(S) AND ADDRESS(ES)
Ruhr-University-Bochum
D-4630 Bochum
FEDERAL REPUBLIC OF GERMANY

8. PERFORMING ORGANIZATION REPORT NUMBER

9. SPONSORING/MONITORING AGENCY NAME(S) AND ADDRESS(ES)
Phillips Laboratory
Hanscom AFB, MA 01731-5000

Contract Manager: James Lewkowicz/GPEH

10. SPONSORING/MONITORING AGENCY REPORT NUMBER

PL-TR-92-2142

11. SUPPLEMENTARY NOTES

12a. DISTRIBUTION/AVAILABILITY STATEMENT

APPROVED FOR PUBLIC RELEASE; DISTRIBUTION UNLIMITED

12b. DISTRIBUTION CODE

13. ABSTRACT *(Maximum 200 words)*

The GERESS array project is a cooperative research program, jointly undertaken by Southern Methodist University Dallas (USA) and Ruhr-University Bochum in Germany. It is part of a multi-array network which includes NORESS, ARCESS, and FINESA in Scandinavia. This report summarizes research activities carried out at the data center in the Institute of Geophysics in Bochum during 1991.

The GERESS array became fully operational in January 1991. Data are continuously transmitted from the array hub in Bavaria to NORSAR and to Bochum via 64 kbit lines. In Bochum, an experimental on-line processing system, based on RONAPP, is operated to monitor data quality and initiate necessary maintenance activities. Since July 1991, the on-site maintenance of the array is also overtaken by Ruhr-University as part of the research grant. The monthly uptime of the array varied between 88.4% and 99.7% with an average of 94.9%. At the data center in Bochum, an automatic event bulletin - interactively reviewed by an analyst - is produced and widely distributed to interested institutions.

14. SUBJECT TERMS
GERESS   FINESA
NORESS   Teleseismic seismicity
ARCESS   Geotectonic environment

15. NUMBER OF PAGES
148

16. PRICE CODE

17. SECURITY CLASSIFICATION OF REPORT Unclassified	18. SECURITY CLASSIFICATION OF THIS PAGE Unclassified	19. SECURITY CLASSIFICATION OF ABSTRACT Unclassified	20. LIMITATION OF ABSTRACT SAR

After one year of operation it is found that GERESS is the most sensitive station in Central Europe for monitoring local, regional, and teleseismic seismicity. During the GSETT-2 experiment, which was conducted by the Geneva experts group during the time period from April 22 to June 2 1991, GERESS located on average 16 regional events and detected 12 teleseismic events daily. Within the 6 weeks of GSETT-2, GERESS reported 3275 phases to the international data centers.

Following a similar study at NORSAR, an evaluation of the P-wave detectability was undertaken for GERESS. In the frequency range between 1 Hz and 3 Hz the full GERESS array reaches a higher SNR gain than expected by $\sqrt{N}$. In the same frequency range, the SNR gain is also higher than at NORESS. GERESS shows a SNR gain similar to NORESS in the frequency band from 3 Hz to 6 Hz. At higher frequencies, the SNR gain at GERESS is significantly lower than at NORESS. The differences in P-wave detectability, observed at GERESS and NORESS, clearly correlate with the noise characteristics at both array sites.

In contrast to the regional arrays in Scandinavia, GERESS is located in a complex geotectonic environment. The Alpine-Mediterranean earthquake belt to the South or the Tornquist-Teisseyre (TTL) suture to the Northeast are prominent examples. As a consequence, regional phases show remarkable azimuthal variation. A study of the regional characteristics reveals that L_g and S_n are the most sensitive phases to separate the different propagation paths. In addition, the blocking effect of structures like the TTL suture has to be taken into account in the design of future regional monitoring networks.

Finally, this report contains a discrimination study between earthquakes and quarry blasts. In the Vogtland area about 180 km NW of GERESS natural and artificial seismicity is co-located. Both sources produce significantly different seismograms at GERESS. The source effect can be seen in the amplitude ratios of P-waves and in the frequency content of S-waves as well as in the excitation of surface waves. In a joint discrimination scheme, an effective separation of both populations, earthquakes and quarries, is achieved.

TABLE OF CONTENTS

page

1. GERESS STATUS REPORT

April 1991 - February 1992

Michael L. Jost

1.1 General

The German Experimental Regional Seismic System (GERESS) is a cooperative research program of Southern Methodist University Dallas, Texas, and Ruhr-University Bochum, Germany. It is an extension of the Scandinavian regional array network, i. e., NORESS, ARCESS, and FINESA, into Central Europe. The GERESS array is located in the Bavarian Forest area at the southeastern part of Germany near the border to Austria and Czechoslovakia (Harjes, 1990). The array consists of 25 stations with vertical-component short-period Teledyne Geotech GS-13 instruments sampled at 40 Hz. In addition, four of the sites include horizontal component instruments. At the key station of the array, GEC2 (48.84511 N, 13.70156 E, 1132 m), there is a supplemental three-component set of GS-13's sampled at 120 Hz and a three-component set of broad-band seismometers (Teledyne Geotech BB-13) sampled at 10 Hz. The geometry of the array is based on concentric rings providing an overall aperture of about 4 km. The array became fully operational in January 1991. Data from the array are continuously transmitted to NORSAR and to the Department of Geophysics, Ruhr-University Bochum via 64 kbit telephone lines. The data flow is displayed in Figure 1-1.

1.2 GERESS Observatory at Ruhr-University Bochum

The Department of Geophysics of Ruhr-University Bochum operates an experimental on-line processing system for GERESS data. This system uses software developed at NORSAR (Mykkeltveit and Bungum, 1984; Fyen, 1987) and continuously improved at Bochum. During the Group of Scientific Experts Technical Test 2 (GSETT-2), numerous updates to the program package were implemented.

The on-line processing consists of 3 steps: detection, fk-analysis, and location. The first stage of the on-line processing accesses data in 30 second segments and runs a STA/LTA detector. The detector presently recognizes an onset if the STA/LTA ratio for a filtered trial-beam exceeds a threshold of 4. Figure 1-2 shows the beams currently used for the on-line data processing at Bochum. The next step of the on-line processing is the transformation of a 3 second filtered data segment at each onset time (derived from the detection time) into the frequency-wavenumber domain. As a result, the slowness and back-azimuth of the phase is determined. From the slowness information, seismic phases are identified. The final step of the on-line data processing is

the location of events. The seismic phases as identified in the fk-analysis are associated to events in this step. From the arrival time difference of regional phases, the distance to the epicenter can be determined from the Jeffreys - Bullen travel time tables for regional seismic phases. Together with a mean back-azimuth, the epicenter locations of local and regional events are determined.

In the period covered in this report, 15 events have been automatically located each day on average (Table 1-1). At Bochum, local magnitudes are calculated by the following procedure (the algorithm was implemented by J. Schweitzer):
1) Determination of the optimum S-phase beam.
2) High-pass filter at 0.7 Hz.
3) Transformation of beam-trace to a Wood-Anderson record.
4) Picking of maximum amplitude of the S-wavetrain and correction for epicentral distance (s. chapter 3, Fig. 3-5).
The ML magnitude distance correction from Gutenberg and Richter (1956) was changed following the procedure of Ebel (1982) using the attenuation relation for France from Nicolas et al. (1982).

Table 1-1

Statistics on the GERESS Bochum On-line Processing

	number	number/day
detections	56139	168
f-k analyses	52598	157
locations	5014	15

Since Sep. 1991, the results of the on-line processing have been sent to interested institutions via e-mail (e.g. Bundesanstalt für Geowissenschaften und Rohstoffe (BGR), Hungarian GSE Seismological Network, Frankfurt University, GRF, LJU, ORFEUS, Stuttgart University, Swiss GSE Seismological Network). In addition, the On-line Processing Display Manager (Jost, 1991) has been used by many scientists for near real time information on parameter data. Recently, a first version of the Data Request Manager (DRM) by Krake Inc. has been installed for trial operation. The DRM enables the transmission of data (GSE, SEED) and interfaces to the German Regional Network of Broadband Stations.

Since late October 1991, alert messages of strong teleseismic and regional events are automatically sent to NEIC (Golden, CO) in near real-time (Table 1-2). In addition, teleseismic events have been analyzed interactively, and parameter data such as onset time, amplitude, period, azimuth and slowness have been routinely sent to NEIC (Golden, CO).

Table 1-2

Number of events for which GERESS sent automatic alert messages to NEIC (Golden, CO)

Month	Alerts
10/91	10
11/91	29
12/91	57
1/92	29
2/92	32

1.3 GERESS Array Hub

The GERESS array showed a significant improvement for the period covered in this report. Figure 1-3 shows the uptime of the system including the Bochum Observatory (uptimes directly correspond to the data archived in Bochum). The average uptime was 94.9 %. The highest uptime (99.7 %) was observed in January 1992; the lowest uptime (88.4 %) occurred in December 1991 due to analysis work at the IAC. In January and February 1991, significant outages were caused by the degrading acquisition workstation (SUN 3E) at Bochum. The Bochum data acquisition reached a high level of reliability after the SUN-4 based data acquisition system came on-line (February 26, 1991). The technical status of GERESS is summarized in chronological order in Appendix 1-1 (monthly status reports are available upon request).

However, GERESS could not be considered fully acceptable for the period covered in this report. Major problems have been identified during the GERESS System Verification Test in mid September 1991. The detailed test evaluation by Golden et al. (1991) noted 4 significant deficiencies:

1) Data gaps are inherent in the IAC. The number of 1-second gaps per data channel were found to form 4 groups. These 4 groups correspond to the 4 communication boards (digiboards) on the array-controller (Table 1-3). The reason is that the digiboards perform sporadic self-resets, loosing about 9 seconds of data each time (Figure 1-4). Therefore, the overall data loss is significantly greater than the loss in data transmission as specified and observed by the German Telekom (1 bit in 10E+06).

2) The Remote Data Acquisition System (RDAS-200) connected to a BB-13 (sampled with 10 Hz) reports data 90 msec ahead of world time.

3) Documentation for operation and maintenance of the array is incomplete.

4) Water leakage is observed in the vaults of A3, C2A, C2B, C4, D3, and D5.

Minor problems of the GERESS installation include (Golden et al., 1991):
- the power distribution system cannot restart the complete array after a power outage of more than 15 minutes;

- there are 2 distinct populations of the RDAS showing a time skew bias of 800 microseconds, although the design specifications are met;
- the wind direction sensor is inoperative;
- the amount of memory in the Communication Interface Module (CIM) at Bochum is too small;
- the display software on the workstation at Bochum needs an upgrade.

On the other hand, the GERESS System Verification Test demonstrated good adherence to specifications with respect to noise floor, dynamic range, crosstalk, array synchronization (see discussion below), and seismometer response (except A2 and A3). The time jitter test was not performed to the specified precision due to a breakdown of the function generator.

Table 1-3

Number of 1 second data gaps averaged for a specific digiboard. Results of 4 tests are given (times were adjusted to a test duration of 241896 seconds).

digiboard	15 Dec 1991	18 Sep 91	5 June 91	15 Nov 90
1	409	522	176	274
2	511	1084	527	459
3	181	194	240	?
4	99	161	97	?

Based on the findings of the GERESS System Verification Test, Teledyne Geotech started corrective action under warranty. A specialist was sent (December 5-15) to investigate data gap problem. At Dallas, Teledyne Geotech has continued to work on this problem. For May 1992, a hardware (IAC) and software update (for IAC and RDAS-200) has been announced by Teledyne that is expected to solve the data gap problem

A software upgrade for the RDAS 200 has been provided by Teledyne Geotech that fixed the BB-13 desynchronization problem in March 1992

Teledyne Geotech sent some of the missing documentation The RDAS 200 technical reference manual as well as the IAC technical reference manual are expected to be available in summer 1992. Lahmeyer Inc , responsible for the vault construction, will start warranty repairs after the snow melt

From April to September 1991, several GERESS channels showed desynchronization varying from units of a second to fractions of a second The amount of desynchronization varied with time. Teledyne and our engineers found improper adjusted optical links between RDAS and IAC as the cause of the desynchronization In September, Teledyne corrected the optical links and all channels have remain... ...hronized when properly adjusted after ou......

It has been noted that the optical link is very sensitive to lightning damage due to destruction of repeaters which are connected to the DC power (e. g., June 24, 1991; July 12, 1991). This means that the optical links have to undergo maintenance work comparatively often. Since proper equipment to adjust these links is extremely expensive, the adjustment is usually done by trial and error. A deviation or drift from the optimum adjustment means that time synchronization pulses (1 pps signals) can be distorted, hence the synchronization of the array is fundamentally affected (e. g., Figure 1-5). For stable channel synchronization, possibilities to provide each RDAS with an independent time receiver should be investigated (f.e., low cost GPS receivers).

Ruhr-University has taken responsibility for GERESS maintenance. Starting from July 1991, our technicians succeeded in performing routine repairs on the RDAS, the optical links, and the IAC.

1.4 Conclusion

GERESS is the most sensitive seismological station in Central Europe as results of the GSETT-2 experiment demonstrate (J. Schweitzer, this report). In addition, the uptime of the GERESS system shows its high level of reliability.

The Bochum observatory routine included data archival and on-line analysis. The automatic locations of regional events render a good first solution, in general. Results of the interactive re-analysis of teleseismic data have been used by NEIC for the PDE. In addition, interested institutions have used parameter data of GERESS for their tasks. The Bochum observatory is an open station similar to the German Regional Network of Broad-band Stations.

On the other hand, GERESS could not be considered fully acceptable for the period covered in this report. Major problems have been identified during the GERESS System Verification Test in mid September 1991 (Golden et al., 1991).

1.5 Acknowledgements

I want to thank J. Schweitzer, N. Gestermann, N. Schnieders, B. Klotz, L. Kühne, and O. Richter for their support in the daily observatory routine.

1.6 Literature

Ebel, J. E. (1982). ML measurements for northeastern United States earthquakes, *Bull. Seism. Soc. Am.* **72**, 1367-1378.

Fyen, J. (1987). Improvements and Modifications, Semiannual Technical Summary, 1 October 1986 - 31 March 1987, NORSAR Sci. Rep. No. 2-86/87, Kjeller, Norway.

Golden, P., E. T. Herrin, and C. Hayward (1991). Development of an intelligent seismic facility and preparation for participation in the conference on disarmament group of scientific experts technical test. Results of the

GERESS verification test, Quarterly Technical Report SMU-R-91-152, Southern Methodist University, Dallas, Texas, 64 pp.

Gutenberg, B. and C. F. Richter (1956). Earthquake magnitude, intensity, energy, and acceleration (2. paper), *Bull. Seism. Soc. Am.* **46**, 105-145.

Harjes, H.-P. (1990). Design and siting of a new regional array in Central Europe, *Bull. Seism. Soc. Am.* **80**, 1801-1817.

Jost, M. L. (1991). The Bochum on-line processing display manager, in *Advanced Waveform Research Methods for GERESS Recordings*, DARPA Annual Report No. AFOSR-90-0189, 38-43. PL-TR-91-2134, ADA239199

Mykkeltveit, S. and H. Bungum (1984). Processing of regional seismic events using data from small-aperture arrays, *Bull. Seism. Soc. Am.* **74**, 2313-2333.

Nicolas, M., B. Massinon, P. Mechler, and M. Bouchon (1982). Attenuation of regional phases in Western Europe, *Bull. Seism. Soc. Am.* **72**, 2089-2106.

Teledyne Geotech (1991). System Verification Tests German Experimental Regional Seismic System, Document No. 990-58500-6101, Revision D, 22 August 1991, 49 pp.

Appendix 1-1: Chronological Status List GERESS

Apr. 1991: - Synchronization problems on D3 and D4.
- Crashes of IAC: 6 (instability of IAC follows distinct pattern: first, all channels on digiboard 3 stopped transmitting data. Second, all channels on digiboard 1 quit after several hours. Then, the remaining channels started sending unusable data).
- Data outages of several minutes in duration suspected to be caused by faulty PTM multiplexer of the German Telekom.
- Malfunction of the CIM at Bochum documented.
- Several ethernet failures caused data loss at Bochum.
- Participation in GSETT-2.

May 1991: - Synchronization problems on D3 and D7.
- Crashes of IAC: 6.
- On May 15, artificial data on C4 and D4.
- German Telekom continued testing communication lines.
- At Bochum, increase of the size of the circular buffer to hold 10 hours data.
- At Bochum, display problems documented, a fix from Science Horizons was promised.
- At Bochum, ethernet problems fixed by a SUN patch to the system kernel.
- Participation in GSETT-2.

June 1991: - Desynchronization of the BB-13 channels documented.
- Crashes of IAC: 4.
- 9-second gaps on all channels of a digiboard documented.
- Bochum engineers analyzed the 2 GERESS data streams (Bochum, NORSAR): these streams are not truly independent (there is a master and a slave cable). This may be the cause of the large amount of data gaps observed in NORSAR.
- German Telekom finished testing and repair of the communication lines.
- June 24, thunderstorm damage to the optical data link (repeater) at 9 stations.
- Installation of RDAS-200 software (version 2.3.1) and IAC software ("WAT-CHIAC").
- At Bochum, installation of command facility (ICI) (in cooperation with SHI).
- At Bochum, the circular buffer was increased to hold 16 hours data.
- At Bochum, reinstallation of on-line data analysis package after numerous updates had been implemented during the GSETT-2 experiment (location routine was based on Jeffreys Bullen tables).
- Installation of the on-line processing on a dedicated SUN-4 (4/75) workstation, provided by the BGR (German Federal Department of Geosciences and Natural Resources).
- Participation in GSETT-2.

July 1991: - Successful repair of lightning damages (further lightning on July 12) by Bochum engineers.
- Twice, some stations of the array produced artificial data.
- On July 12, future data were written to disk on the data acquisition workstation in Bochum. (The data acquisition software sometimes puts data with future time stamps onto the time sorted circular buffer. After an acquisition shutdown, a complete reinstallation of the acquisition environment (zero out disk loops of 16 hours capacity) is necessary. Then data are lost due to the insufficient buffer capacity of the CIM as documented during the GERESS System Verification Test. Teledyne has been asked to prevent an RDAS-200 from generating data with future time stamps. Science Horizons has been asked to make their software more robust).

Aug. 1991: - Desynchronization of A0 and C6
- RUB engineers finished array repair work on Aug 7.
- At Bochum, installation of upgrade of the data display software (SHI). (However, display stops continued, but now the display stopped for single channels instead of a bunch of channels).
- Malfunction of CIM at Bochum.
- Participation on revising the planned GERESS System Verification Test (Teledyne Geotech, 1991).

Sep. 1991: - Teledyne and Bochum engineers investigated the synchronization problem. Desynchronization due to distortion of the signals received via the optical data link. All optical links adjusted.
- Lightning protection installed at each RDAS.
- Sept. 12 - 23, GERESS System Verification Test (Teledyne Geotech, 1991; Golden et al., 1991).

- At Bochum, data display problem continued.
- On Sept. 30, future data were written to the disk on the data acquisition workstation at Bochum.
- Development of an automatic message system to transmit daily epicenter lists to interested scientist via e-mail.

Oct. 1991: - IAC crashes: 2.
- 22 times, 5 minute data gaps observed on all channels of a digiboard.
- Since October 21, daily sinusoidal calibration of all channels.
- At Bochum, malfunction of the data archiving routine SCHEDULER documented (30 minutes of data that had been transmitted were not archived).
- Development of an automatic alert message system to provide parameter data of strong teleseismic events to NEIC (Golden, CO) in near real time (start: Oct. 25).
- Analysis of teleseismic onsets off-line since Oct. 18.

Nov. 1991: - IAC crashes: 1.
- 27 times, 5 minute data gaps observed on all channels of a digiboard.
- Data acquisition workstation at Bochum malfunctioned.
- 4 times, 30 minutes of data that had been transmitted were not archived.
- Extension of the automatic alert message system to include strong regional events.

Dec. 1991: - IAC crashes: 2.
- December 5 - 15, Teledyne analyzed IAC for the cause of the inherent 9-second data gaps (9-second data gaps continued to exist at the same rate as before. The GERESS gap rate observed in NORSAR has been reduced, remaining on a significantly higher level than in Bochum).
- RUB engineers went to the array Dec. 2-6 and Dec. 9-13 (fix of D3 and D9, installation of SUN 3-E data acquisition workstation)
- At Bochum, 30 minutes of data that had been transmitted were not archived.

Jan. 1992: - At Bochum, 30 minutes of data that had been transmitted were not archived.
- Installation of test version of the Data Request Manager (DRM) by Krake Inc.

Feb. 1992: - IAC crashes: 2
- Feb. 10 - 14, maintenance visit by RUB engineer.
- Desynchronization on B1 (1 msec due to defective clock board).
- RDAS-200 software update (version 3.01) loaded to C2B (desynchronization problem BB13 on a RDAS-200 (Golden et al., 1991) was not fixed). A second software update finally fixed the problem on March 24.
- Installation of hardware for power cycling the IAC remotely (e.g., from Bochum) (information provided on the PSAC screen of each RDAS-200 can also be remotely obtained for diagnostics at Bochum).
- At Bochum, a software update for MONITOR_DL (version 1.5.2, SHI) was installed (several problems related to future data generated on the data acquisition system remain).
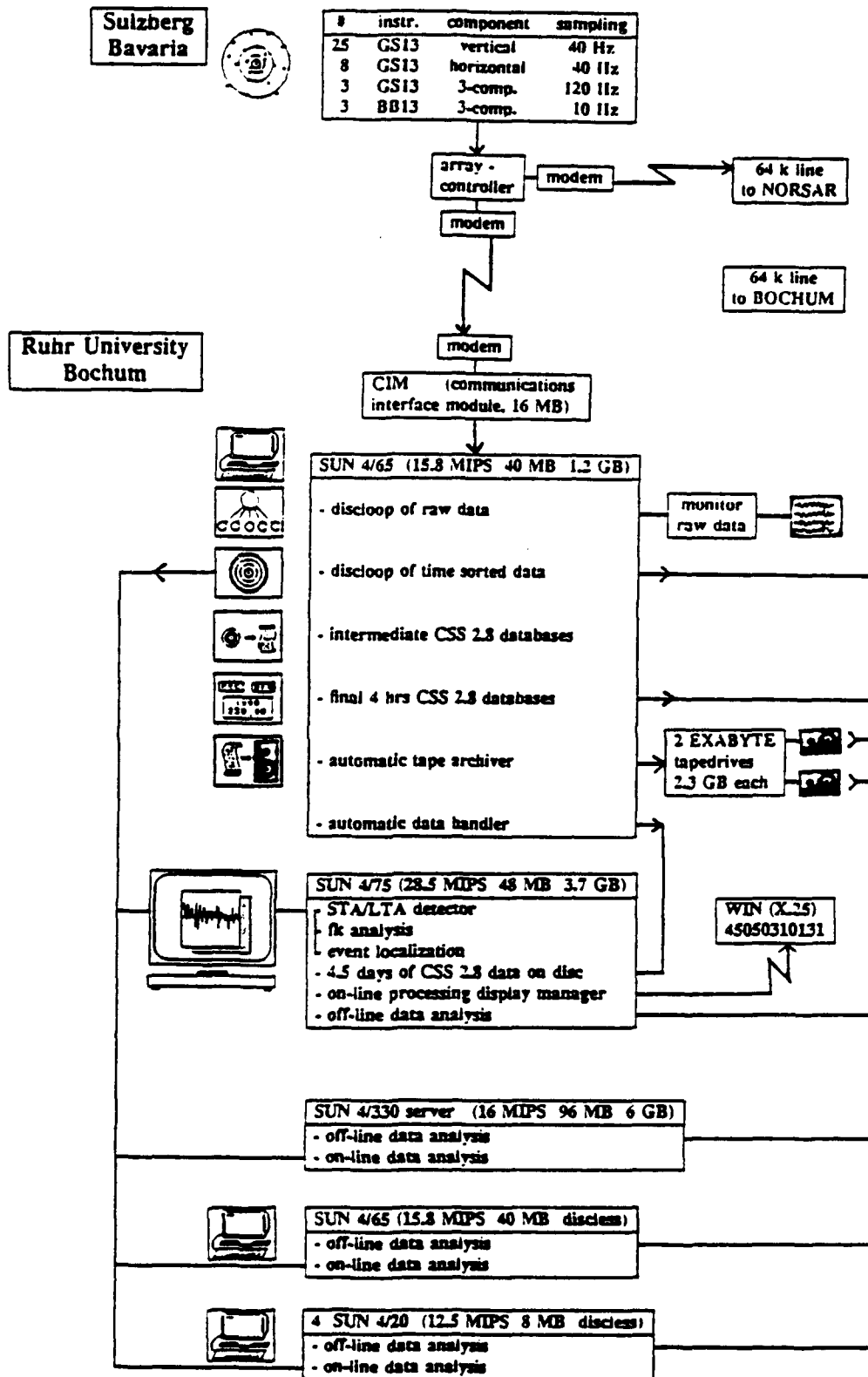
Sulzberg Bavaria

#	instr.	component	sampling
25	GS13	vertical	40 Hz
8	GS13	horizontal	40 Hz
3	GS13	3-comp.	120 Hz
3	BB13	3-comp.	10 Hz

array - controller → modem →～→ 64 k line to NORSAR

modem

64 k line to BOCHUM

Ruhr University Bochum

modem

CIM (communications interface module. 16 MB)

SUN 4/65 (15.8 MIPS 40 MB 1.2 GB)

- discloop of raw data

- discloop of time sorted data

- intermediate CSS 2.8 databases

- final 4 hrs CSS 2.8 databases

- automatic tape archiver

- automatic data handler

monitor raw data

2 EXABYTE tapedrives 2.3 GB each

SUN 4/75 (28.5 MIPS 48 MB 3.7 GB)
- STA/LTA detector
- fk analysis
- event localization
- 4.5 days of CSS 2.8 data on disc
- on-line processing display manager
- off-line data analysis

WIN (X.25) 45050310131

SUN 4/330 server (16 MIPS 96 MB 6 GB)
- off-line data analysis
- on-line data analysis

SUN 4/65 (15.8 MIPS 40 MB discless)
- off-line data analysis
- on-line data analysis

4 SUN 4/20 (12.5 MIPS 8 MB discless)
- off-line data analysis
- on-line data analysis

Figure 1-1: GERESS Observatory Bochum. Data Flow.

GERESS - BOCHUM BEAM SET

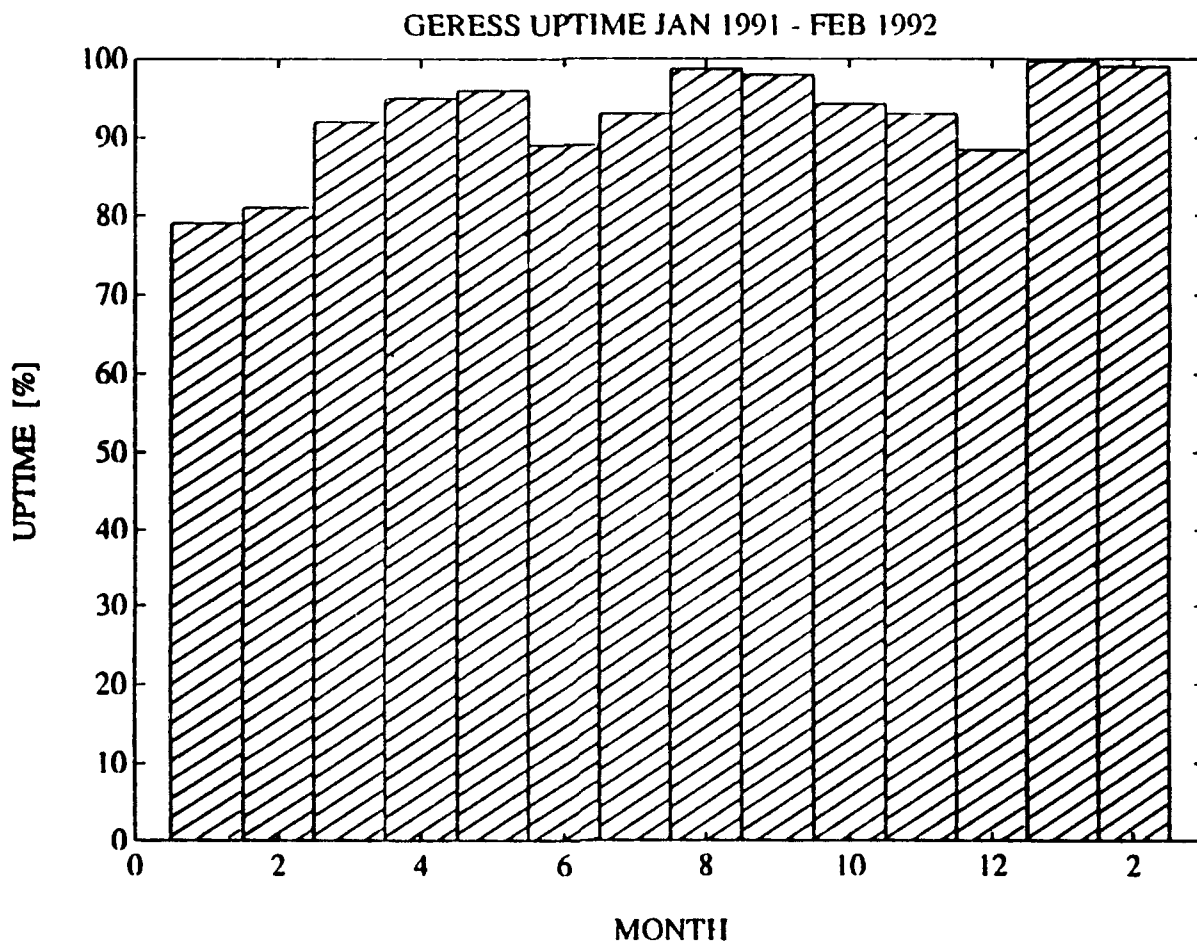| BEAM	AZ deg	ΔAZ deg	VEL km/sec	FILTER Hz - Hz	ORD	THR	STATION LIST
GF77	305		0.33	8.0-16.0	3	4.0	A0 A3 B3 B5 C1 C3 C5 D2 D5 D8 D9
GF88	99		0.33	8.0-16.0	3	4.0	A0 A3 B3 B5 C1 C3 C5 D2 D5 D8 D9
GC01 - GC12		30	4.0	0.7- 3.0	3	4.0	A1 A2 B1 B2 B4 B5 C1 C2 C3 C4 C5 C6 C7 D1 D2 D3 D4 D6 D7 D8 D9 -
GF01 - GF12		30	6.5	2.5- 4.5	4	4.0	A1 A2 B1 B2 B4 B5 C2 C3 C4 C6 C7 D1 D3 D4 D6 D7
GF13 - GF24		30	6.5	6.0-10.0	3	4.0	A1 A2 B1 B2 B4 B5 C2 C3 C4 C6 C7 D1 D3 D4 D6 D7
GG01 - GG12		30	8.5	1.0- 4.0	3	4.0	A1 A2 B1 B2 B4 B5 C2 C3 C4 C6 C7 D1 D3 D4 D6 D7
GG13 - GG24		30	8.5	6.0-10.0	3	4.0	A1 A2 B1 B2 B4 B5 C2 C3 C4 C6 C7 D1 D3 D4 D6 D7
GA01 - GA12		30	12.0	1.0- 3.0	4	4.0	A1 A2 B1 B2 B4 B5 C1 C2 C3 C4 C5 C6 C7 D1 D2 D3 D4 D6 D7 D8 D9
GF99	0		999.9	0.7- 2.0	4	4.0	A0 C1 C2 C3 C4 C5 C6 C7 D1 D2 D3 D4 D5 D6 D7 D8 D9
GVI2	0		999.9	1.0- 4.0	3	3.0	A1 A2 B1 B2 B4 B5 C1 C2 C3 C4 C5 C6 C7 D1 D2 D3 D4 D6 D7 D8 D9
GHI1	0		999.9	1.0- 4.0	3	3.0	A2_sn A2_se D1_sn D1_se D4_sn D4_se D7_sn D7_se
GHI2	0		999.9	8.0-16.0	3	3.0	A2_sn A2_se D1_sn D1_se D4_sn D4_se D7_sn D7_se
GHI3	0		999.9	0.7- 2.0	4	3.0	A2_sn A2_se D1_sn D1_se D4_sn D4_se D7_sn D7_se

Figure 1-2: GERESS Bochum beam set.

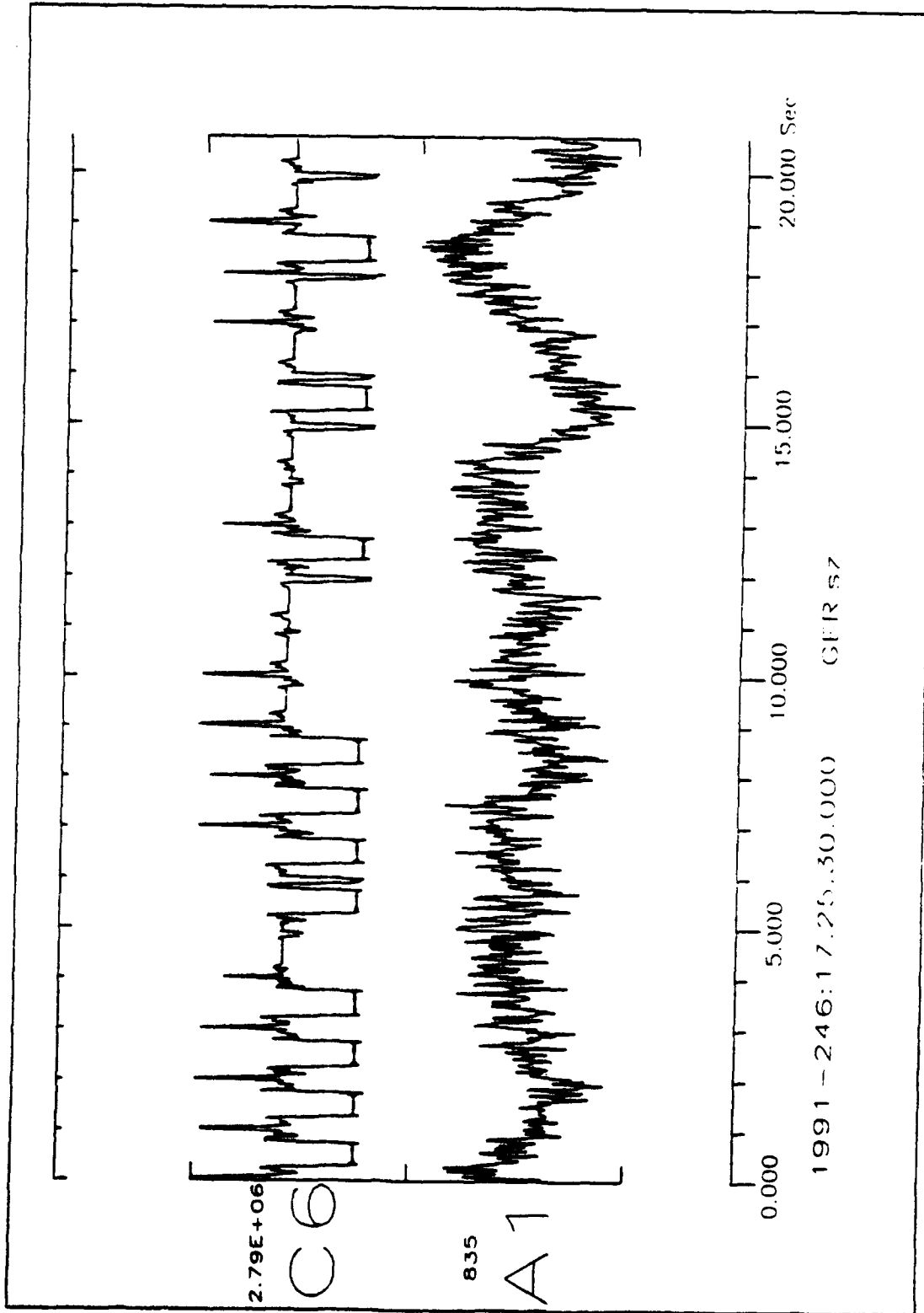Figure 1-3: GERESS uptime from January 1991 - February 1992.

Figure 1-4: Unfiltered data from all channels of GERESS on Feb. 6, 1992 02:30:26.65 - 02:30:48.65. From top to bottom are displayed A0, A1, A2 (z,n,e), A3, B1, B2, B3, B4, B5, C1, C2 (sz,bz,bn,be, hz,hn,he), C3, C4, C5, C6, C7, D1 (z,n,e), D2, D3, D4 (z,n,e), D5, D6, D7 (z,n,e), D8, D9). The tics on the vertical axis indicate +/- 555 counts. B1 is off-line. Note the 15 second outage on digiboard 1 (A-ring, B1, B2, B3). At 02:30:36, transmission related 1-second data gaps are evident on B4, B5, C1, C5, D1-sz, D2, D3.

- 12 -

Figure 1-5: Time synchronization signals from the GERESS HUB (1 pps) were replacing seismometer input at C6-sz (GS-13) on Sep. 3, 1991 17:25:30. Note the severe distortion of the synchronization signal due to misadjustment of the optical link.

2. GERESS P-Wave Detectability

Michael L. Jost

2.1 Introduction

The German Experimental Regional Seismic System (GERESS) array was specifically designed to significantly increase the detection capability for regional seismic phases ($\Delta < 1500$ km) in Central Europe. After one year of full operation, it was found that GERESS also has an excellent capability to detect teleseismic onsets (e.g., GSETT-2, phase-3, this report).

A systematic study has been carried out to determine the performance of the newly installed GERESS array. Following the study done by Kvaerna (1989) for NORESS, an evaluation of the P-wave detectability of GERESS was undertaken. By assuming that primary phases are embedded in pure noise, the signal to noise ratio (SNR) can be increased by beamforming (delay and sum). The correlation of the noise at the N sensors of the array is dependent on the sensors' relative distances and also on the dominant wavelength of the noise. If the noise is completely uncorrelated at the N sensors, the signal enhancement due to beamforming is expected to be $\sqrt{N}$. Secondary phases are embedded in a coda of the primary energy that is not completely uncorrelated. Hence beamforming for Sg or Lg onsets is expected to improve the SNR far less than $\sqrt{N}$.

In this study, a quantitative assessment of the SNR improvement by beamforming was done for P-phases of strong local, regional, and teleseismic events at various frequencies and for different array subgeometries. Results of this study can be used to optimize the set of beams used for the automatic on-line data processing in Bochum.

2.2 Data Analysis

To objectively access the P-wave detectability for GERESS, the analysis was based on the GERESS on-line data analysis software (Mykkeltveit and Bungum, 1984; Fyen, 1987). Initially in the detection process, beams are formed using results of the frequency wavenumber analysis. Next, the beam traces are filtered by butterworth band-pass filters. Finally, a detection is declared if the short term average over long term average ratio (SNR = STA/LTA) surpasses a set threshold. This detection procedure was applied in this study for various strong local, regional, and teleseismic events.

The data analysis proceeded in the following way:

1) 13 partially overlapping 1-octave (except BP02 and BP13) band-pass filters have been defined (Table 2-1). These filters are identical, except BP02, to

those defined by Kvaerna (1989).

2) Using the 25 short-period vertical components of GERESS, 11 subgeometries were defined (Table 2-2). It was observed that the noisy stations A0, A3, and B3 did not improve the SNR at high frequencies. For consistency, those 3 stations were omitted for all frequencies throughout this study. Since the GERESS center station, A0, is also the noisiest of the array, A2-sz was chosen as reference station. From those 11 subgeometries (Table 2-2), 3 are nearly identical and can be neglected: BCD, BC, and B contain one station less than ABCD, ABC, and AB, respectively. Configuration F (all stations that are on hard rock sites) is asymmetric which suggests that detection capabilities vary with azimuth. Hence configuration F will not be further analyzed. Configuration A consists of only 2 channels. Configuration C has 2 channels less than D. For the detection of teleseismic events, configurations D or CD seem more appropriate than C. In conclusion, from the 11 subgeometries (Table 2-2), 5 configurations seem to be promising for further evaluation which are: AB, ABC, ABCD, CD, and D.

3.) The amount of data that can be used for this study is comparatively small. Although GERESS became fully operational in January 1991, the channel desynchronization problem was not solved until the GERESS System Verification Test in September 1991 (GERESS Status Report, this volume). This test classified the GERESS installation as "not fully acceptable" (Golden et al., 1991). Data have continued to show various problems after September 1991: Channel outages or desynchronizations hindered the use of many promising events. For this study, events were selected by searching through the bulletins of the GERESS on-line data analysis at Bochum. As a first step to use as much high SNR data as possible, the desynchronized channels were manually synchronized when possible (3 cases) and parameter values of missing channels were estimated by mean values (14 cases). Tests on this procedure showed that the influence of the estimation can be neglected for the subarray configurations that were further analyzed in this study. By this procedure, 28 events were selected (Table 2-3).

4) For each event, a wide-band frequency-wavenumber analysis (Kvaerna and Doornbos, 1986) was carried out. Using all available channels, the slowness and back-azimuth of the incident P-wave was determined.

5) For all events, a detection processing was applied using the on-line program system (Fyen, 1987). The SNR, STA, and LTA detection values for all beams and single channels were determined. From these values, the SNR gain, noise suppression, and signal loss values were calculated. The SNR gain is defined as the ratio of the SNR of the beam to the average SNR of the single channels that participate in the beamforming. Noise suppression is the ratio of the average LTA of the channels in the beam to the beam LTA. The signal loss is the

ratio of the average STA of the channels in the beam to the beam STA. In the logarithmic domain (db), the noise suppression equals the sum of the SNR gain and the signal loss.

The STA values were determined by averaging absolute values over 1 sec intervals. The LTA values were calculated by averaging over 30 seconds. Kvaerna (1989) has shown that the specific choice of these values does not influence the beamforming results.

2.3 Results

Table 2-4 and 2-5 show examples of the output of the data processing for a regional event on Oct 31, 1991 (see Table 2-3). In the following, only the lower cutoff of the band-pass filters (Table 2-1) is indicated. This is fully justified due to the fact that the amplitudes of noise decrease with increasing frequencies.

Table 2-4 shows the SNR gain, the noise suppression (NSUP), the signal loss (SLS), and the LTA in the pass-band of 1.0 - 2.0 Hz for different array subgeometries. This table also includes the number of stations used and the theoretical values for the SNR gain. For the event on Oct 31, 1991, the configurations D (A2 and D-ring), F (hard rock sites), and CD (A2, C- and D-ring) show higher SNR ratio improvement than expected by $\sqrt{N}$. This fact can be explained by negative noise correlation for certain interstation separations. The signal loss is small enough to be neglected for the configurations D, F, and CD. Note that the performance of the inner rings (configurations A, AB, B, ABC, BC) is well below the $\sqrt{N}$ value in this pass-band.

Table 2-5 shows the SNR gain, the noise suppression (NSUP), the signal loss (SLS), and the values of the SNR at different frequencies for the configuration ABCD. The noise suppression remains at a high level nearly over the whole frequency band (1.0 - 10.0 Hz). Configuration ABCD consists of 22 channels suggesting a noise reduction by 13.4 db. At 1.5 Hz, a SNR gain in excess of 13.4 db is observed. From 1.0 - 5.0 Hz, the SNR gain shows a plateau, which tapers off to low as well as to high frequencies. As the frequency of the band-pass filters increases signals become incoherent and hence the signal loss increases. For the subsequent analysis, values at high and low frequencies (i.e. 0.5 Hz, 0.7 Hz, 6.0 - 10.0 Hz) were not further considered for the studied event since these values are more related to the signal content at these frequencies (source, medium) than to properties of the array.

The detection processing which was demonstrated for one event (Tables 2-4 and 2-5) was repeated for all events listed in Table 2-3. For each event, only those SNR gain values that fell into a plateau region are shown in Figure 2-1. The following figures consist of 3 parts: the noise suppression is displayed on top, the signal loss in the middle, and the SNR gain on the bottom. Figure 2-1 summarizes the results of detection processing for the configuration ABCD. Mean values and the 13.4 db level are given. In Figure 2-1, circles indicate

results from local, triangles from regional, and crosses from teleseismic events. Results of teleseismic events could not be obtained for pass-band frequencies larger than about 4 Hz which can be related to medium properties. Results for regional events are available from 0.5 - 10 Hz and for local events from about 2 - 10 Hz.

Figure 2-2 displays the mean curves for 5 of the 11 configurations defined in Table 2-2: AB, ABC, ABCD, CD, and D. This figure shows that the full array (ABCD) gives the largest SNR gains from 1.5 - 6 Hz. Configuration CD is slightly better from 0.5 - 1.5 Hz. From 6 - 10 Hz, the inner 3 rings (ABC) show the optimum SNR gain for GERESS. The noise suppression is showing a broad plateau from about 1.5 - 10 Hz for all configurations. For configurations D, CD, and ABCD, a maximum is superimposed between 1.5 - 4 Hz. The signal loss curves show 2 trends for 5 - 10 Hz: configurations D, CD, and ABCD have a larger (3 db) signal loss than the inner rings (AB and ABC).

Figures 2-3 and 2-4 compare the mean curves for GERESS and NORESS (Kvaerna, 1989) for configuration ABCD (full array) and CD (center station & 2 outer rings), respectively. The data analysis for configuration ABCD was based on 25 channels at NORESS (the theoretical noise suppression is 14.0 db) and 22 channels at GERESS (the theoretical noise suppression is 13.4 db). In the frequency range of 1 - 3 Hz, the noise suppression for GERESS seems to be better than for NORESS for configuration ABCD; they are very similar for configuration CD. From 3 - 6 Hz, noise suppression values at both arrays are very similar. From 6 - 10 Hz, GERESS shows a poorer noise suppression (1 - 2 db) for both configurations. The signal loss at GERESS and NORESS is comparable, although GERESS seems to have a somewhat larger signal loss at higher frequencies (5 - 10 Hz). The SNR gain shows a similar behavior as the noise suppression: from 6 - 10 Hz, GERESS has a significantly poorer SNR gain.

The cause of these differences between NORESS and GERESS seems to be the different noise characteristics at both arrays as observed by Harjes (1990). At NORESS, low frequent noise (around 1 Hz) shows an order of magnitude higher peak spectral displacement values than at GERESS (10 nm^2/Hz versus 0,7 nm^2/Hz, respectively). Hence GERESS shows an increased detection capability at lower frequencies (Figures 2-3 and 2-4). From 3 - 6 Hz, GERESS records show cultural noise that varies with time of day. Cultural noise at NORESS is mainly observed in the frequency range of 5 - 9 Hz. At high frequencies (around 10 Hz), the noise values at GERESS are significantly higher than at NORESS (2.5 10^{-4} nm^2/Hz versus 0.6 10^{-4} nm^2/Hz). These differences in noise level may serve as one explanation of the observed poorer SNR gains at GERESS in the frequency range of 6 - 10 Hz.

2.4 Conclusion

Following work by Kvaerna (1989) for NORESS, an evaluation of the P-wave detectability at GERESS was undertaken. In the frequency range of 1 - 3 Hz, GERESS reaches a higher noise suppression and SNR gain than expected by $\sqrt{N}$. In the same frequency range, the SNR gain is higher at GERESS than at NORESS for the full array, and similar for the outer 2 rings. Compared with NORESS, GERESS shows a similar SNR gain in the frequency range of 3 - 6 Hz. At higher frequencies, the SNR gain at GERESS is significantly poorer than at NORESS. The differences in SNR gains observed at NORESS and GERESS clearly correlate with the noise characteristics at both array sites.

Since the GERESS array is still not fully acceptable (Golden et al., 1991), data of many strong events could not be used in this study. The conclusions with respect to the high frequencies could be modified when more high quality data are available. Hence the analysis will be extended to a larger data set. In addition, secondary phases will also be addressed since the detection of S-phases fundamentally affects location capabilities of GERESS.

2.5 Literature

Fyen, J. (1987). Improvements and modifications, Semiannual Technical Summary, 1 October 1986-31 March 1987, NORSAR Sci. Rep. No. 2-86/87, Kjeller, Norway.

Golden, P., E. T. Herrin, and C. Hayward (1991). Results of the GERESS verification test, in: Development of an intelligent seismic facility and preparation for participation in the conference on disarmament group of scientific experts technical test, Quarterly Technical Report, Southern Methodist University, Dallas, Texas.

Harjes, H.-P. (1990). Design and siting of a new regional array in Central Europe, Bull. Seism. Soc. Am. 80, 1801-1817.

Kvaerna, T. (1989). On exploitation of small-aperture NORESS type arrays for enhanced P-wave detectability, Bull. Seism. Soc. Am. 79, 888-900.

Kvaerna, T. and D. J. Doornbos (1986). An integrated approach to slowness analysis with arrays and 3-component stations, Semiannual Technical Summary, 1 October 1985-31 March 1986, NORSAR Sci. Rep. No. 2-85/86, Kjeller, Norway.

Mykkeltveit, S. and H. Bungum (1984). Processing of regional seismic events using data from small- aperture arrays, Bull. Seism. Soc. Am. 74, 2313-2333.

TABLE 2-1: BUTTERWORTH BAND-PASS FILTERS

FILTER	f_L [Hz]	f_H [Hz]	ORDER
BP01	0.5	1.0	3
BP02	0.7	2.0	3
BP03	1.0	2.0	3
BP04	1.5	3.0	3
BP05	2.0	4.0	3
BP06	2.5	5.0	3
BP07	3.0	6.0	3
BP08	3.5	7.0	3
BP09	4.0	8.0	3
BP10	5.0	10.0	3
BP11	6.0	12.0	3
BP12	8.0	16.0	3
BP13	10.0	16.0	3

TABLE 2-2: DEFINITION OF GERESS SUBGEOMETRIES

CHANNEL	D	F	CD	BCD	ABCD	C	BC	ABC	B	AB	A
A0	0	0	0	0	0	0	0	0	0	0	0
A1	0	0	0	0	1	0	0	1	0	1	1
A2	1	1	1	1	1	1	1	1	1	1	1
A3	0	0	0	0	0	0	0	0	0	0	0
B1	0	0	0	1	1	0	1	1	1	1	0
B2	0	1	0	1	1	0	1	1	1	1	0
B3	0	0	0	0	0	0	0	0	0	0	0
B4	0	0	0	1	1	0	1	1	1	1	0
B5	0	1	0	1	1	0	1	1	1	1	0
C1	0	0	1	1	1	1	1	1	0	0	0
C2	0	1	1	1	1	1	1	1	0	0	0
C3	0	0	1	1	1	1	1	1	0	0	0
C4	0	0	1	1	1	1	1	1	0	0	0
C5	0	0	1	1	1	1	1	1	0	0	0
C6	0	1	1	1	1	1	1	1	0	0	0
C7	0	1	1	1	1	1	1	1	0	0	0
D1	1	1	1	1	1	0	0	0	0	0	0
D2	1	1	1	1	1	0	0	0	0	0	0
D3	1	1	1	1	1	0	0	0	0	0	0
D4	1	1	1	1	1	0	0	0	0	0	0
D5	1	0	1	1	1	0	0	0	0	0	0
D6	1	1	1	1	1	0	0	0	0	0	0
D7	1	1	1	1	1	0	0	0	0	0	0
D8	1	0	1	1	1	0	0	0	0	0	0
D9	1	0	1	1	1	0	0	0	0	0	0

TABLE 2-3: LIST OF EVENTS

DATE ddmmyy	ORIGIN TIME	LAT N	LON E	MAG	Δ [km]	VEL [km/s]	BAZ [deg]
30.09.91	15.54.10.6	48.937	12.859	$1.7^{(2)}$	62.4	6.1	276.2
02.10.91	10.54.58.2	48.559	13.306	$1.9^{(2)}$	43.1	5.9	224.6
08.10.91	03:31.15.6	45.557	149.039	$6.0^{(3)}$	8698.1	20.7	39.1
17.10.91	11.43.55.6	48.852	14.231	$1.4^{(2)}$	38.7	5.8	88.2
28.10.91	00.21.30.3	44.332	21.378	$4.0^{(3)}$	773.0	7.9	121.4
31.10.91	09.31.17.9	45.031	10.054	$4.7(3)^{(1)}$	507.1	9.1	206.1
20.11.91	01.54.16.9	46.770	9.532	$5.1(3)^{(1)}$	388.5	8.8	235.7
22.11.91	08.20.44.0	50.518	14.973	$2.2^{(2)}$	207.2	6.5	8.9
30.11.91	11.29.47.1	50.367	14.665	$1.9^{(2)}$	182.8	7.1	22.5
02.12.91	08.49.40.2	45.483	21.123	$5.3(2)^{(1)}$	675.5	7.7	114.7
05.12.91	12.03.18.3	50.475	12.537	$1.5^{(2)}$	199.6	7.9	341.2
13.12.91	02:33.52.2	45.582	151.629	$6.2^{(3)}$	8789.2	26.1	35.3
13.12.91	05.45.29.9	45.538	151.531	$6.0^{(3)}$	8790.1	24.0	34.5
13.12.91	18.59.11.0	45.554	151.718	$6.2^{(3)}$	8795.1	25.8	37.6
17.12.91	06.38.16.2	47.347	151.525	$5.9^{(3)}$	8610.5	23.5	35.2
19.12.91	03.12.23.9	45.882	21.521	$4.4(2)^{(1)}$	676.3	7.9	112.6
19.12.91	18.55.18.8	28.279	57.317	$5.4^{(3)}$	4351.9	13.4	113.9
20.12.91	02.06.05.7	24.668	93.090	$5.5^{(3)}$	7230.2	18.4	78.0
01.01.92	10.12.19.9	44.984	9.962	$3.3(3)^{(1)}$	515.4	8.5	202.6
02.01.92	13.44.59.8	44.998	9.964	$3.5(1)^{(1)}$	514.0	8.6	203.6
02.01.92	19.41.45.8	5.663	-73.836	$5.8^{(3)}$	9357.7	31.0	269.1
08.01.92	08.52.59.5	47.455	14.925	$1.4^{(2)}$	179.1	6.5	151.0
23.01.92	04.24.14.8	38.335	20.319	$5.0(2)^{(1)}$	1283.6	8.3	157.7
23.01.92	06.27.38.8	38.351	20.301	$4.5(1)^{(1)}$	1281.3	8.0	157.2
29.01.92	12.00.27.8	49.894	13.639	$1.5^{(2)}$	116.6	6.3	351.3
01.02.92	15.22.27.7	47.475	13.611	$1.9^{(2)}$	152.4	7.0	183.2
02.02.92	00.31.30.2	-51.666	139.491	$5.6^{(3)}$	16222.3	29.0	135.9
17.02.92	19.23.08.0	47.076	8.932	$3.3^{(1)}$	405.7	8.5	238.6

(1) mean ML (number of PDE stations)

(2) ML determined at GERESS

(3) mb from the PDE

TABLE 2-4: RESULTS OF THE PROCESSING FOR THE EVENT
ON 31.10.91 IN THE PASS-BAND 1.0 - 2.0 HZ
(SEE TABLE 2-2 FOR THE DEFINITIONS OF SUBGEOMETRIES)

CONFIG	N	THEO. SNRG db	SNRG db	NSUP db	SLS db	LTA
D	10	10.0	11.94	11.99	0.05	14.13
F	12	10.8	11.39	11.47	0.08	14.70
CD	17	12.3	13.23	13.32	0.09	12.11
BCD	21	13.2	12.94	13.03	0.09	12.56
ABCD	22	13.4	12.39	12.47	0.08	13.36
C	8	9.0	8.89	9.09	0.20	19.82
BC	12	10.8	8.26	8.51	0.25	21.25
ABC	13	11.1	7.77	8.03	0.26	22.37
B	5	7.0	3.32	3.49	0.17	38.38
AB	6	7.8	2.87	3.03	0.16	40.01
A	2	3.0	0.49	0.55	0.06	52.99

TABLE 2-5: RESULTS OF THE PROCESSING
FOR THE EVENT ON 31.10.91 FOR
CONFIGURATION ABCD

f Hz	SNRG db	NSUP db	SLS db	SNR
0.5	2.87	3.07	0.20	27
0.7	7.69	7.69	0.00	191
1.0	12.39	12.47	0.08	376
1.5	14.36	15.01	0.65	322
2.0	10.83	12.83	2.00	161
2.5	11.50	13.04	1.54	157
3.0	11.18	13.12	1.94	175
3.5	11.24	13.25	2.01	188
4.0	11.06	13.37	2.31	194
5.0	10.36	13.46	3.10	238
6.0	7.57	13.36	5.79	178
8.0	4.54	12.67	8.13	91
10.0	2.08	12.67	10.59	43
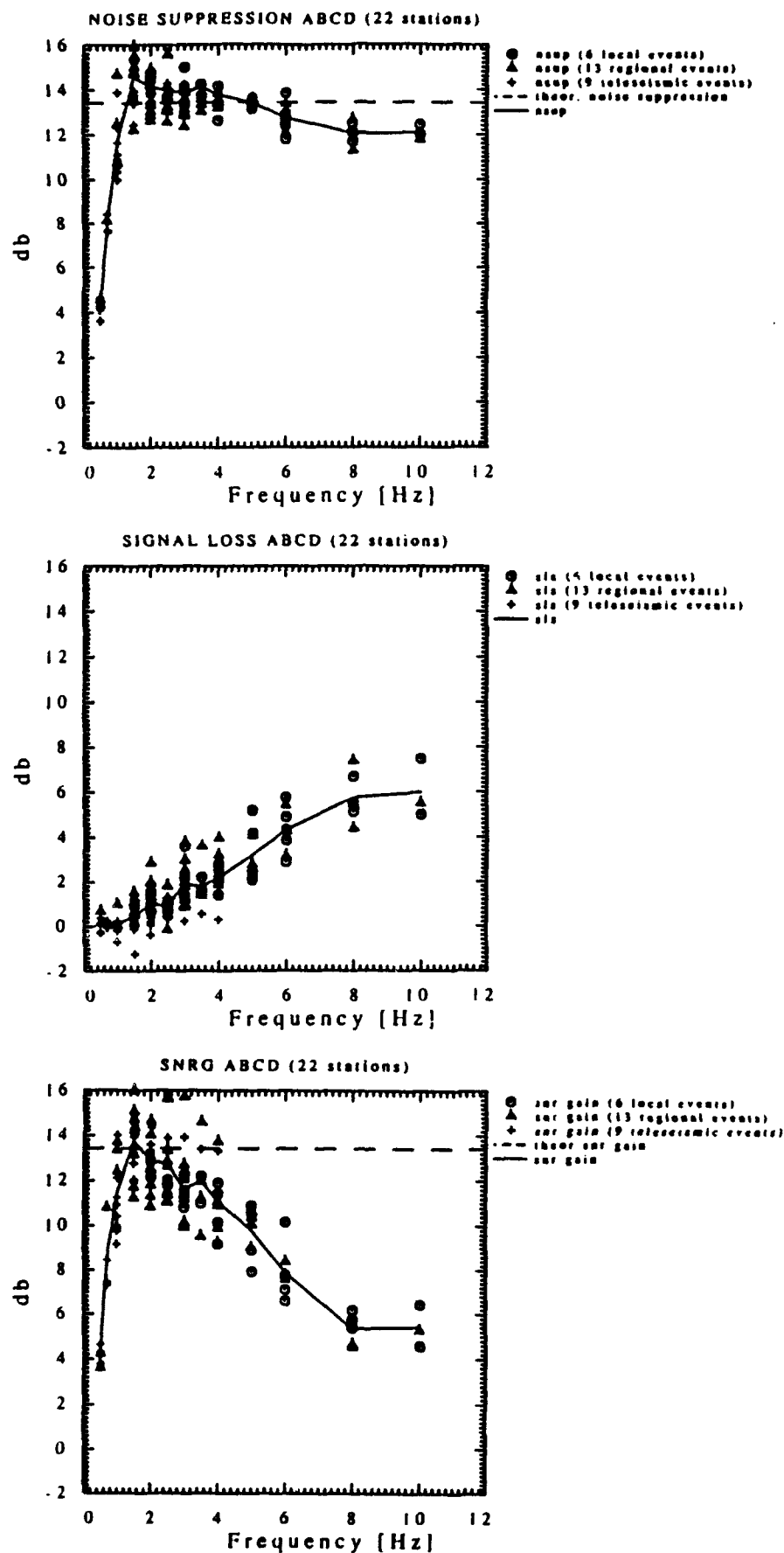
Figure 2-1: Noise suppression, signal loss, and SNR gain, for configuration ABCD of GERESS. Mean values (solid line) and the theoretical noise suppression (dashed line) are indicated. Circles were determined from local, triangles from regional, and crosses from teleseismic events (see Table 2-3).
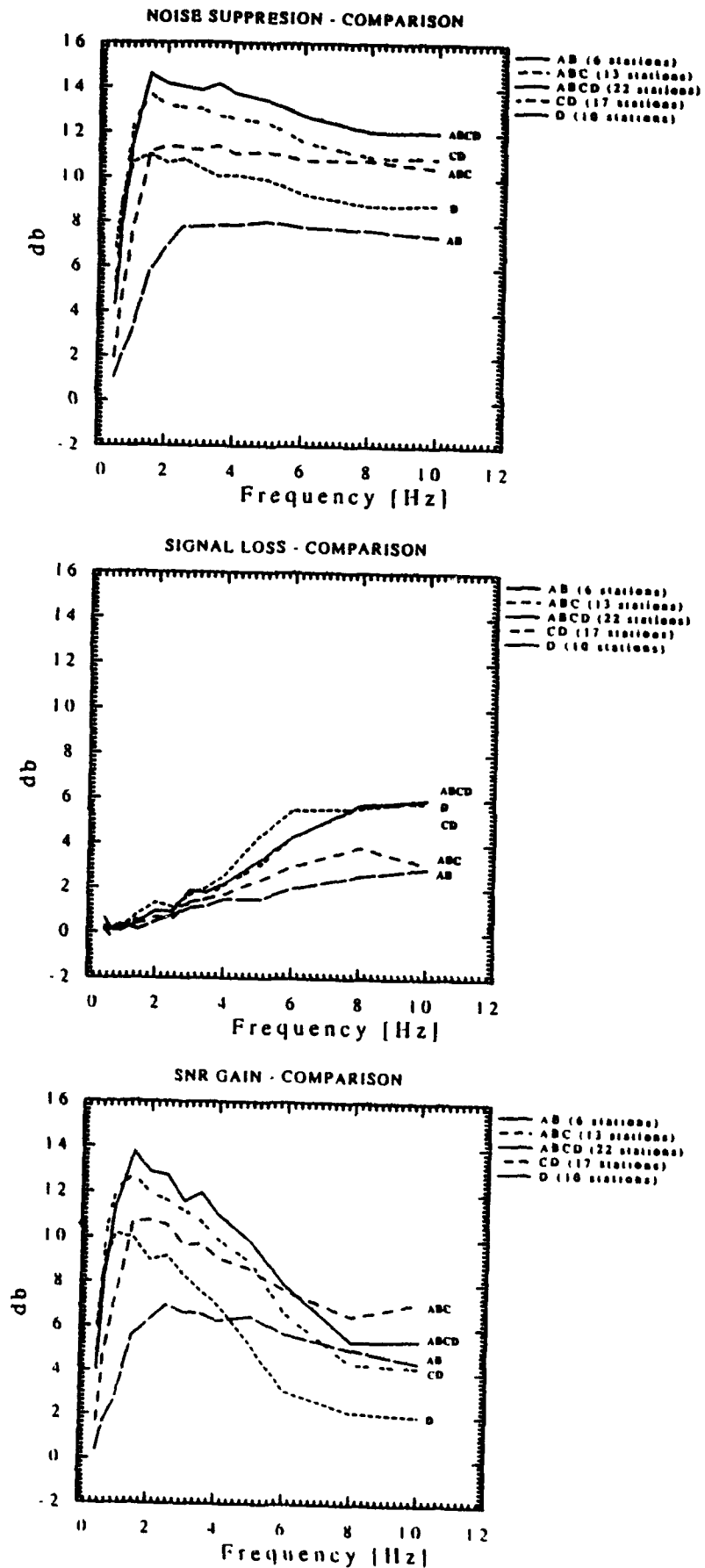
Figure 2-2: Mean curves of noise suppression, signal loss, and SNR gain for 5 subgeometries of GERESS.

NOISE SUPPRESION ABCD - COMPARISON

SIGNAL LOSS ABCD - COMPARISON

SNRG ABCD - COMPARISON
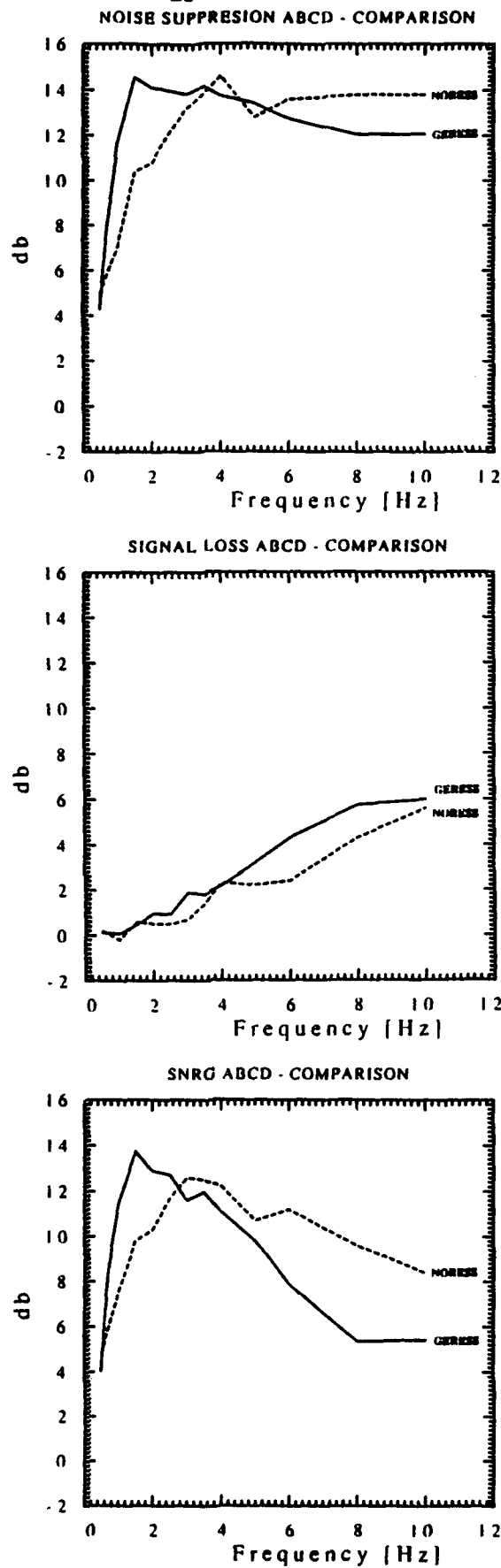
Figure 2-3: Mean curves of noise suppression, signal loss, and SNR gain for configuration ABCD of GERESS (solid line) and NORESS (dashed line; from Kvaerna, 1989).

NOISE SUPPRESION CD - COMPARISON

SIGNAL LOSS CD - COMPARISON

SNRG CD - COMPARISON
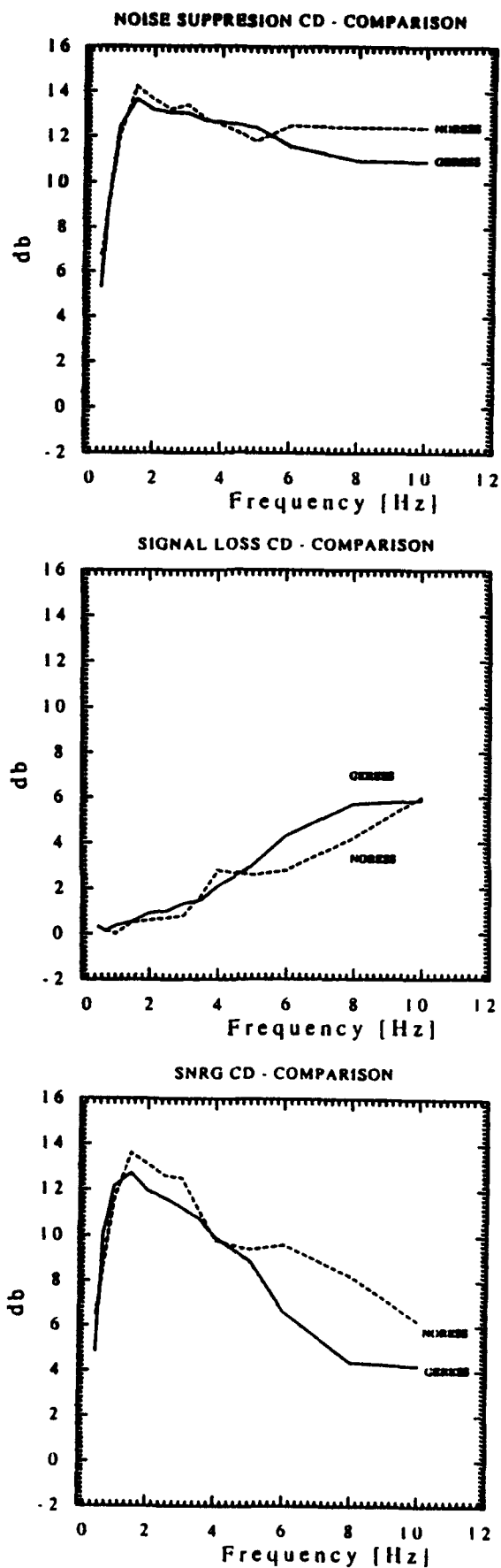
Figure 2-4: Mean curves of noise suppression, signal loss, and SNR gain for configuration CD of GERESS (solid line) and NORESS (dashed line; from Kvaerna, 1989).

3. THE GERESS CONTRIBUTION TO THE GSETT-2 EXPERIMENT 1991

Johannes Schweitzer

3.1 INTRODUCTION

The GERESS array became fully operational in January 1991. Participation in GSETT-2 (Group of Scientific Experts Technical Test 2) was the first opportunity to investigate the detection and location capability of GERESS. Because the German National Data Center (NDC) in Hannover was not able to handle the large amount of GERESS-data these data were analyzed with the support of the NORSAR-staff in Kjeller, Norway.

The GSETT-2 period covered six weeks from April 22, 1991 to June 2, 1991. This experiment aimed at testing procedures of an international seismic data exchange system for a future nuclear test ban treaty. Therefore it was necessary to detect and locate as many seismic events as possible worldwide within a specified short time interval. Every contributing country had to analyze seismograms daily and sent all level-1 data (parameter data) and if possible all level-2 data (waveform data) to one of the four Experimental International Data Centers (EIDC) in Canberra, Moscow, Stockholm, or Washington. From the contributions of all stations (57 worldwide), the EIDCs located the events and compiled the Final Event Bulletins (FEB). These bulletins were sent back to the NDCs after one week. GERESS was one of the 12 seismic arrays participated in the test and contributed level-1 and level-2 data. Because of technical difficulties of GERESS (s. Chapter 1 in this Report) not all data were available. Observed outages were caused by problems with the array controller in Bavaria, by problems with the communication between Bavaria and NORSAR, and by problems with the data acquisition system in Norway. Nevertheless, GERESS-data were analyzed for 92.25 % of the GSETT-2 period.

3.2 DATA ANALYSIS

The GERESS data stream was automatically analyzed using NORSAR routines. To adjust to GERESS conditions, some software changes were made:

a) Site C2 was defined as reference station instead of A0.

b) A specific beam configuration was installed.

c) For the location of local and regional events, the travel time tables used in Scandinavia were changed to the Jeffreys-Bullen tables. This implied the use of Sg instead of Lg.

d) The overall transfer function of GERESS (Wüster, 1991) was implemented.

All data were filtered within seven different passbands and a STA/LTA detector was running online over 80 different beam traces. For all detected onsets azimuth and velocity were calculated automatically (fk-analysis). Every detection was checked interactively and every arrival was reanalyzed. Especially all bad traces (spikes, data gaps) had to be eliminated manually and the fk-analysis was repeated. From 8443 detections, 3795 (44.9 %) onsets were reported with their arrival time, estimated velocity and azimuth, maximum amplitude and period. All measurements were done on the beam trace of the array. The velocity information was used to label the phases. In detail GERESS reported:

Phase	Number
P	837
Pn	412
Pg	806
Sn	162
Sg	817
Lg	176
Rg	594

Additionally, phases were grouped together to events and locations were determined with RONAPP (Mykkeltveit and Bungum, 1984). 705 locations were reported (Fig. 3.1), including source time, latitude, longitude and ML value.

If we compare the amount of GERESS-data contributing to the FEBs with other arrays or single stations (B. North, pers. communication) it is obvious that GERESS is the most sensitive station in Central Europe. 1325 phases (33.3 %) were associated to FEB events by the EIDCs. 1064 phases (27 %) were reported as NDCs events which could not be confirmed by other independent observations and 1553 phases (39.3) were left as unassociated. Most of them were single crustal phases (Sg, Lg, Rg) from small events for which the GERESS detector missed the P-arrival and an NDC location could not be defined. Roughly 10 % of all GERESS reportings were misassociated by the EIDCs or they appear twice in the FEBs.

3.3 LOCAL AND REGIONAL EVENTS

Fig. 3.2 shows that the events located by GERESS are concentrated in a circle of 5° around GERESS. Only for the seismic active region around the Mediterranean Sea some events were located at larger distances. Most of the local seismic activity around GERESS is caused by quarries in Southern Germany, Austria, and the CSFR. The two distinct source regions in Poland are the two mining areas in Upper Silesia (cupper and stone coal). It can be daily demonstrated that most of the events around GERESS are not part of the natural seismicity. Fig. 3.3 shows the number of events per hour versus day of the week. The data were corrected for local holidays and GERESS outages. Clearly seen is the decrease of events at the weekends when the quarries in Germany and Austria do not work. The minimum is on Sunday when only the brown coal district in the CSFR is active. This conclusion is confirmed by Fig. 3.4 in which the number of events is plotted versus hour. The source time correlates strongly with the working hours in the quarries between 7:00 and 15:00 UT (9:00 and 17:00 local time) with a peak around noon (lunch time). This is a preferred shooting time because of security instructions.

Fig. 3.5 shows the local magnitudes versus distance of the events. Magnitudes were calculated with an amplitude distance relation estimated for Scandinavia (Båth et al., 1976). The observed magnitudes are very small. The two lines show different amplitude distance relations both fixed for ML = 2.0 at a distance of 1000 km. The lower line shows the previously used Scandinavian calibration curve and the second (upper) line shows the now in Bochum used amplitude distance relation (s. Chapter 1, page 2). The new curve represents the lowest at GERESS observed magnitudes much better.

The locations by GERESS show - as single array solutions - some uncertainties. These were caused by detections with low signal to noise ratios (SNR), by scatter in the results of the fk-analysis, by the velocity model (the simplified two layer crust model of Jeffreys-Bullen tables), and by systematic mislocations due to the lateral heterogeneous crust around GERESS. To investigate these problems the GERESS locations can be compared with results of international organizations. In this case, the GERESS results were compared with the Earthquake Data Report (EDR) of NEIC. 58 events were located by both, GERESS and NEIC. Fig. 3.6 shows all GERESS events with respect to their EDR solution (triangle). Clearly seen are some systematic mislocations especially in the south but the GERESS solutions are very close to the network solution within a distance of about 4° around GERESS. This leads to the conclusion that a careful calibration of the array for events in regional distances is needed.

Fig. 3.7 shows the GSETT-2 network in and around Europe. With these stations all FEB events in Fig. 3.8 were located by the EIDCs. It is not surprising that most of the events are concentrated around the regional arrays in Scandinavia and around GERESS. As discussed above in the case of GERESS, the observed large seismicity in Northern Europe is also due to artificial events in quarries or mining areas.

In Fig. 3.8 the seismicity around GERESS seems to be much less than detected by GERESS (s. Fig. 3.1) but this is due to the rules for compiling the FEBs: One hypocenter can be estimated by at least four defining observations, not all PKP, at three stations or one defining measurement (arrival time, azimuth, and slowness) at one station and two observations at another. Therefore only the larger events located by GERESS were listed in the FEBs.

On the other hand, several FEB events in Europe were not located by GERESS. Most of them were observed by GERESS but only with one phase. Fig. 3.9 shows this effect in more detail. All FEB events to which a GERESS observation was associated were plotted. Only few events in Central and Southern Europe were missed by GERESS (compare Fig. 3.8 with Fig. 3.9). An opposite picture is seen in Northern Europe, the large number of events in and around Scandinavia and the Balticum are not observed by GERESS. After analyzing the few observations of these events by GERESS in more detail, we found that they all are misassociations and errors in the FEBs. A comparing study (Gestermann et al, 1991) of the observations at all GSETT-2 stations in Europe showed that all stations south west of the Teisseyre Tornquist Line (TTL) (Tornquist, 1911; Meissner et al., 1987) missed the events north east of the TTL. Vice verse all stations north east of the TTL have an unusual low detection capability for events south west of the TTL. This shows that the presence of a tectonic suture like the border between Eastern and Western Europe, drastically influences the detection capabilities of regional arrays and networks of seismic stations.

3.4 GERESS OBSERVATION OF THE AFTERSHOCK SERIES OF THE CAUCASUS EVENT (APR 29, 1991)

In the GSETT-2 period the largest event close to GERESS was an earthquake in the Western Caucasus on April 29, 1991 (42.454°N, 43.673°E, 09:12:48.1, $m_b = 6.2$, epicentral distance to GERESS 21.8°). After the main shock a series of aftershocks with hundreds of events occurred. A local network located 365 events within the GSETT-2 period with the Russian magnitude $k > 9$ (Starovoit, pers. communication). This value corresponds approximately with $m > 2.77$ (Russian conversion formula).

From the 365 events, 118 or 32.3 % were detected by GERESS. Fig. 3.10 shows the P-phase of the three smallest events ($k < 10$) which had been detected by GERESS (May 4, 1991, 04:53:39.5, $k = 9.6$, $\Delta = 21.49°$; May 6, 1991, 07:54:57.7, $k = 9.9$, $\Delta = 21.74°$; May 11, 1991, 04:57:08.7, $k = 9.8$, $\Delta = 21.86°$). Shown are the unfiltered traces at the GERESS key station GEC2 and Butterworth band pass (0.7 Hz - 3.0 Hz) filtered traces. The increase of the SNR is negligible. GERESS sent not only the unfiltered trace of key station GEC2 but also an unfiltered beam trace for every arrival to the EIDCs. Fig. 3.11 shows these beams for the three Caucasus onsets, once again unfiltered and filtered. The increase of the SNR is now obvious. The complexity of the P-phase is caused by different P-onsets of the upper mantle triplications.

To define a detection threshold for GERESS for the Caucasus region the cumulative number of events is plotted against their k-values in Fig. 3.12. The upper trace shows all occurring events and the lower line shows the events observed by GERESS.

3.5 TELESEISMIC CAPABILITIES

GERESS, designed as a regional array, also contributed remarkably to the teleseismic observations ($\Delta > 20°$). Every onset with an observed velocity of larger than 10 km/sec (or a slowness of less than 11.12 sec/deg) was defined as a teleseismic P-phase. A further distinction in direct P-waves, core phases, or later P-type onsets was not tried. Altogether GERESS reported 837 P-phases. From the 2985 events in the FEBs in teleseismic distance, GERESS detected 582 (19.5 %). Fig. 3.13 shows all events defined by the EIDCs and Fig. 3.13 the subset of these events to which at least one GERESS onset was associated.

The detection capability of GERESS is not limited to special distance ranges which can be demonstrated with Fig. 3.14. It shows all teleseismic events observed by GERESS with respect to their magnitude (maximum likelihood) in the FEBs. The detection capability only decreases for distances beyond $90°$, but increases again from about $120°$ for PKP phases. For distances between $140°$ to $155°$, around the PKP caustic, the detection threshold is similar to that at about $90°$. At $\Delta = 146°$, the PKP caustic is at its maximum which enables GERESS to detect events down to $m_b = 3.5 - 4.0$. This is the reason for the excellent monitoring capability of GERESS with respect to the French nuclear test sites in the Tuamotu Archipelago (Mururoa and Fangataufa) in the South Pacific. Three underground explosions from this test site were clearly recorded at GERESS during the GSETT-2 period (s. Chapter 4 in this Report).

A teleseismic detection threshold of GERESS can be estimated from Fig. 3.16. The cumulative number of all observed events with respect to all occurring events in the FEBs shows that GERESS missed worldwide no event with $m_b > 5.3$ and observed more than 50 % of all events with $m_b > 4.2$.

The good teleseismic detection capability of GERESS is caused mainly by the general low noise level at frequencies around 1 Hz and the application of array techniques. On the other hand, we clearly see that man-made noise (mining and industrial activity) increased during day time. This increased cultural noise diminished the detection capability for teleseismic events. Consequently, we observed fewer P-phases during general working hours. During this time (UT) of the day, the number of reported teleseismic arrivals decreased by 30 % (Fig. 3.17). The local time was two hours earlier than UT.

We cannot expect, that the GERESS array with its small aperture of about 4 km can observe slowness and azimuth for teleseismic phases with the same accuracy as larger arrays (e. g. Gräfenberg, NORSAR, Yellowknife). Therefore a point of general interest is: how accurate are the observed azimuth and slowness values and do the mislocation vectors show any systematic pattern?

To investigate this problem, we calculated the theoretical slowness and azimuth (from station to epicenter) values and their residuals for about 350 teleseismic FEB events. We used the IASPEI 1991 tables to estimate the theoretical slowness. To reduce the scatter in the data and the influence of observed slowness and azimuth errors at GERESS, we only used events, which had been located by the EIDCs with more than 15 defining phases.

A first analysis shows that the residuals for azimuth and relative slowness (i. e. $(p_{obs} - p_{theo})/p_{theo}$) increase with epicentral distance - as expected. The azimuth residuals (Fig. 3.18) are $+/- 30°$ for distances less than $70°$ and increase rapidly to $+/- 60°$ for larger distances. Only few observations (about 2 %) show residuals of more than $+/- 90°$. The observed relative slowness residuals (Fig. 3.19) show a similar pattern. We observe slowness variations of up to $+/- 60$ % for P- and P_{diff}-phases and an increase of slowness variations to $+/- 100$ % for PKP-phases.

If these preliminary mislocation vectors are plotted in the slowness space (Fig. 3.20), we see - besides the large scatter in the data - some systematic effects: The slowness observations - without the PKP_{DF} observations from the north-east - are rather too small than too large. Wether this effect is influenced by the array transfer function of GERESS, needs further investigations.

The mean value of the azimuth residuals is positive for observations from the north and northeast. For the azimuth range from $40°$ to $80°$ we observe negative residuals which change again to positive residuals for events directly from the east. For the azimuth range between $250°$ and $300°$, we once again observe a change in the sign of the residuals from negative to positive. All other directions are not well constrained by FEB events.

The GERESS mislocation vector field in the slowness space shows some similarities - especially for observations from the north and east - with the mislocation vectors of the Gräfenberg array (Faber et al., 1986; Krüger and Weber, 1992). These authors explained most of the mislocation of GRF as a laterally heterogeneous velocity structure in the crust and in the upper mantle under the GRF array and north-north-east from GRF under the Bohemian Massive. Whether we see the same effects in GERESS mislocations by chance, or the mislocations of both arrays are caused by commonly seen larger heterogeneous structures, will be investigated in a joint interpretation of GRF and GERESS mislocation vectors.

3.6 CONCLUSIONS AND RECOMMENDATIONS

After one year of data recording and analysis it is obvious that GERESS is the most sensitive station in Central Europe for monitoring local, regional, and teleseismic seismicity as demonstrated by the results of the GSETT-2 experiment. During the time of the experiment, GERESS located on average 16 events per day within $5°$ distance. In addition, an average of 12 teleseismic events per day were observed. These results motivated the GERESS group in

ery interested institution.

GERESS shows an azimuthaly varying detection capability within regional distances which seems to be related to a major suture zone in Central Europe (e. g. TTL) effectively blocking regional seismic energy.

For teleseismic observations the GERESS array is also very sensitive. The observed slowness and azimuth values for P- and PKP-phases can be used for a first order event location, with increasing error bars for larger distances.

To increase the location accuracy for all distance ranges from GERESS, a calibration of the array is necessary.

LITERATURE

Båth, M., O. Kulhánek, T. van Eck, R. Wahlström (1976). Engineering analysis of ground motion in Sweden, *Report No. 5-76*, Seismological Institute, Uppsala, Sweden.

Gestermann, N., M. L. Jost, and J. Schweitzer (1991): Performance of the new German Experimental Regional Seismic System (GERESS) during GSETT-2 (Abstract), *EOS, Trans. Am. Geoph. Union* 72, Suppl. Oct. 29, 1991, 354.

Faber, S., J. Plomerová, V. Babuška (1986). Deep-seated lateral velocity variations beneath the GRF array inferred from mislocation pattern and P residuals, *J. Geoph.* 60, 139-148.

Krüger F. and M. Weber (1991). The effect of low-velocity sediments on the mislocation vectors of the GRF array, *Geophys. J. Int.* 108, 387-393.

Meissner, R., T. Wever, E. R. Flüh (1987). The Moho in Europe - Implications for crustal development, *Ann. Geophys.* 5B, (4), 357-364.

Mykkeltveit, S. and H. Bungum (1984). Processing of regional seismic events using data from small- aperture arrays, *Bull. Seism. Soc. Am.* 74, 2313-2333.

Tornquist, A. (1911). Die Tektonik des tieferen Untergrundes Norddeutschlands, *Sitzungsberichte der königlich preussischen Akademie der Wissenschaften*, 38, 27.7.1911, 822-836.

Wüster, J. (1991). Signal transfer functions and sensitivities for GERESS seismometers, in *Advanced Waveform Research Methods for GERESS Recordings*, DARPA Annual Report No. AFOSR-90-0189, 11-27. PL-TR-91-2134, ADA239199

- 32 -

FIGURE CAPTIONS

Fig. 3.1: All events located by GERESS during the GSETT-2 experiment from April 22, 1991 to June 2, 1991.

Fig. 3.2: Number of events located by GERESS with respect to their epicentral distance.

Fig. 3.3: Number of events per hour located by GERESS with respect to the day of week. The data were corrected for national holidays and GERESS outages.

Fig. 3.4: Number of events located by GERESS versus time of day (UT).

Fig. 3.5: Observed ML values of the events located by GERESS versus epicentral distance. The two lines show the amplitude distance relations for Scandinavia (lower curve) and the now at GERESS used relation (upper line).

Fig. 3.6: Comparison between GERESS and NEIC locations for 58 common events during the GSETT-2 period.

Fig. 3.7: The network of GSETT-2 stations in and around Europe.

Fig. 3.8: All events located by the EIDCs in and around Europe.

Fig. 3.9: As Fig. 3.8, but now only for these events which had been detected by GERESS.

Fig. 3.10: Unfiltered and filtered vertical traces from station GEC2 of three small event in the Western Caucasus. The events were: May 4, 1991, 04:53:39.5, k=9.6, Δ = 21.49°; May 6, 1991, 07:54:57.7, k=9.9, Δ = 21.74°; May 11, 1991, 04:57:08.7, k=9.8, Δ = 21.86°. The amplitudes (on the right) are given in counts and the start time of the traces is given on the left.

Fig. 3.11: As Fig. 10, but now for the array beams respectively.

Fig. 3.12: The cumulative number of all events in the Western Caucasus during GSETT-2 (crosses) and the cumulative number of these events seen by GERESS (triangles).

Fig. 3.13: All FEB events in teleseismic distances (Δ > 20°) from GERESS.

Fig. 3.14: As Fig. 13, but now only for the events detected by GERESS.

Fig. 3.15: The epicentral distance of all FEB events detected by GERESS

plotted versus magnitude.

Fig. 3.16: The cumulative number of all FEB events (crosses) and the cumulative number of these events seen by GERESS (triangles).

Fig. 3.17: Number of P-phases reported by GERESS with respect to the time of day (UT). Local time was two hours earlier than UT.

Fig. 3.18: Observed residuals of reported backazimuths with respect to the theoretical value (FEB source parameter).

Fig. 3.19: Relative slowness residuals (p_{obs} - p_{theo})/p_{theo}) between the reported slowness values and the theoretical values from IASPEI 1991 Tables.

Fig. 3.20: Mislocation vectors for about 350 FEB events observed with GERESS. The symbols represent the theoretical values.

GERESS-EVENTS APR 22, 1991 - JUN 2, 1992
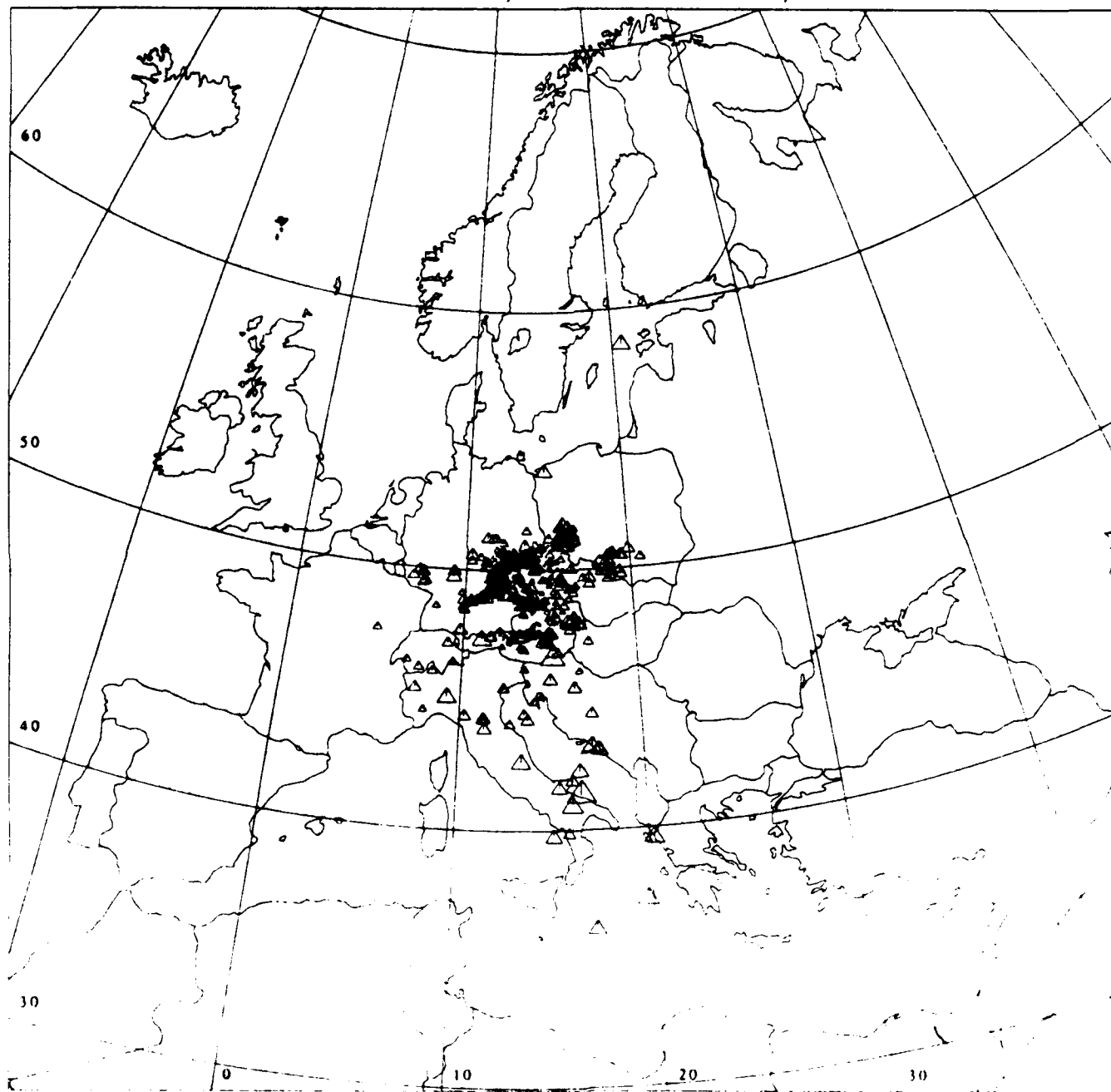
Figure 3-1
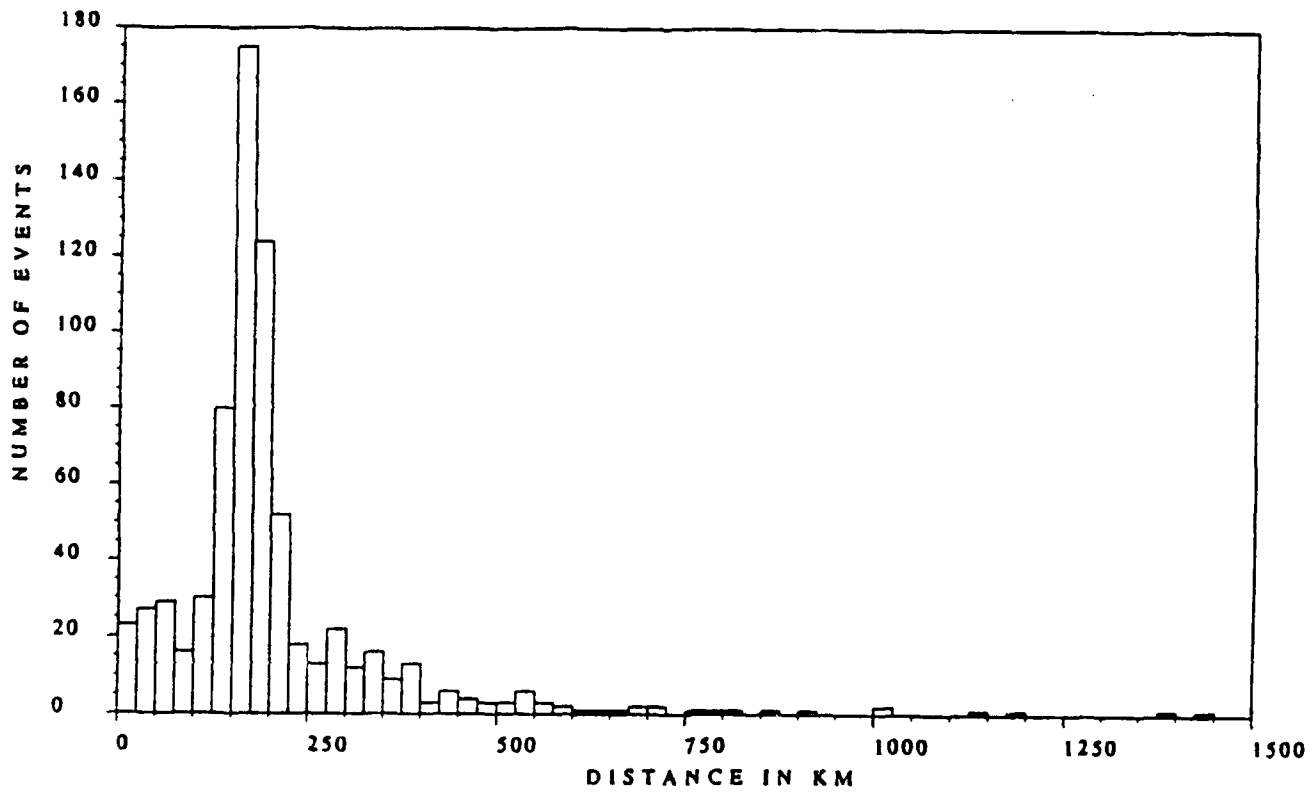
Figure 3-2
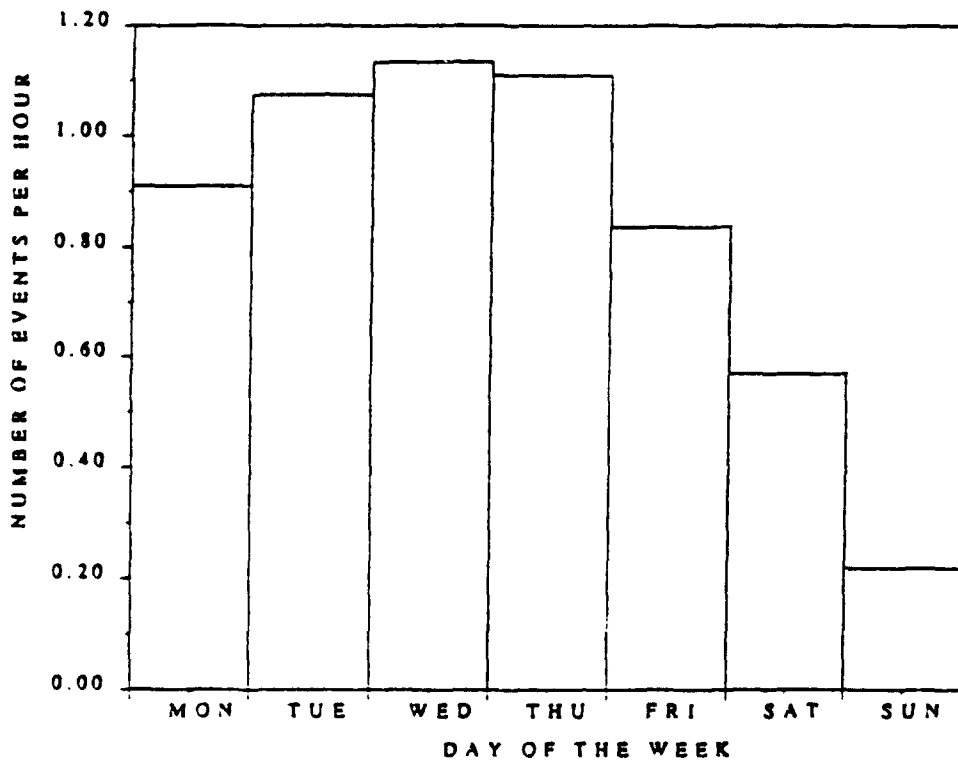
Figure 3-3
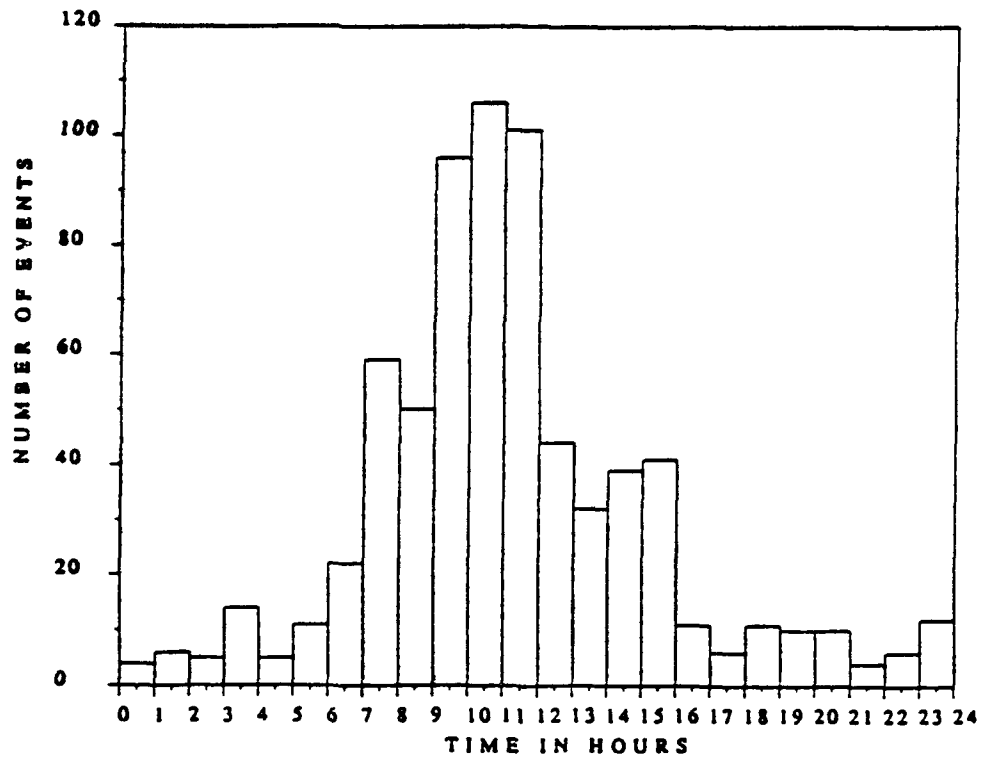
Figure 3-4
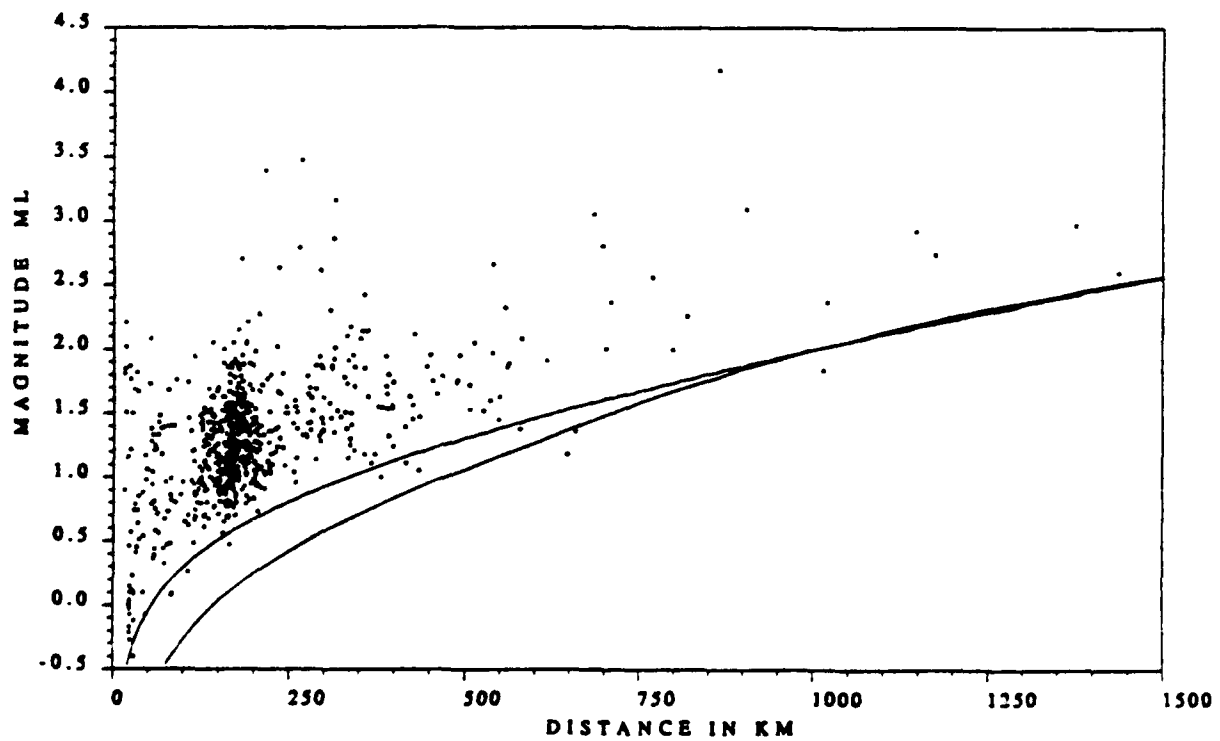
Figure 3-5

COMPARISON EDR's - GERESS BULLETIN
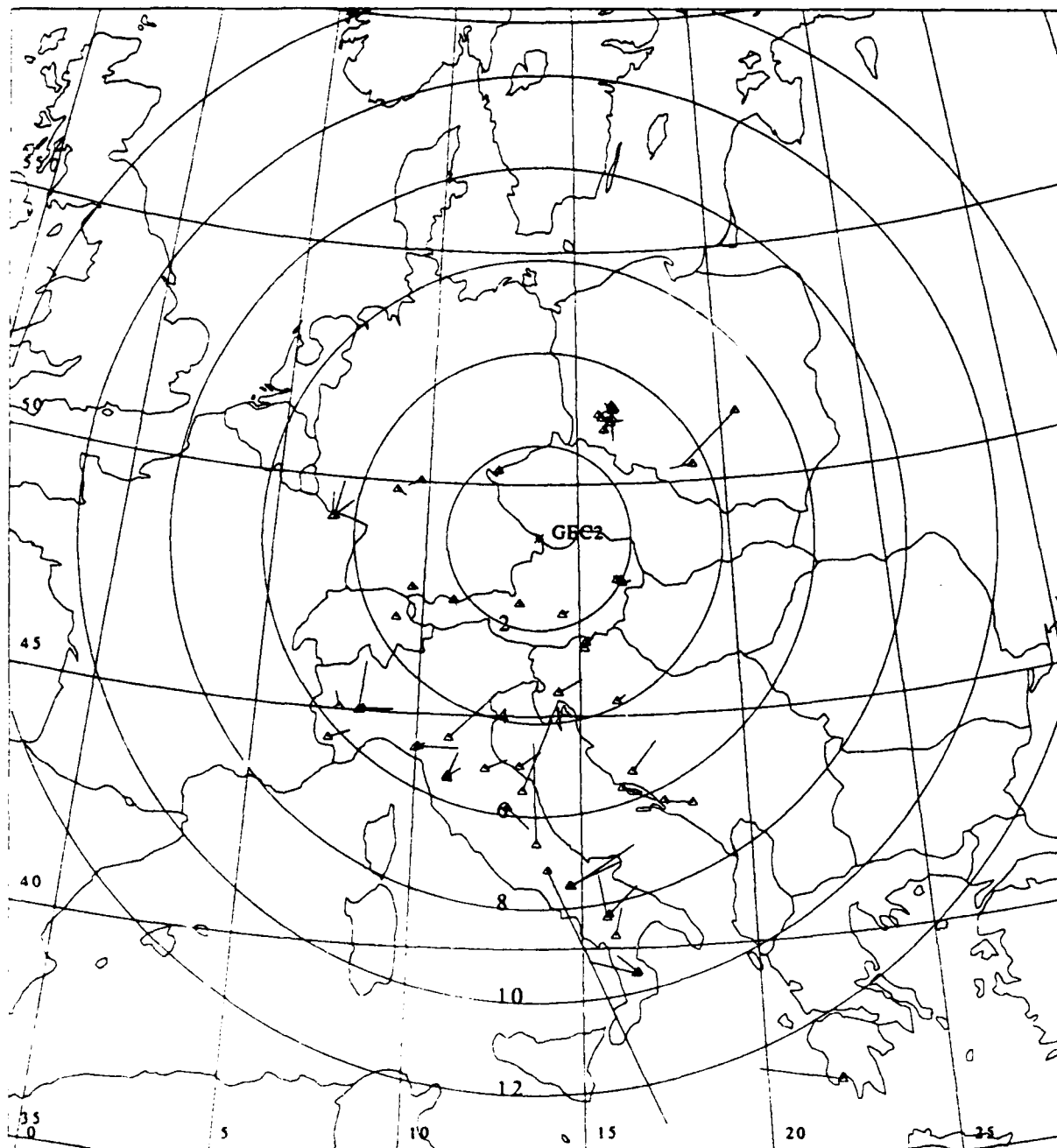
Figure 3-6
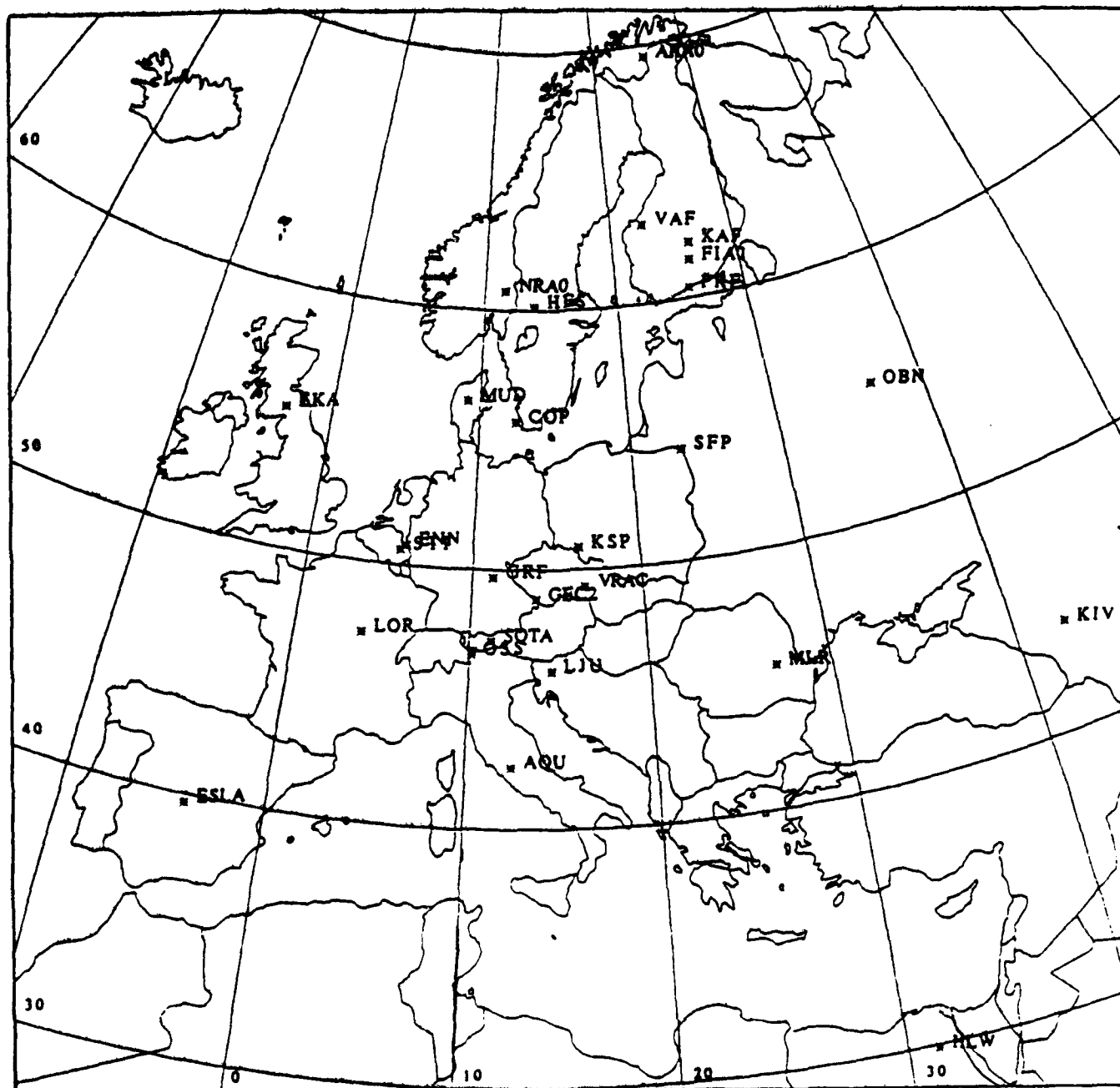
Figure 3-7

ALL OBSERVED EVENTS (FEB) APR 22, - JUN 2, 1991
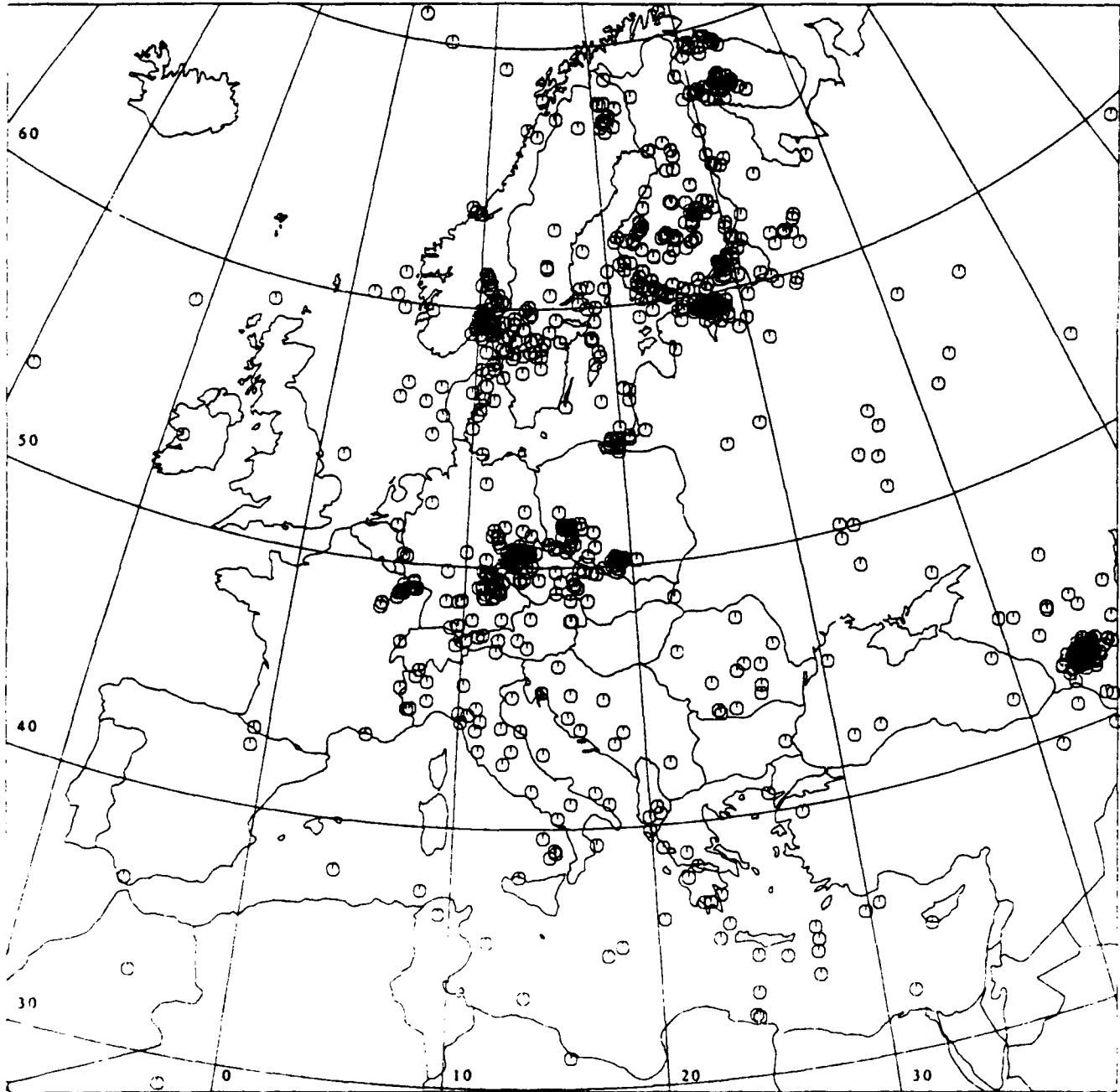
Figure 3-8

GERESS OBSERVED EVENTS (FEB) APR 22, - JUN 2, 1991

Figure 3-9

- 41 -

MAY_GEC2.sz

Figure 3-10

Figure 3-11

CAUCASUS EVENTS OBSERVED WITH GERESS

Figure 3-12

ALL EVENTS (FEB) 1991, 112 - 1991, 153 DELTA > 20DEG
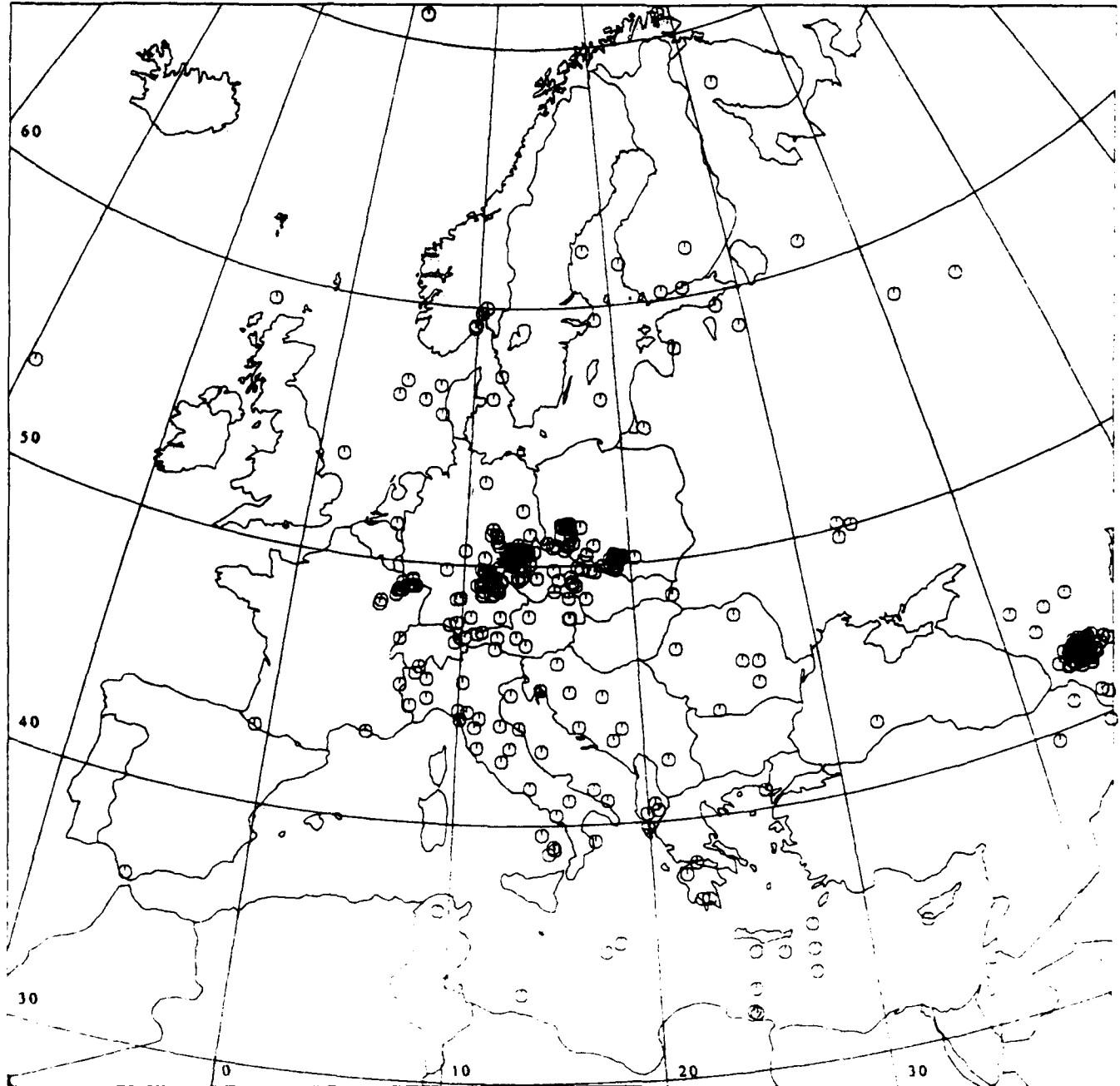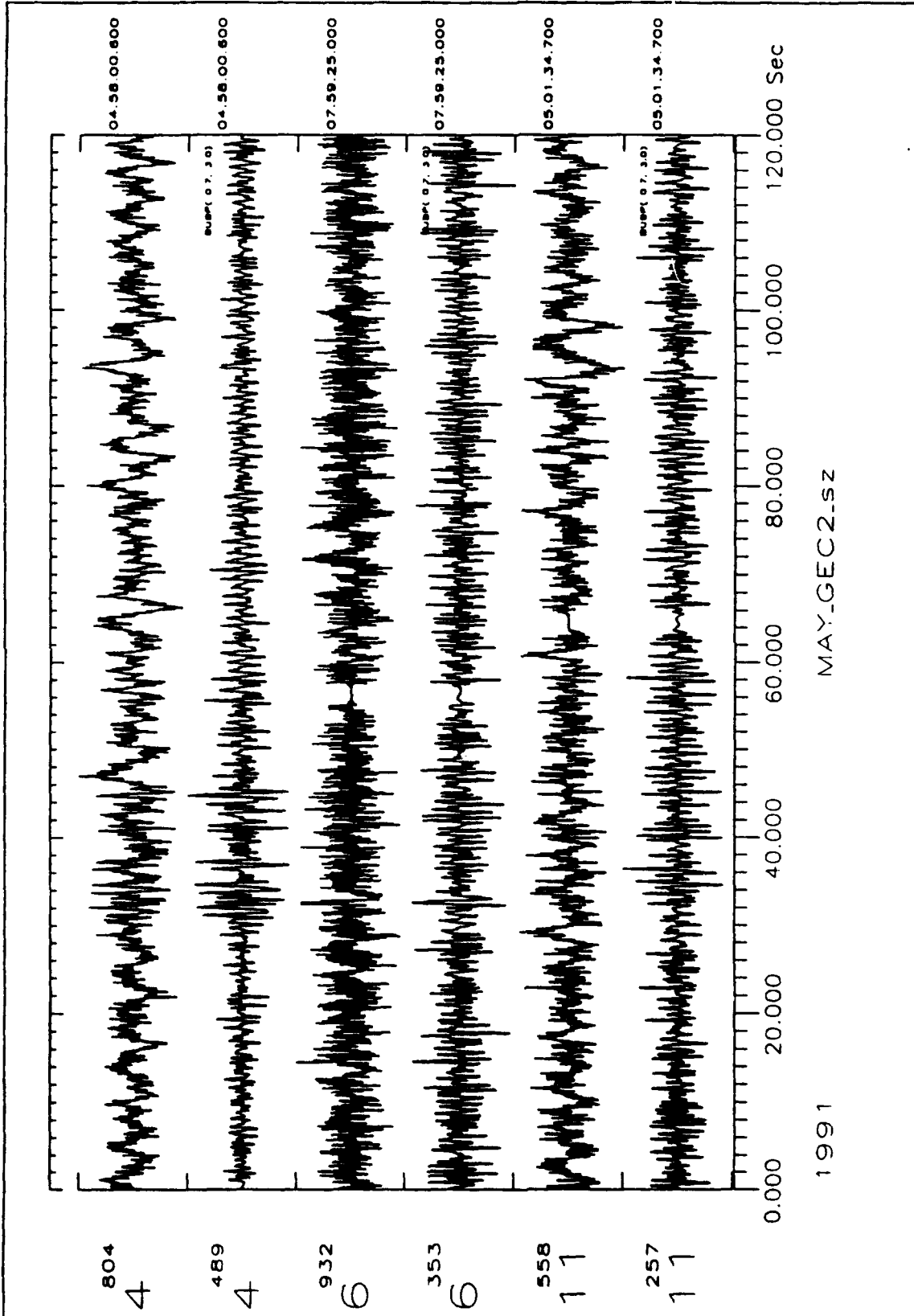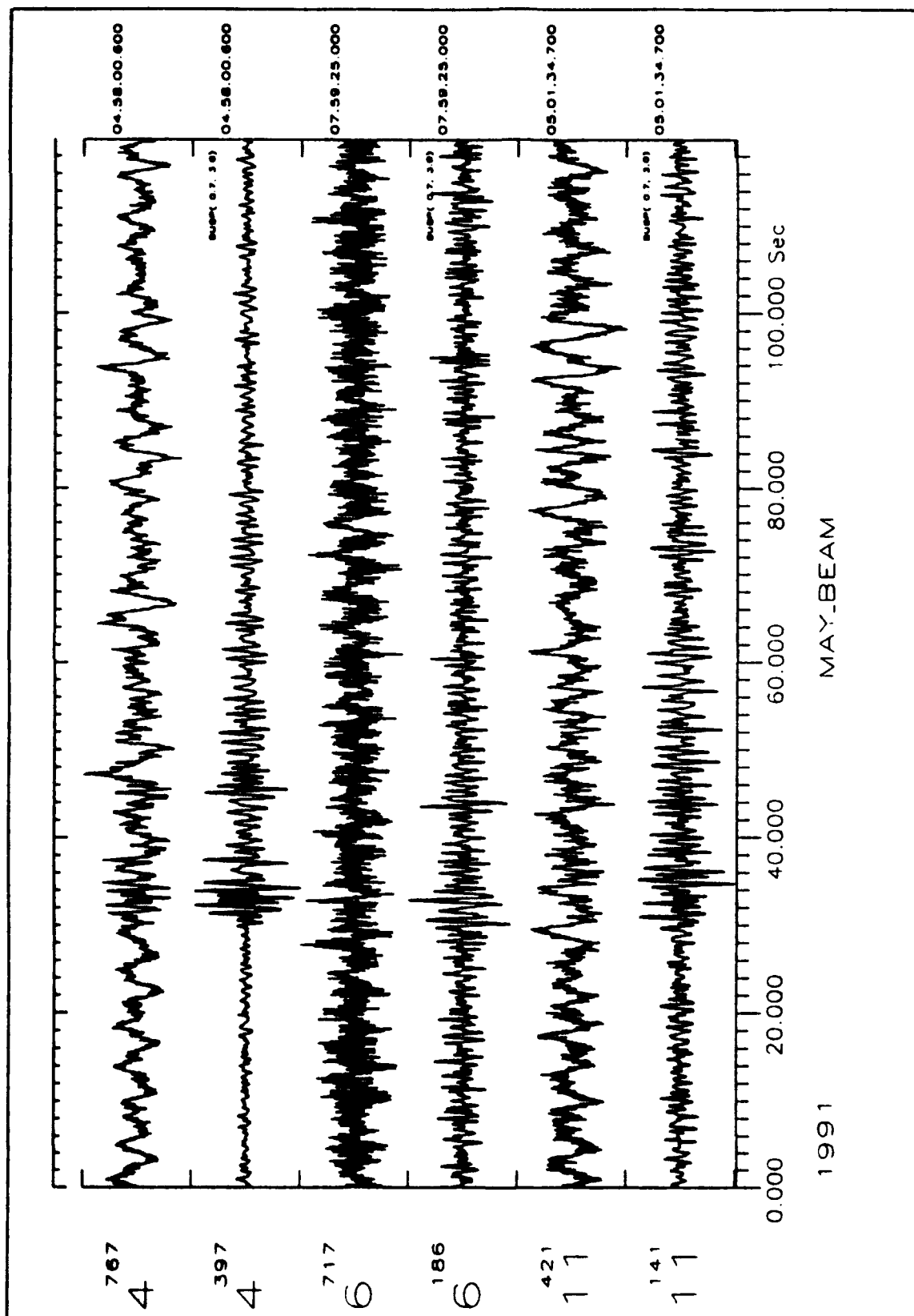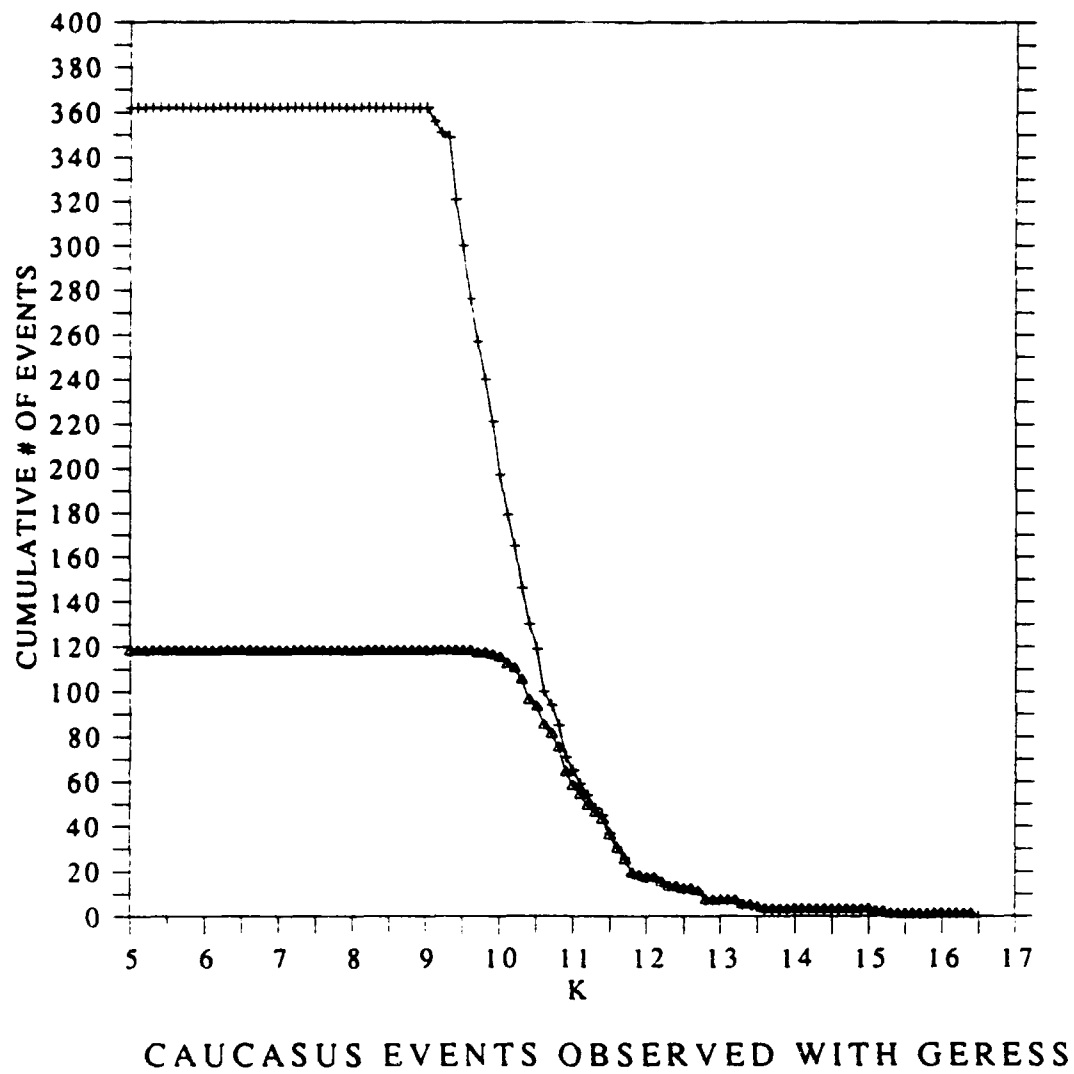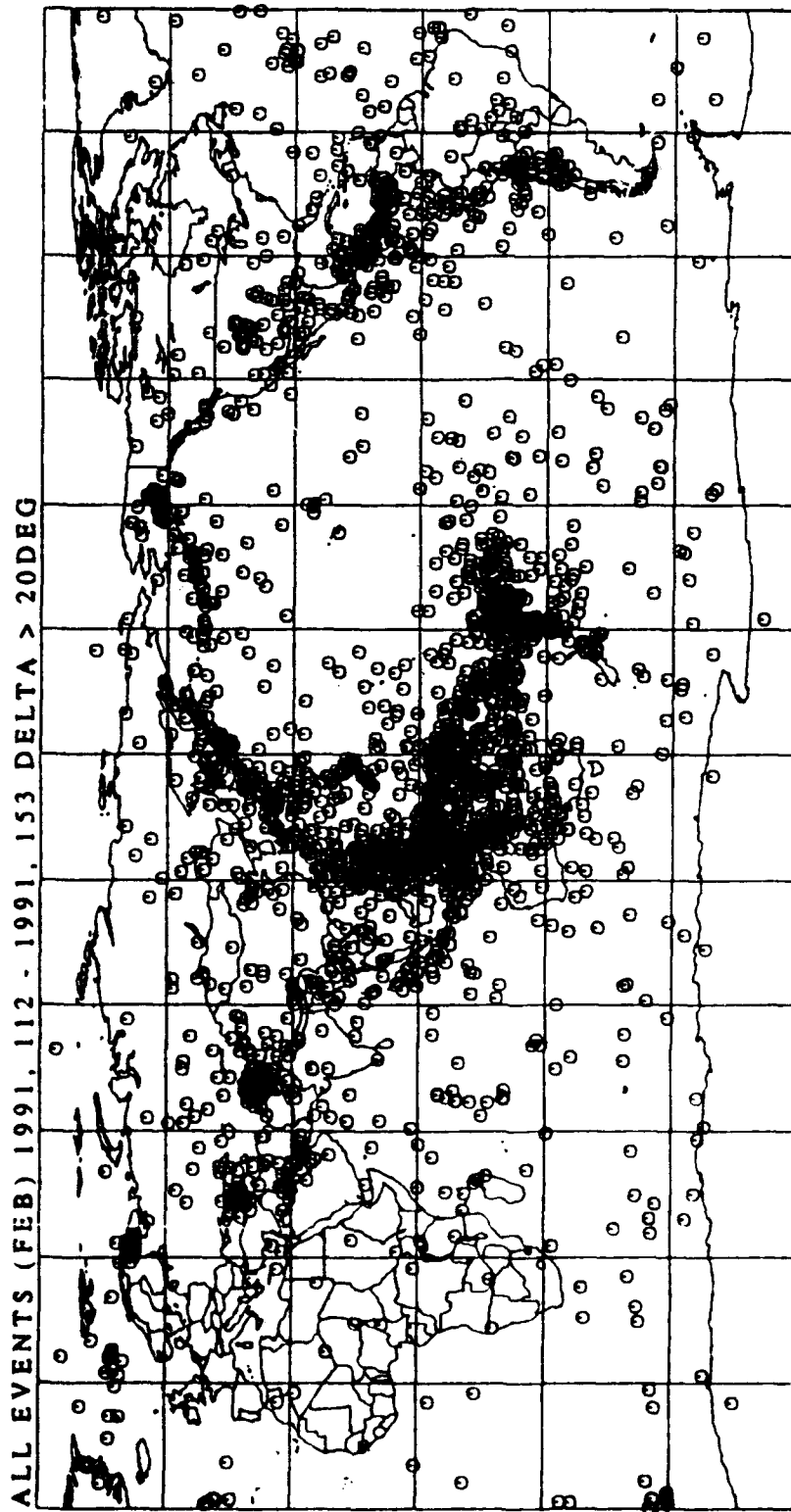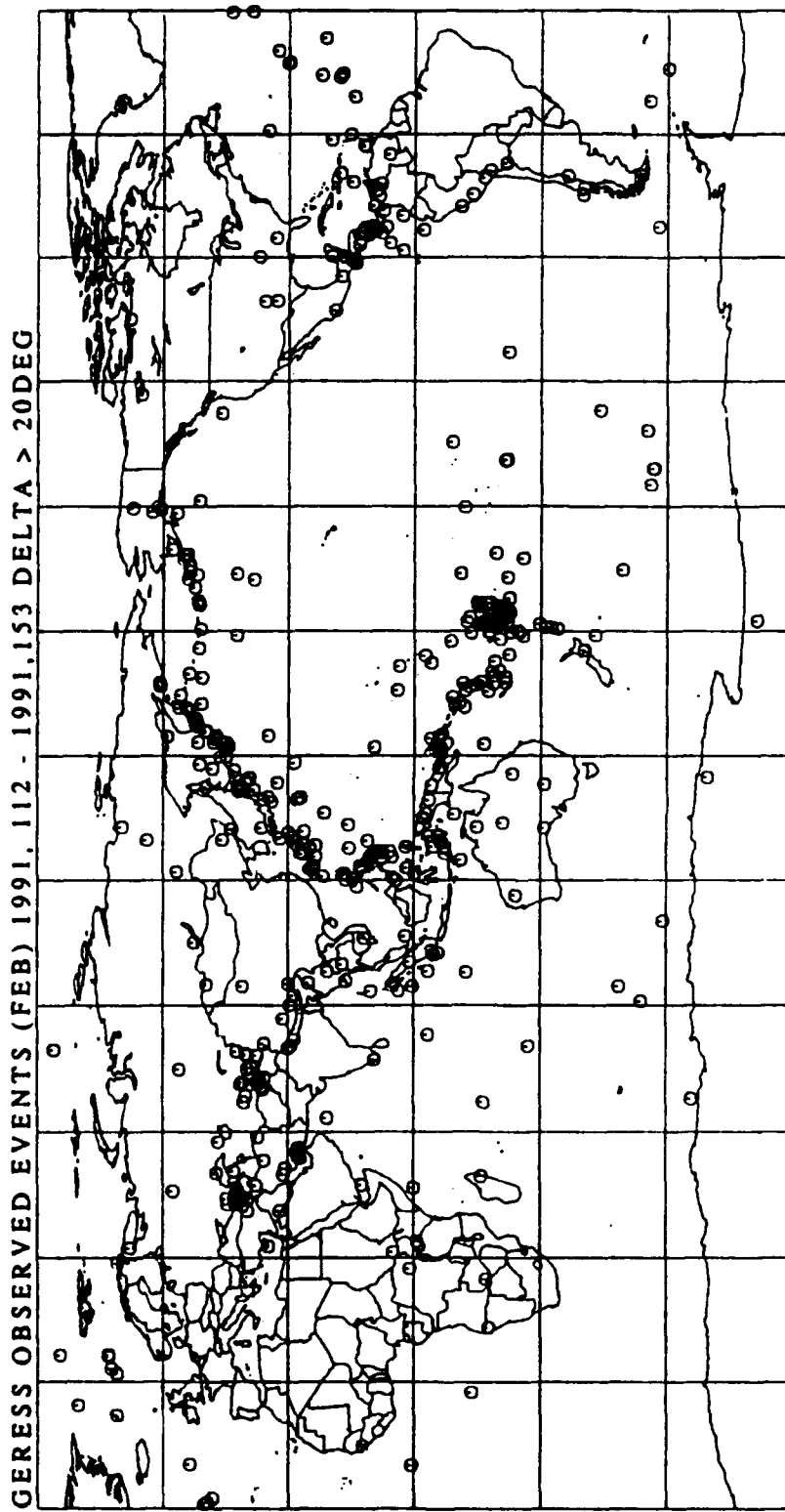
Figure 3-13
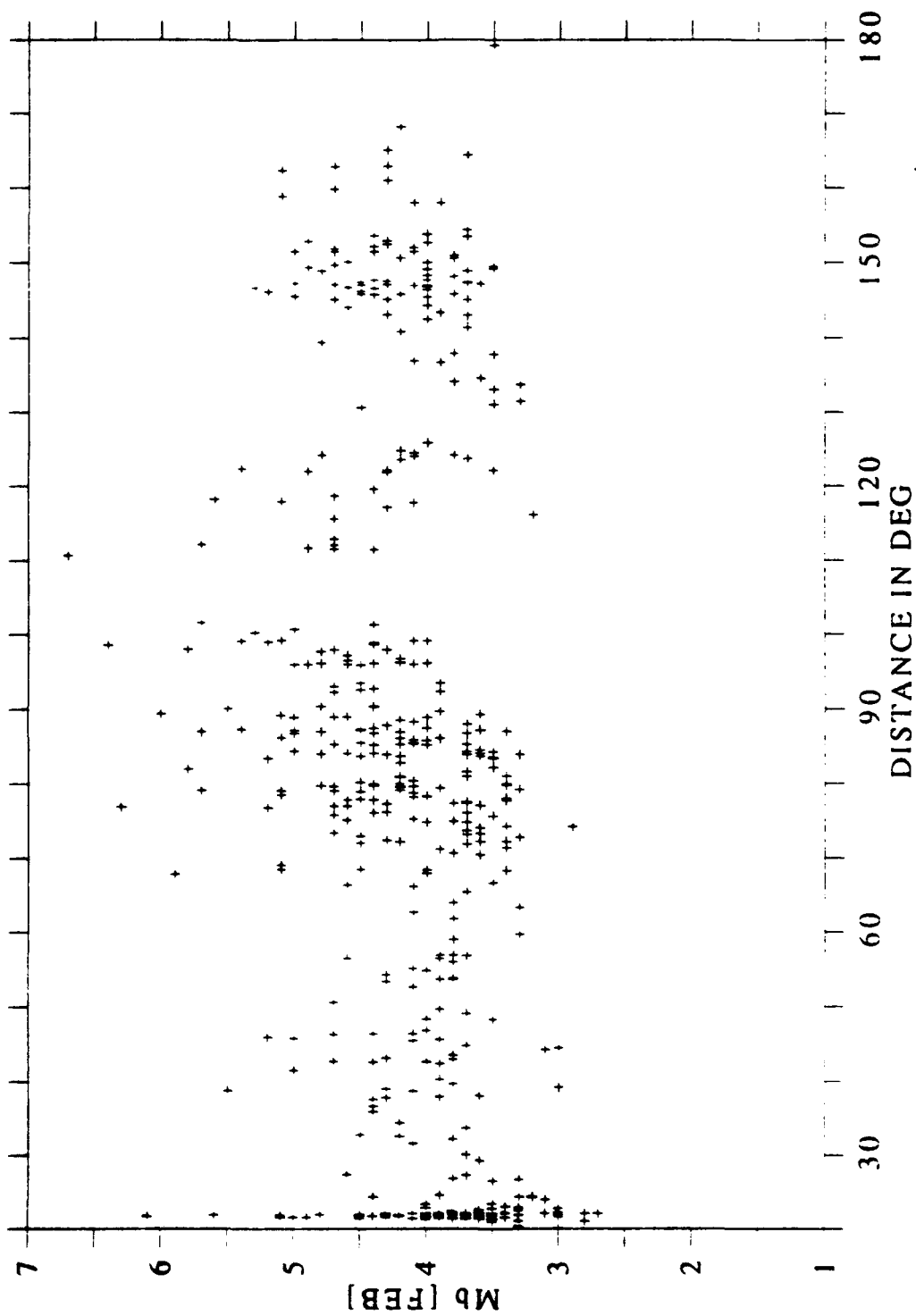
Figure 3-14

EVENTS OBSERVED WITH GERESS Apr 22, - Jun 2, 1991

Figure 3-15
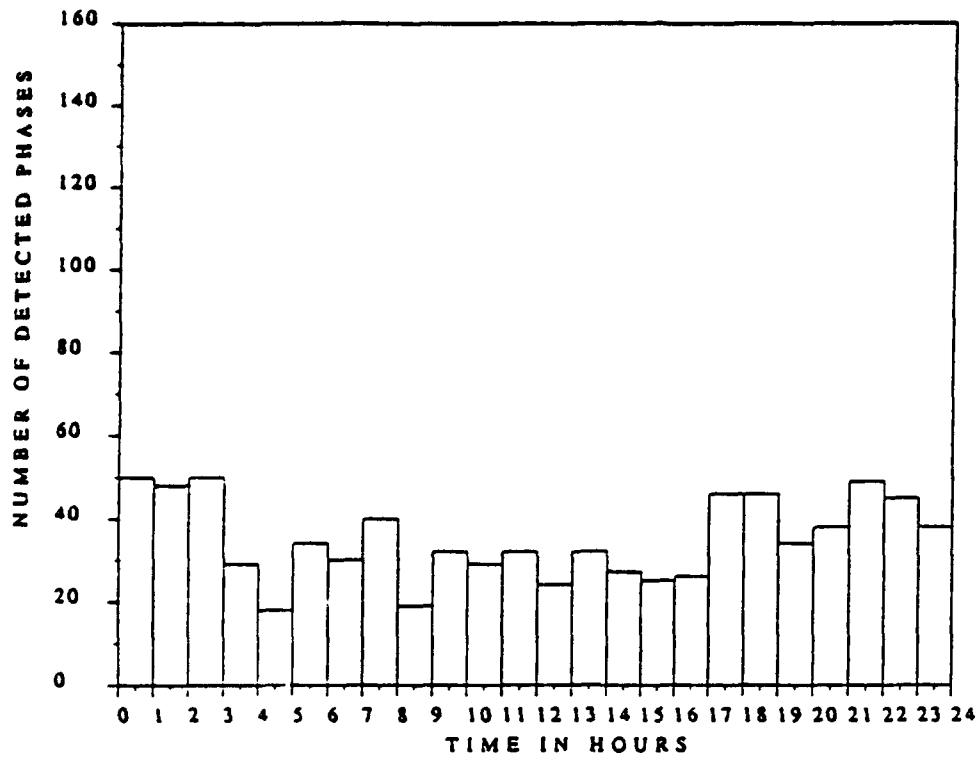
Figure 3-16
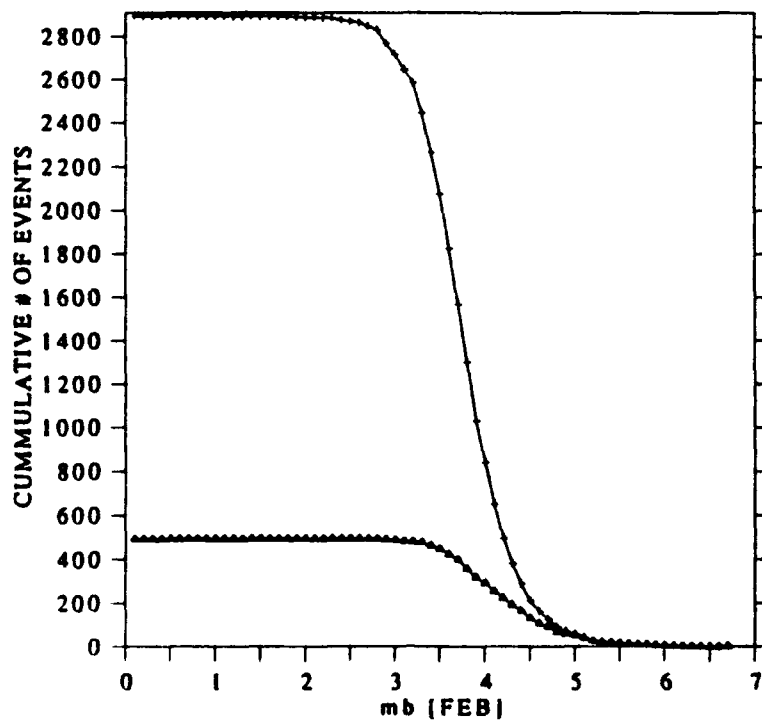
Figure 3-17
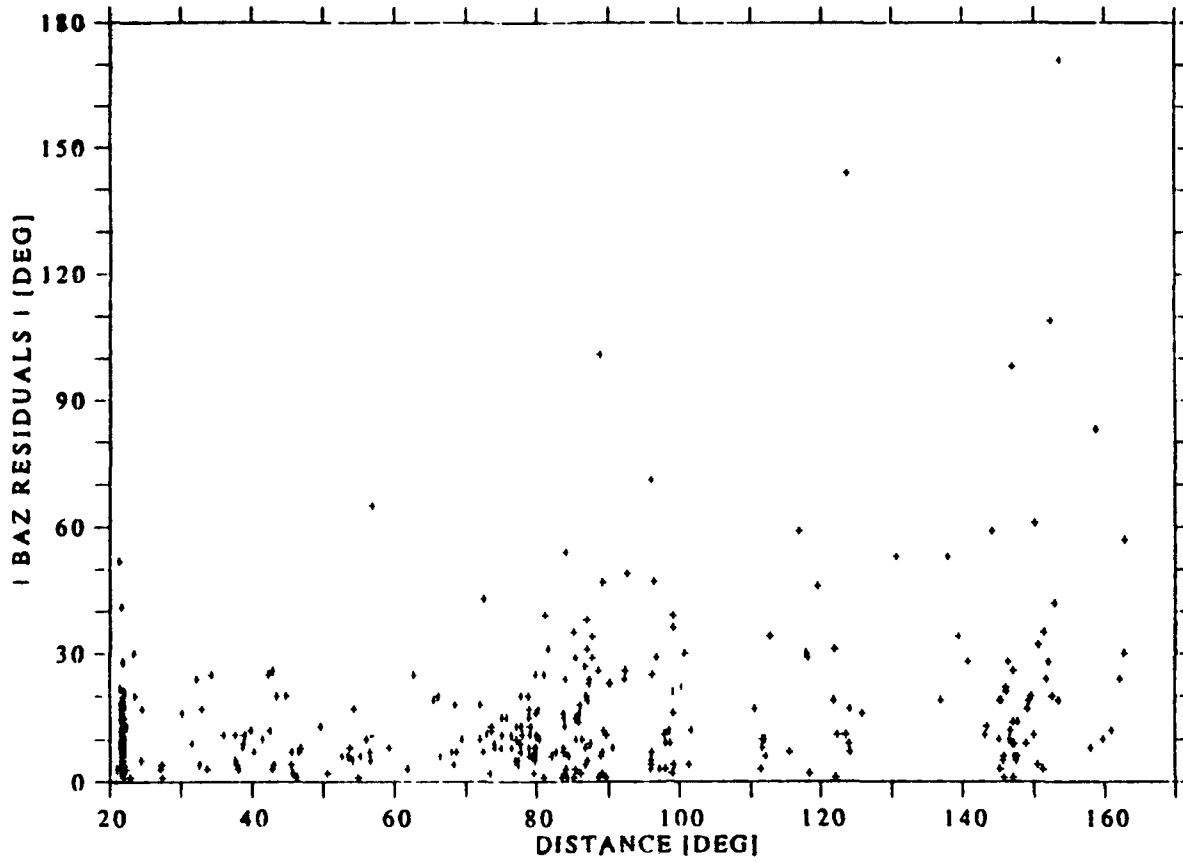
Figure 3-18
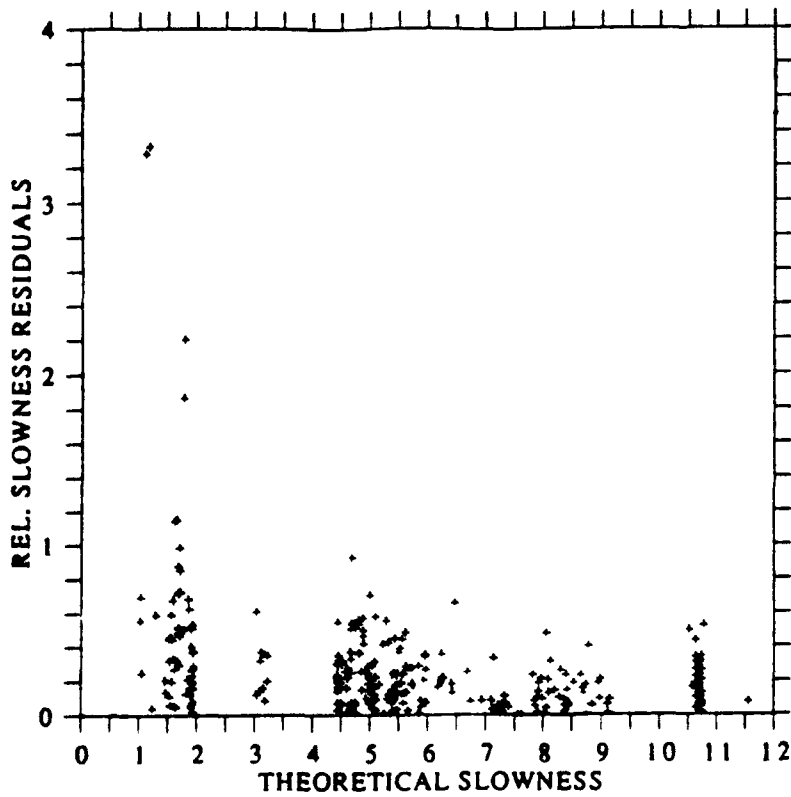
Figure 3-19
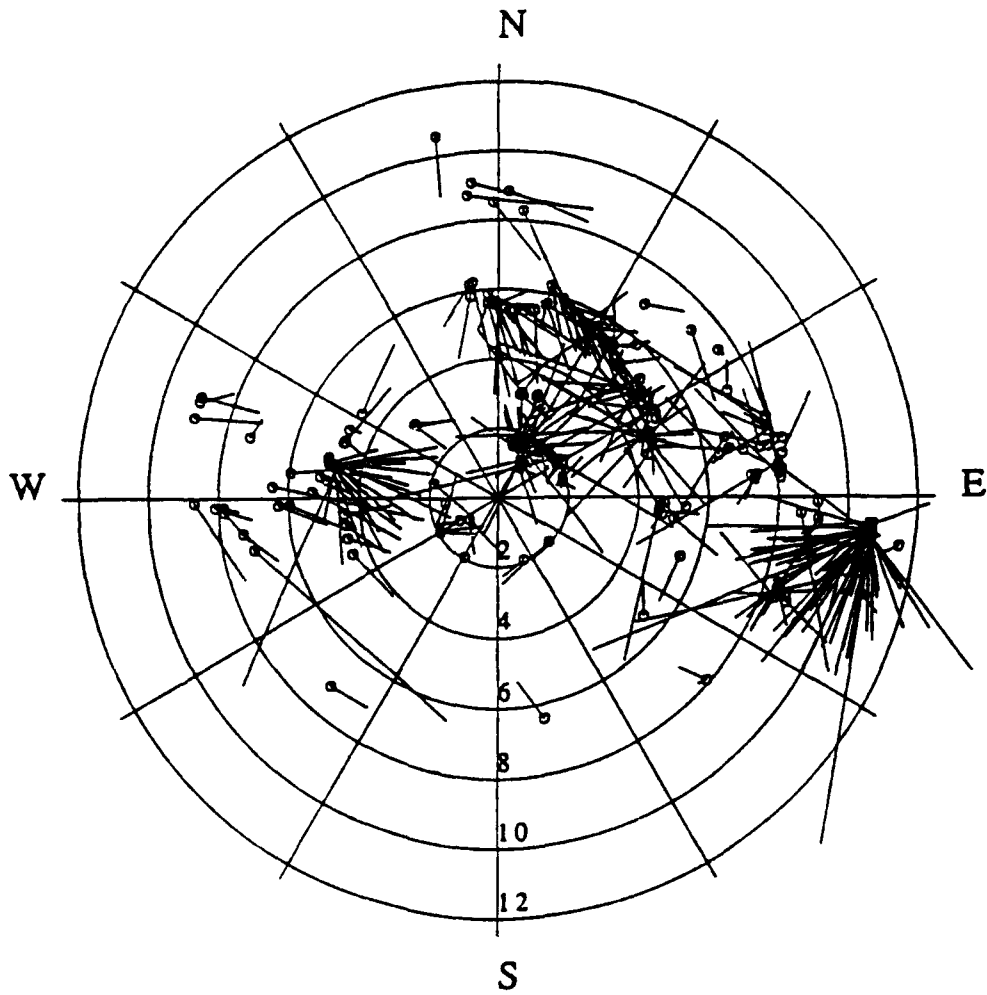
Figure 3-20

4. NUCLEAR TESTS OBSERVED WITH THE GERESS ARRAY IN 1991

Johannes Schweitzer, Michael L. Jost, Nicolai Gestermann

4.1 INTRODUCTION

As in 1990, GERESS observed most of the presumed nuclear tests in 1991. The absolute number of known nuclear tests decreased, because neither the Soviet Union nor China tested their weapons last year. The number of tests in the Tuamotu Archipelago of France and at the Nevada Test Site in USA was once again 6 and 8, respectively. In this chapter we want to continue the report about all nuclear tests observed at GERESS (Schweitzer, 1990).

Country	Test Site	Epicentral Distance	# of Tests	# of GERESS Observations
France	(Mururoa)	145.4°	5	4
France	(Fangataufa)	145.6°	1	1
USA	(Nevada)	83.5°	8	6

The differences between the total number of tests (14) and the number of recorded events (11) is caused by explosions, which were too small (3) to produce an observable signal at the GERESS site.

In the following, a description is given of all observations of presumed nuclear explosions from the different test sites. The data are shown either unfiltered or filtered with a third order Butterworth bandpass (pass 2) from 0.5 Hz to 2.5 Hz. The general results of the analysis are listed in Tab. 4-1. Station GEC2 was used as reference for all investigations (fk-analysis and beam forming). All times, amplitudes, signal to noise ratios (SNR), and periods have been measured on the beams.

Location	Date		Onset Time	Ampli. [nm]	Period [sec]	SNR Ampli.	m_b	BAZ [deg]	P [sec/deg]
Nevada	Mar	08	21:15:15.1	1.77	1.01	3.2	4.2	306.3	4.16
Nevada	Apr	04	19:12:29.2	38.31	1.21	58.9	5.5	326.0	3.65
Nevada	Apr	16	15:42:29.5	18.57	0.99	48.1	5.3	331.8	3.64
Mururoa	May	07	17:19:39.4	2.14	0.72	6.9	-	308.0	2.02
Mururoa	May	18	17:34:39.6	22.69	0.81	86.4	-	331.1	2.59
Fangataufa	May	29	19:19:39.6	120.49	1.46	141.3	-	330.0	2.65
Mururoa	Jun	14	18:19:39.2	37.99	0.93	135.4	-	329.9	2.65
Mururoa	Jul	15	18:29:39.4	42.65	0.81	91.8	-	318.5	2.71
Nevada	Sep	14	18:12:29.9	42.35	1.19	121.7	5.6	330.5	3.36
Nevada	Oct	18	19:24:29.9	14.99	1.02	19.3	5.4	322.6	3.28
Nevada	Nov	16	18:47:30.0	5.12	1.13	10.9	4.7	338.9	4.36

Tab. 4-1: Observed parameters of presumed nuclear tests recorded at GERESS in 1991.

4.2 FANGATAUFA and MURUROA

The recordings of presumed nuclear tests at the French Test Sites Mururoa and Fangataufa in 1991 confirmed the excellent detection capability of GERESS for this region. In 1991, 6 known tests occurred and only one of these explosions was not detected by GERESS (Jul 15, 1991; 18:00). This test was very small and was only observed by the seismic station Raratonga (RAR). The yield of this explosion was estimated as less than 0.3 kt TNT from the T-phase at RAR (Smith, pers. communication).

Because the body wave magnitude m_b is not defined for events with an epicentral distance of more than about 100°, no direct m_b estimation is possible for these explosions from GERESS. Therefore we corrected the observed log (A/T) values with the attenuation curve of Blandford and Sweetser (1973) for PKP-phases. The m_b(PKP)-values for the French explosions were determined with the correction value of 3.50 for an epicentral distance of 145.5°. The results for all events in 1990 and 1991 can be found in Tab. 4-2. For 9 of these events our m_b(PKP)-values can be compared with "conventional" m_b-determinations by NEIC. The agreement between both m_b-values is satisfactory taking in account that the GERESS station magnitude is not calibrated with NEIC network magnitudes.

Date dd-mm-yy	Time hh:mm	G E R E S S Amplitude [nm]		Period [sec]	m_b (PKP)	NEIC m_b	DSIR Yield [kt]
02-06-90	17:30		32.69	0.88	5.07	5.3	30
07-06-90	17:30		5.77	0.90	4.31	-	3
26-06-90	18:00	F	148.54	1.57	5.48	5.5	100
04-07-90	18:00		14.68	0.87	4.73	5.1	18
14-11-90	18:12	F	142.79	1.50	5.48	5.5	117
21-11-90	16:59		64.65	0.81	5.40	5.4	36
07-05-91	17:00		2.14	0.72	3.97	-	1
18-05-91	17:15		22.69	0.81	4.95	5.1	16
29-05-91	19:00	F	120.49	1.46	5.42	5.5	107
14-06-91	18:00		37.99	0.93	5.11	5.2	28
05-07-91	18:00	*	<0.80	1.30	<3.30	-	<0.3
15-07-91	18:10		42.65	0.81	5.22	5.3	34

F - event probably on Fangataufa

* - event not observed, parameters measured on noise

Tab. 4-2: Amplitude and magnitude observations of French nuclear tests in
1990 and 1991.

Fig. 4-1 shows the estimated m_b(PKP)-values for all events observed with
GERESS in 1990 and 1991 plotted against the yields estimated with the Rara-
tonga T-phases (W. Smith, pers. communication). The line follows the linear
relationship (least square fit) between log(yield) and m_b(PKP)-values:

$$\log_{10}(\text{yield}) = 1.256 \cdot m_b \text{ (PKP)} - 4.930$$

The two dotted lines give the upper limits for the smallest not observed
explosion. This leads to the conclusion, that the GERESS detection threshold is
about m_b(PKP) = 3.6 (yield = 0.5 kt).

Fig. 4-2 and Fig. 4-3 show all presumed French nuclear tests as observed
by GERESS. All traces are beams with the parameters of Tab. 6-1 in the 1990
Report (Schweitzer, 1990) or with the parameters of Tab. 4-1. The beams are
plotted unfiltered (Fig. 4-2) and filtered (Fig. 4-3). The uppermost trace is the
theoretical beam for the PKP-onset of the event on Jul 05, 1991 which was not
observed at GERESS. The French authorities do not publish any parameters of
their tests, therefore the start time of all traces is always 19 minutes and 30
seconds after an assumed shot time at full minutes respectively.

4.3 NEVADA

Six of eight nuclear tests at the Nevada test site (NTS) were observed with the GERESS array. The calculated m_b-values are in good agreement with the network magnitudes published by NEIC (EDR or PDE) as can seen in Tab. 4-3.

Date		m_b GERESS	m_b NEIC	SNR	Det. Thr. [m_b]
1990 Jun	13	5.7	5.7	93.5	4.3
1990 Jul	25	4.7	4.7	8.3	4.4
1990 Oct	12	5.5	5.6	55.9	4.5
1990 Nov	14	5.4	5.4	59.1	4.2
1991 Mar	08	4.2	4.3	3.2	4.3
1991 Apr	04	5.5	5.6	58.9	4.3
1991 Apr	16	5.3	5.4	48.1	4.2
1991 Sep	14	5.6	5.5	121.7	4.0
1991 Oct	18	5.4	5.2	19.3	4.5
1991 Nov	26	4.7	4.6	11.0	4.2

Tab. 4-3: Magnitudes and detection thresholds for the NTS-explosions in 1990 and 1991.

A mean mean detection threshold of m_b (GERESS) = 4.3 is estimated using with 10 (1990 and 1991) NTS-events. This implies a threshold of the GERESS STA/LTA detector of 4.0. Consequently GERESS did not detect the small explosion on Mar 08, 1991 with m_b = 4.3 (NEIC) and m_b = 4.2 (GERESS). But in hindsight, a coherent signal at all GERESS traces was detected at the theoretical onset time for a P-phase of this event with a SNR of 3.19. The results of the fk-analysis deviate from normal values for NTS-shots (s. Tab. 4-1) probably due to the low SNR.

Fig. 4-4 shows all NTS events recorded by GERESS in 1990 and 1991. The unfiltered traces are beams sorted with respect to the m_b-values (NEIC). Note that the smallest event is not seen on the unfiltered uppermost seismogram. Fig. 4-5 shows all filtered beams and the small explosion of Mar 08, 1991 becomes visible. The comparison with the other seismograms confirms our interpretation of this onset by the similarity of the pulse form.

Fig. 4-4 and Fig. 4-5 show another remarkable effect. All starting times of the seismograms were chosen as follows: We calculated the theoretical onset time with the IASPEI 1991 travel time tables for these events with respect to their published (NEIC, Department of Energy (DOE)) source parameters. All traces start 10 sec before the theoretical onset time. Clearly seen is a scatter of +/- 1 sec for the observed onset times at GERESS. A first explanation would be that the absolute timing of the GERESS array was not stable and produced these deviations. But this conclusion could be rejected because all GERESS onset times show a constant travel time difference of 7.5 - 7.8 sec with respect to published onset times of these events at the Gräfenberg array (GRF). It is obvious that the same absolute time scatter could not occur at two different arrays. Another explanation would be a time depending travel time between NTS and the two arrays in Germany. Our preferred hypothesis is that the published coordinates or source times are not correct, either due to typing errors or due to other reasons.

LITERATURE

Blandford, R. R. and E. I. Sweetser (1973): Seismic distance-amplitude relation for short period P, P_{diff}, PP and compressional core phases for delta > 90 deg. Report, Teledyne-Geotech, SDAC-TR-73-9, Alexandria, VA.

Schweitzer, J. (1991). Nuclear tests observed with the GERESS array in 1990, in *Advanced Waveform Research Methods for GERESS Recordings*, DARPA Annual Report No. AFOSR-90-0189, 56-78.

FIGURE CAPTIONS

Fig. 4.1: The observed m_b (PKP)-values at GERESS plotted versus estimated yields (DSIR, W. Smith, pers. communication).

Fig. 4.2: Cumulative plot of all observed presumed explosions at the Tuamotu Archipelago in 1990 and 1991. Shown are the unfiltered GERESS beams. The upper trace shows the time window for the not observed explosion on Jul 05, 1991. The seismograms are sorted by their presumed yields respectively (DSIR).

Fig. 4.3: As Fig. 4.2, but now for Butterworth bandpass (0.5 Hz - 2.5 Hz) filtered beams.

Fig. 4.4: Cumulative plot of all observed presumed explosions at NTS in 1990 and 1991. Shown are the unfiltered GERESS beams. The seismograms are sorted by their magnitudes (m_b, NEIC) respectively.

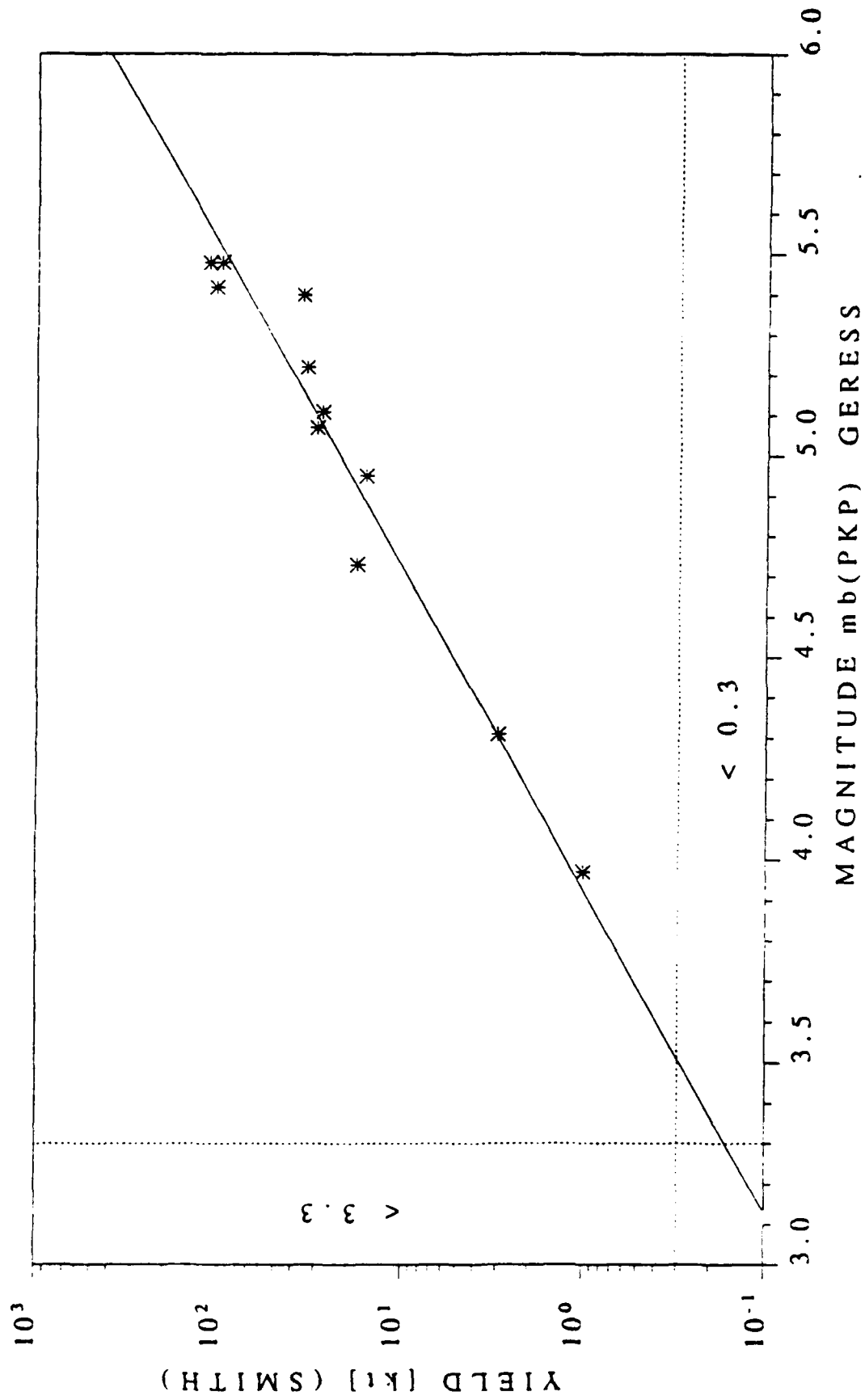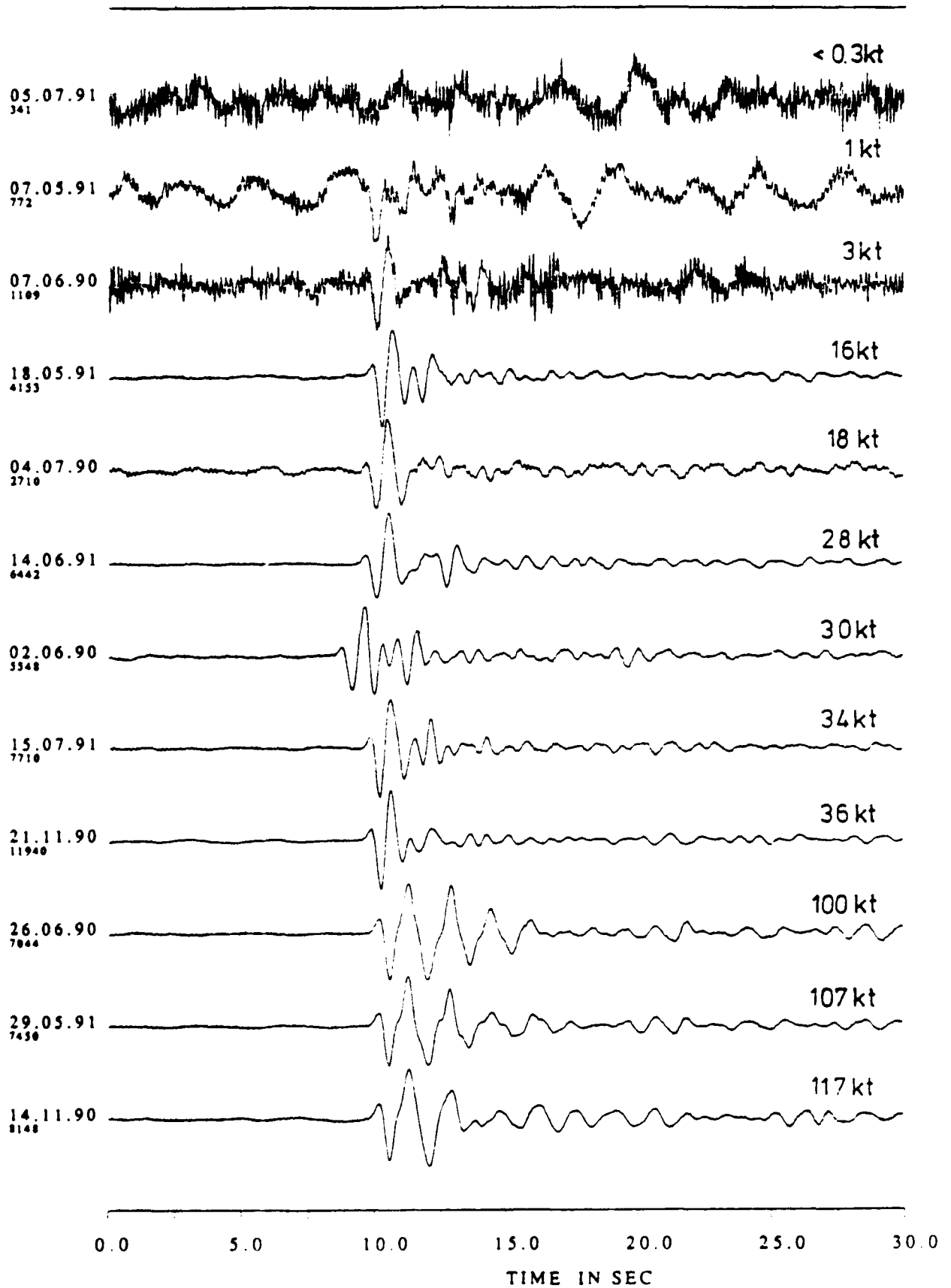Fig. 4.5: As Fig. 4.4, but now for Butterworth bandpass (0.5 Hz - 2.5 Hz) filtered beams.
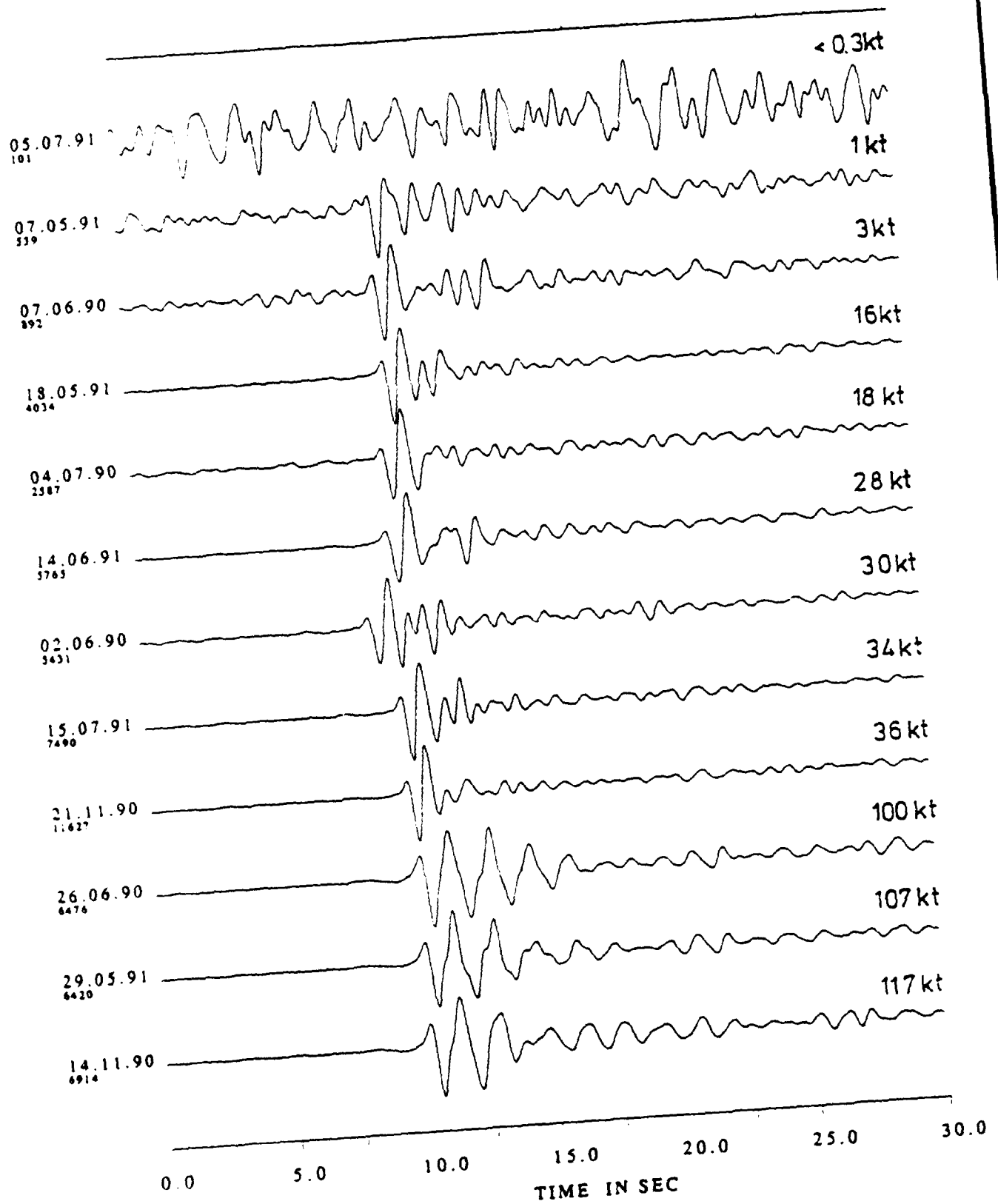
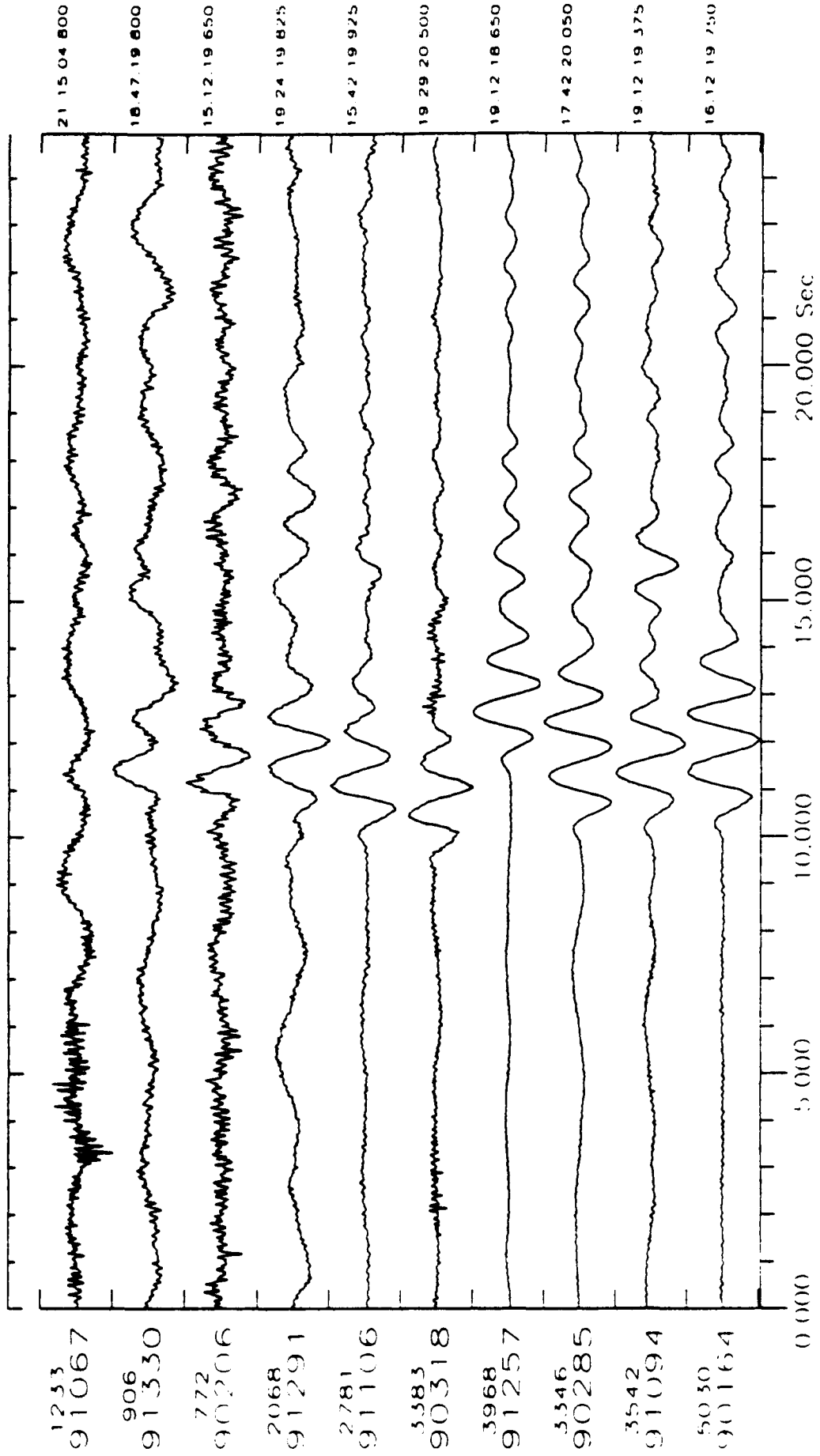Figure 4-1
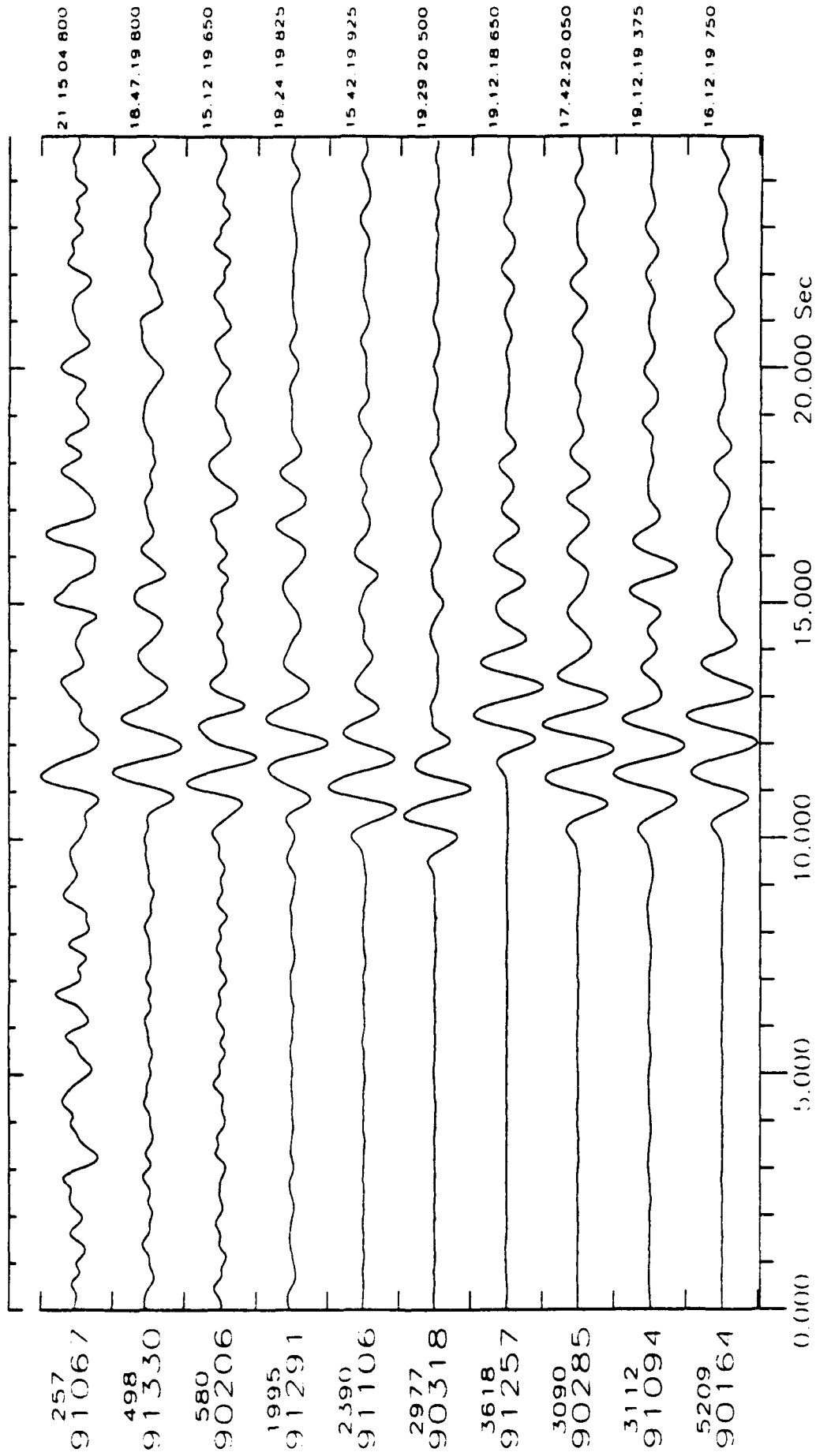
Figure 4-2

Figure 4-3

Figure 4-4

Figure 4-5

5. CHARACTERISTICS OF REGIONAL PHASES RECORDED AT GERESS

Nicolai Gestermann

5.1 INTRODUCTION

Since the GERESS array became fully operational in January 1991, numerous events at regional distances have been recorded, which will be used in this study. The configuration of the array is most favorable for the investigation of events in the local and regional distance range. In the first part some theoretical investigations are presented with the aim to improve the understanding of apparent velocity and azimuth values calculated with the frequency-wavenumber analysis for regional phases. It is shown that a full waveform analysis reveals details in the seismograms which are difficult to identify otherwise. A beam-amplitude trace was developed, to improve the signal-to-noise ratio and to automate the phase identification process.

In a second step, events recorded by GERESS at regional distances are analyzed, using the beam-amplitude trace. The main attributes of seismograms from different directions will be specified and an attempt is made to correlate these attributes with geological properties known from other studies. It will be shown that L_g and S_n are the most sensitive phases to characterize the different propagation paths.

5.2 DATA ANALYSIS

To identify the wave-types crossing the array, the broad band frequency wavenumber analysis (Nawab et al. 1985) was applied to a moving time window of 1.5 seconds duration and an increment of 0.2 seconds covering the whole seismogram

of an event. All 25 vertical components of the array were included. The frequency range of a single f,k analysis was chosen to be 0.8-4.0 Hz which yielded the best results. For each time window, back-azimuth and velocity were determined from the maximum in the wavenumber plane. For these parameters, the beam was calculated to obtain the maximum amplitude and corresponding arrival time inside the time window under study. This results in a beam-amplitude trace with time dependent parameters. In this trace correlated phases are enhanced with respect to seismogram sections made of uncorrelated phases.

To demonstrate this procedure, the results of the analysis of event 28 (Table 5.1) are shown in Figure 5.1. The power spectra of time windows with P-energy, S-energy and noise (Figure 5.2) demonstrate that the best signal-noise ratio occurres in the selected frequency band. The quality value at the top of Figure 5.1 extends from 0.0 to 1.0 and reflects the signal coherence inside each time-window. Results from time windows with a quality less than 0.35 were omitted because they correspond to the quality value for noise. Noise thresholds were determined for each event using a window before the first onset. If the azimuth value is outside a range of ±15° around the mean value, the corresponding velocity value is omitted in the plot as well.

But for an increase in amplitude for L_g, the single seismogram has a quite uniform structure. It cannot be interpreted any further without the information about apparent velocities revealed by the moving window f,k analysis. The arrival of S-phases (S_n), for example, is not visible on the vertical-components and only hardly recognizable on the horizontal components. On the other hand the onset can be clearly identified on the beam-amplitude trace and the velocity plot, characterized by a step in velocity from about 7 km/sec down to 4.5 km/sec, which indicates a fundamental change in the type of waves crossing the array.

The clear decrease in velocity along the strong P_n wave-train from about 8.5 km/sec to 7 km/sec is remarkable. A second strong phase (P_g) is easily identified in the beam amplitude trace. The corresponding velocity values cover a range from about 6.5 km/sec to 7.5 km/sec with only slight azimuth variations. The wavetrain seems to consist of constructive superposition of several arrivals rather than being a discrete onset.

The arrival times of the observed onsets (P_n, P_g, S_n and S_g) agree very well with Jeffreys-Bullen travel time curves, which are used in the automatic GERESS on-line processing at Bochum.

Two properties could be observed for GERESS registrations:

- The azimuth values from the moving window f,k analysis result in an azimuth distribution with a clear maximum in the expected direction. The azimuth values vary within a range of ±25° around this mean value, and the deviations are not restricted to the coda of the dominant phases.
- For most of the events recorded with the GERESS array at regional distances,

the variation of azimuth values shows an apparently Gaussian distribution for a certain interval around the great circle azimuth (for example see Figure 5.3).

- Secondary lobes appear in the azimuth distribution for several events, indicating the presence of secondary sources. An example is seen in Figure 5.4, where a small secondary lobe can be identified at about 205°. So far it has not been possible to connect these observed lobes with geologic or topographic structures.

To test the hypothesis of a Gaussian Distribution, a χ^2 test was applied to the data. The azimuth range was subdivided into classes Δ_j with width of 1° and the relative frequency of these classes was calculated. The corresponding histogram of event 22 is seen in Figure 5.3. The critical values $\chi_c^2(\alpha, m)_i$ and χ_i^2 were calculated for different azimuth intervals

$$[a_{mv} - a_i, a_{mv} + a_i] \qquad i = 1, ..., 180$$

around the mean value a_{mv}. The significance level α is chosen to be 0.02 and the number of degrees of freedom m was calculated by

$$m = k_i - 2 \qquad (1)$$

with

$$k_i = \text{number of classes } \Delta_j \text{ inside}$$
$$\text{the interval } [a_{mv} - a_i, a_{mv} + a_i].$$

The value f_i

$$f_i = \frac{\chi_c^2(\alpha, m)_i - \chi_i^2}{\chi_c^2(\alpha, m)_i} \qquad i = 1, ..., 180 \qquad (2)$$

$$max(f_i) = f_{max} \qquad (3)$$

was maximized, adjusting the interval width $2a_i$. If f_{max} is negative, the hypothesis of a Gaussian distribution will be rejected for the chosen significance level α. The mean value a_{mv} and azimuth values $a_{mv} \pm a_i$ ($i = 18$), indicated by dashed lines for f_{max}, is seen in Figure 5.3 for event 22. The hypothesis of Gaussian distribution was accepted in this case with standard deviation $s_a = 6.0°$.

5.3 VELOCITY ANALYSIS FOR SYNTHETIC SEISMOGRAMS

The moving window frequency wavenumber analysis was applied to synthetic seismograms to test the resolution of phase velocity determination for single phases. The seismograms were calculated with the reflectivity method (Müller 1985) for a simple model of one layer over a half-space (Table 5.2) and an explosion source at

the surface. The time dependence of the source is given by a 2nd order Küpper impulse with a dominant period of 0.3 seconds. A receiver geometry was used which corresponds to the GERESS array, disregarding differences in elevation. The epicentral distance to the key station GEC2 was chosen to be 340 km. In addition, velocity values were calculated for most of the phases with a ray tracing method as reference.

A single seismogram and the corresponding velocity values are seen in Figure 5.5. For most of the onsets, a very good agreement was found. Only some later S-phases show significant deviations; their lower signal frequency would require a change in frequency-band of the f,k analysis. The velocities of few phases with low amplitude present in the seismogram (for example at $t = 30sec$ and $t = 46sec$ in Figure 5.5) could not be calculated by the ray tracing method but are clearly identified in the velocity plot. For time windows containing more than one onset, the moving window f,k analysis yields the velocity of the phase of the highest amplitude. This will be the normal situation in real seismograms and is also the value we are usually interested in.

In a second step, genuine noise measured at GERESS was superimposed on synthetic seismograms to test its influence on the analysis (Figure 5.6). The noise amplitude was normalized to 10% of the largest phase in the seismogram. Only phases with small amplitude below the noise level disappear, otherwise the moving window analysis remains unchanged.

The described moving window analysis is an appropriate technique to identify coherent energy in the seismogram which is especially available for secondary arrivals masked by coda noise. This technique allows to determine phase velocity with sufficient accuracy when time window and frequency range are chosen appropriately. These parameters can be obtained from previously calculated power spectra.

5.4 ANALYSIS OF EVENTS FROM A MINING AREA IN POLAND AND COMPARISON WITH SYNTHETIC SIGNALS

To improve the understanding of azimuthal variations observed for regional events, 34 events from the copper mine area in Lubin (Poland) were investigated. The site is about 340 km from GERESS in an azimuth direction of 31° (event 2 in Figure 5.15). The event locations are plotted in Figure 5.7 for a small area with different symbols for the respective mine in which the event took place. A typical record for one of these events is shown in Figure 5.8. Most of the events were probably induced by mining activities (Gibowicz et al., 1977; Gibowicz, 1985). The hypocenters of the events are very well known from observations with seismic

stations inside the mining area and supposed to be exact within 10 to 100 m (500 m for only a few events) in horizontal direction and within 200 m in depth (P. Wiejacz, pers. communication).

The events were used to test the hypothesis, that the standard deviation of azimuth variations s_a as described in chapter 5.2 depends on the energy of the respective event, and to monitor its possible range. The energy of the events is measured solely on the basis of the duration of the events from near source registrations by the mining staff. These energy values and the maximum amplitude of the GERESS registration (L_g-phase of station GEC2sz) are in good agreement (Figure 5.9).

The hypothesis of a Gaussian distribution for the azimuthal variations was confirmed for 19 of 34 events with a significance level $\alpha = 0.02$ and for 4 events with $\alpha = 0.01$. For 11 events the hypothesis was not be supported, which is not surprising for 6 events taking into account the poor data quality (spikes and several data gaps). Nevertheless f_{max} was determined. As seen in Figure 5.10, the standard deviation s_a ranges from 5.0° to 9.5° and no clear interrelation between energy and s_a can be observed. The same plot was produced using signal-noise ratio instead of energy with similar results.

Theoretical azimuths and calculated mean values a_{mv} are compared in Figure 5.11. The maximum deviation is 4°, and a small general trend in northern directions (smaller azimuth values) can be observed. The agreement between theoretical azimuths and mean values a_{mv} is more stable than azimuth values from single phases derived with the f,k analysis.

Various reasons for the observed azimuth variations can be given: among others:

- coherent noise
- small scale heterogeneities along the travel path, which lead to a general deformation of the wave front.
- large scale heterogeneities like faults or topographical undulations which act as secondary sources excited by the primary seismic source as observed with the NORESS array (Gupta et al. 1990).
- energy which travels on other than great circle paths.

It is quite important to distinguish between pseudo-azimuth variations caused by wave front deformation from noise and small scale heterogeneities, and true azimuth alterations. The latter should be characterized as genuine alteration of apparent velocity.

The influence of waveform deformation to the results of the f,k analysis was investigated using simple synthetic data. Successive Küpper impulses with time dependence $w(t)$ were calculated for the GERESS array geometry simulating incoming wave fronts. A single Küpper impulse is of order 2 with frequency maximum at 2 Hz (Figure 5.12). The signal of one wave front with index k and station with

number i is given by

$$s_i(t) = a_k w(t - r_i/v_k) \qquad i = 1, ..., 25 \qquad (4)$$

with

r_i = distance between the key station and station i
a_k = amplitude of the k-th wavefront
v_k = apparent velocity of the k-th wavefront

The time dependence of K successive incoming wavefronts at station i is given by

$$s_i(t) = \sum_{k=1}^{K} a_k w(t - r_i/v_k - t_k) \qquad i = 1, ..., 25 \qquad (5)$$

with

$$t_k = \frac{(k-1)}{K} 70 sec$$

The amplitude term a_k decrease linear from 1000 to 200 counts and the velocity v_k decrease from 9 km/sec to 3 km/sec.

In a first step genuine noise, recorded with the GERESS array, was added to the synthetic signals with normalized amplitude:

$$s_i(t) = n_i(t) + \sum_{k=1}^{K} a_k w(t - r_i/v_k - t_k) \qquad i = 1, ..., 25 \qquad (6)$$

$n_i(t)$ = noise signal at station i

The noise amplitude was chosen from 10% to 100% of the maximum signal amplitude. A second test was conducted with the same synthetic signals, adding random time delays τ_r to the onset time of each single Küpper impulse and station to simulate deformed wave fronts:

$$s_i(t) = \sum_{k=1}^{K} a_k w(t - r_i/v_k - t_k + \tau_r) \qquad i = 1, ..., 25 \qquad (7)$$

The time delays were normally distributed random variables with standard deviation s_d and zero mean. The standard deviation s_d was chosen between $0.01 sec$ and $0.1 sec$. A single synthetic signal for one station is seen in Figure 5.13 for the different noise amplitudes and s_d values. The moving window f,k analysis was applied to the synthetic data and the standard deviation s_a was calculated to characterize the corresponding azimuth alterations.

The f,k analysis of the undisturbed synthetic data agrees very well with the theoretical values with maximum deviations of about 0.2 km/sec in velocity and about 0.1° in azimuth (Figure 5.14). The results for the disturbed data are shown in Table 5.3 and 5.4, which contain the calculated standard deviations s_a of the azimuth variations.

The influence of noise on the azimuth values is quite small for these perfectly coherent signals and cannot explain the observations. The error in velocity is smaller than ±0.5 km/sec for a noise level of 50%. The results for the synthetic signals with simulated wave front deformation show larger variations in azimuth and exceed the lower limit of observations (s_a = 5.8° for s_d = 0.1sec), but the error in the corresponding velocity seems to be unrealistically high in this case (±2 km/sec) and the quality is lower than that from noise windows. The superposition of noise (50%) to the synthetic signals with s_d = 0.05sec only leads to a small increase of s_a from 2.34° to 2.62° (Table 5.3).

Thus it has been shown, that there is no dependence between the signal energy and the observed azimuth variations. Superposition of noise and wave front deformation alone cannot explain the observations, such that that waves with a true deviation from great- circle azimuth must be assumed to be present in the seismograms, especially in the coda.

5.5 CHARACTERISTIC OF GERESS RECORDINGS

The area around GERESS was divided into 6 sectors (Figure 5.15) to separate events from different azimuth directions. Sectors without recorded seismicity were omitted. If more than one event occurred in the same location, the one, which characterizes these events best, was selected for this study. The investigation was restricted to distances less than 800 km because there are no events with greater distance from northern directions which can be compared with events from the south. The location were taken from the *Preliminary Determination of Epicenter* (PDE) *Bulletin* from the National Earthquake Information Service (NEIS) if no better information was available. The beam-amplitude trace was used for this investigation, because it contains information of the events in the most condensed form. The data were shifted to the first onset and each event was normalized to the maximum amplitude.

The beam-amplitude traces of events from sector I are shown in Figure 5.16. Most of the events from this area are induced by mining activities at the Lubin copper basin (see also chapter 5.4) and the coal mines in the Katovice area, or were generated by quarry blasts. P_j and L_g are the dominant onsets in the seismograms from this sector. The P_n onset can be identified, but the S_n phase is hardly recognizable without the additional velocity information.

Events with epicentral distances greater than 500 km could not be observed from this direction due to the Teisseyre-Tornquist line (TTL, Figure 5.15) (Tornquist, 1911). This suture zone defines a sharp boundary between the East European Platform and the Paleozoic Europe. Investigations show that the Moho discontinuity increases from a depth of about 25 - 35 km in Central Europe to a depth of about 45 - 50 km in the Eastern European Platform. In the central section of the Teisseyre-Tornquist line (Poland) the Moho apparently reaches depths of more than 60 km (Meissner et al., 1987) in a graben-like structure, which seems to block regional seismic energy (Gestermann et al. 1991).

Sector II (Figure 5.17) to the south-east direction includes the Eastern Alps in the North, the Pannonian basin and a small part of the Southern Carpathians. The two events with epicentral distances smaller than 300 km from this sector contain a dominant L_g-wavetrain and a clear S_n onset. The events from the Hungary-Romania border region ($\Delta > 650\ km$) are quite unusual. The main feature is a large P_n onset followed by a long coda. For most of the events from this region, later arrivals (S_n and L_g) are only weak, except of event 5 with a clearly identifiable S_n. The epicenters of these events lie inside the transition zone between the Pannonian basin and the Southern Carpathians. The travel path crosses this basin, which may be the reason for the long P-coda.

For sector III, to south direction (Figure 5.18), no L_g wavetrain could be observed in the seismograms of events with $\Delta > 500\ km$ from the Adria region. At the same time, S_n is visible for epicentral distances greater than 350 km and is the dominant onset in the seismograms above 500 km. Event 13 shows quite an abnormally high S_n amplitude.

Nearly the same situation can be reported from sector IV (Figure 5.19), including event 18 and 21 at the border to sector V. This sector to the south-west direction include the Western Alps and the Po plain in the south. The L_g wavetrain is missing for events with epicentral distances greater than 500 km and a corresponding dominant S_n phase can be observed. For event 21, a clear onset after P_n can be seen which could be P^*.

The beam-amplitude traces of the events of sector V are plotted in Figure 5.20. The paths of events from this sector are oblique to the strike of the Alps and cross only the northern part. The L_g wavetrain is the dominant onset up to a distance of 560 km, but no clear S_n is visible. In the beams of sector VI (Figure 5.21) with travel paths crossing the Variscan front, the L_g wavetrain is also the dominant onset and the S_n phase is rather weak.

Absence of the L_g wavetrain for epicentral distances greater than 500 km and a corresponding S_n phase with high amplitude are the main properties of the seismograms in sector III and IV in contrast to the seismograms of sector V and VI with no visible decrease of L_g amplitudes. Unfortunately, no events with 400 $km < \Delta < 500\ km$, where the transition from L_g to S_n thought to occur, have

been recorded as yet.

For sector IV, we can associate this transition with the transition zone from the European plate to the Adria microplate (Giese et al., 1982). The travel path of events with epicentral location on the Adria microplate (event 22 and 25 in Figure 5.22) crosses this transition zone and the seismograms are characterized by a high amplitude S_n onset. The events of sector V with high L_g energy are as GERESS located on the European plate. The thinning of the crust from about 50 km in the Western Alps to about 34 km below GERESS along this path does not seem to be sufficient to disturb the L_g wavetrain.

The profile of sector III crosses the Eastern Alps, the tectonical Sava Trough and the Dinarides in the south (Horvath and Berckhemer, 1982). The events with epicenter in the Dinarides beyond the elongated depression of the Sava Trough (event 13, 14, 15, and 16) are characterized by S_n with high amplitudes in contrast to events at smaller distances.

Other investigations (e. g. Bouchon, 1982) show that L_g waves are guided waves made up of $SH-$ and $SV-$waves incident on the Moho at angles more grazing than the critical incidence and multiple reflected within the crust. Leaking of energy into the mantle starts taking place, when irregularities inside the crust disturb the waveguide and changing angle of incidence. This can explain the observation, that a low amplitude L_g phase corresponds to a high amplitude S_n phase which travels in the upper mantle. The hypothesis of energy conversion from L_g to S_n is in good agreement with results of theoretical investigations (Kennett, 1986; Kennett 1989) for a crustal waveguide thinning and two-dimensional heterogeneous crustal structures. The amount of conversion observed in this study is however quite surprising, especially for the seismograms in sector III.

A comparison of apparent velocities, calculated with the moving- window f,k-analysis for event 28 of sector VI (L_g as the dominant onset) and event 25 of sector IV with hardly visible L_g but a S_n onset with high amplitude is shown in Figure 5.23. Differences are not striking and do not correspond to the differences in the seismograms. The onset of S_n is observed very well in both velocity plots, but the following trend is much clearer for event 32 with a slow decrease towards the weak L_g wavetrain. The apparent velocities of $P-$phases are significantly higher for event 32 with velocities greater than 7 km/sec correspond to 6 km/sec for event 28. The clear decrease in velocity following the P_n onset for event 28 cannot be observed for event 32.

5.6 CONCLUSIONS

It is well known from many other studies (e. g. Baumgardt, 1990) that the L_g phase is quite sensitive to changes in crustal properties. This fact can be used to map crustal heterogeneities as done e. g. by Kennett et al. (1985). The observation of possible conversion from L_g- to S_n-type energy is in good agreement with the existence of the Periadriatic line, which separates the European plate from the Adriatic microplate. This investigation should be continued when more events from this region become available. A detailed map of the crustal heterogeneities and tectonic zones will be derived. The use of the beam-amplitude trace is especially suited for small events, which could thus be included to improve the coverage of the investigated distance and azimuth range.

REFERENCES

Baumgardt, D. R. (1990). Investigation of teleseismic L_g blockage and scattering using regional arrays. Bull. Seis. Soc. Am., 80, Part B, 2261-2281.

Bouchon, M., (1982). The complete synthesis of seismic crustal phases at regional distances. J. Geophys. Res., 87, 1735-1741.

Gestermann, N., M. L. Jost, and J. Schweitzer (1991). Performance of the new German Experimental Regional Seismic System (GERESS) during GSETT-2 (Abstract), EOS, Trans. Am. Geoph. Union, 72, Suppl. Oct. 29, 1991, 354.

Gibowicz, S. J., A. Bober, A. Cichowicz, Z. Droste, Z. Dychtowicz, J. Hordejuk, M. Kazimierczyk and A. Kijko (1979). Source study of the Lubin, Poland, tremor of 24 March 1977. Acta Geoph. Pol., 27, 3-38.

Gibowicz, S. J. (1985). Seismic moment and seismic energy of mining tremors in the Lubin copper basin in Poland. Acta Geoph. Pol., 33, 243-257.

Giese, P., K.-J. Reutter, and R. Nicolich (1982). Explosion seismic crustal studies in the alpine mediterranean region and their implications to tectonic processes, in Alpine-Mediterranean Geodynamics, Geodynamics Series Volume 7, edited by H. Berckhemer, and K. Hsü, 39-73, American Geophysical Union, Boulder.

Gupta, I. N., C. S. Lynnes, T. W. McElfresh, and R. A. Wagner (1990). F-k analysis of NORESS array and single station data to identify sources of near-receiver and near-source scattering. Bull. Seism. Soc. Am., 80, Part B, 2227-2241.

Harjes, H.-P. (1990). Design and siting of a new regional array in Central Europe. Bull. Seism. Soc. Am., 80, Part B, 1801-1817.

Horvath, F. and H. Berckhemer (1982). Mediterranean backarc basins, in Alpine-Mediterranean Geodynamics, Geodynamics Series Volume 7, edited by H. Berckhemer, and K. Hsü, 39-73. American Geophysical Union, Boulder.

Kennett, B. L. N., S. Gregersen, S. Mykkeltveit and R. Newmark (1985). Mapping of crustal heterogeneity in the North Sea basin via the propagation of L_g-waves. Geophys. J. R. astr. Soc., 83, 299-306.

Kennett, B. L. N. (1986). L_g-waves and structural boundaries. Bull. Seism. Soc. Am., 76, 1133-1141.

Kennett, B. L. N. (1989). L_g-wave propagation in heterogeneous media. Bull. Seism. Soc. Am., 79, 860-872.

Meissner, R., T. Wever, and E. R. Flüh (1987). The Moho in Europe - Implications for crustal development, Ann. Geophys., 5B, (4), 357-364.

Müller, G. (1985). The Reflectivity Method: A Tutorial. J. Geophys., 58, 153-179.

Nawab, S. H., F. U. Dowla and R. T. Lacoss (1985). Direction determination of wideband signals. IEEE Trans on Acoustics, Speech and Signal Processing, ASSP-33(4),1114-1122.

Tornquist, A. (1911). Die Tektonik des tieferen Untergrundes Norddeutschlands, Sitzungsberichte der königlich preussischen Akademie der Wissenschaften. 38, 27.7.1911, 822-836.

FIGURE CAPTIONS

Figure 5.1: Results of the moving-window f,k analysis of event 28. The length of the dashes correspond to the time length of the f,k analysis.

Figure 5.2: Velocity power spectra density for time windows containing P- and S-energy, and for a time window with noise before the first onset.

Figure 5.3: Histogram of the azimuth distribution for event 22 and the best fitting Gaussian distribution ($s_d = 6.0°$, $a_{mv} = 210.6°$).

Figure 5.4: Histogram of the azimuth distribution for event 12 with main- and secondary lobe and the best fitting Gaussian distribution ($s_d = 7.0°$, $a_{mv} = 173.3°$).

Figure 5.5: Apparent velocity values determined for the synthetic seismograms calculated for the model of Table 5.2. The values indicated by dashes were calculated with the f,k analysis and circles were obtained using a ray tracing method (solid circles indicate a good agreement between the two methods).

Figure 5.6: Same as Figure 5.5 but 10% genuine noise was superimposed upon the synthetic seismograms.

Figure 5.7: Epicenter map of events that occurred in the Lubin copper basin in Poland. The different symbols distinguish between the different mines at which the event occurred.

Figure 5.8: Characteristic seismogram (station GEC2sz) of an event from the mining area in Lubin (Poland) and the corresponding apparent velocity values from the moving-window f,k analysis.

Figure 5.9: Comparison between the energy of events from Figure 5.7 measured with near source observations on the basis of the duration and the maximum amplitude of the GERESS registration (station GEC2sz).

Figure 5.10: Relation between the standard deviation of azimuth variations s_a and the energy of events from the mining area in Lubin (Poland).

event	date	origin time	latitude °N	longitude °E	depth (km)	M_L	region
1	30.11.91	11:29:47.1	50.367	14.665		2.3	Czechoslovakia
2	09.09.91	18:36:57.0	51.414	16.220	1	3.2	Poland
3	10.01.91	06:05:43.0	50.278	18.952	10	3.2	Poland
4	02.05.91	23:19:47.4	47.930	16.352	10	2.1	Austria
5	21.10.91	02:09:47.6	48.240	17.442	10	2.6	Czechoslovakia
6	21.11.91	02:16:29.8	45.424	21.061	10	2.5	Romania
7	28.10.91	00:21:30.3	44.332	21.378	9	2.7	Yugoslavia
8	01.06.90	20:21:27.3	47.877	14.248	8	3.4	Austria
9	07.02.91	07:12:48.1	47.590	15.503	10	3.0	Austria
10	27.04.91	18:44:53.3	46.585	15.190	10	4.0	Yugoslavia
11	04.04.91	20:43:08.7	45.728	14.883	10	3.0	Yugoslavia
12	21.02.92	20:50:30.1	45.484	14.530		2.9	Yugoslavia
13	28.08.91	00:03:35.4	44.396	15.366	10	3.5	Yugoslavia
14	27.11.90	04:37:58.5	43.853	16.633	24	5.6	Yugoslavia
15	26.04.91	22:35:11.3	43.446	16.244	12	3.8	Yugoslavia
16	31.07.90	23:15:16.2	43.016	17.807	10	4.4	Yugoslavia
17	30.11.90	15:44:00.0	47.455	12.692		2.0	Austria
18	25.04.91	20:05:32.7	47.487	10.976	10	3.4	Austria
19	30.05.91	11:50:57.1	47.738	9.610	10	2.9	Germany
20	16.05.90	12.32.26.7	46.979	10.226	5	4.0	Northern Italy
21	20.11.91	01:54:16.9	46.770	9.532	10	5.3	Switzerland
22	31.10.91	09:31:16.1	45.031	10.054	10	4.6	Northern Italy
23	14.05.90	21:42:32.6	48.049	6.714	10	3.1	France
24	03.06.90	19:23:55.0	46.304	7.281	10	3.0	Switzerland
25	29.05.91	20:24:40.4	45.016	8.213	10	3.8	Northern Italy
26	24.03.91	05:05:06.2	50.314	12.202	10	2.5	Vogtland
27	29.05.90	06:14:26.7	50.142	8.513	32	3.3	Germany
28	16.05.91	02:06:16.7	52.309	7.649	10	4.4	Germany

Table 5.1 List of events used in this study.
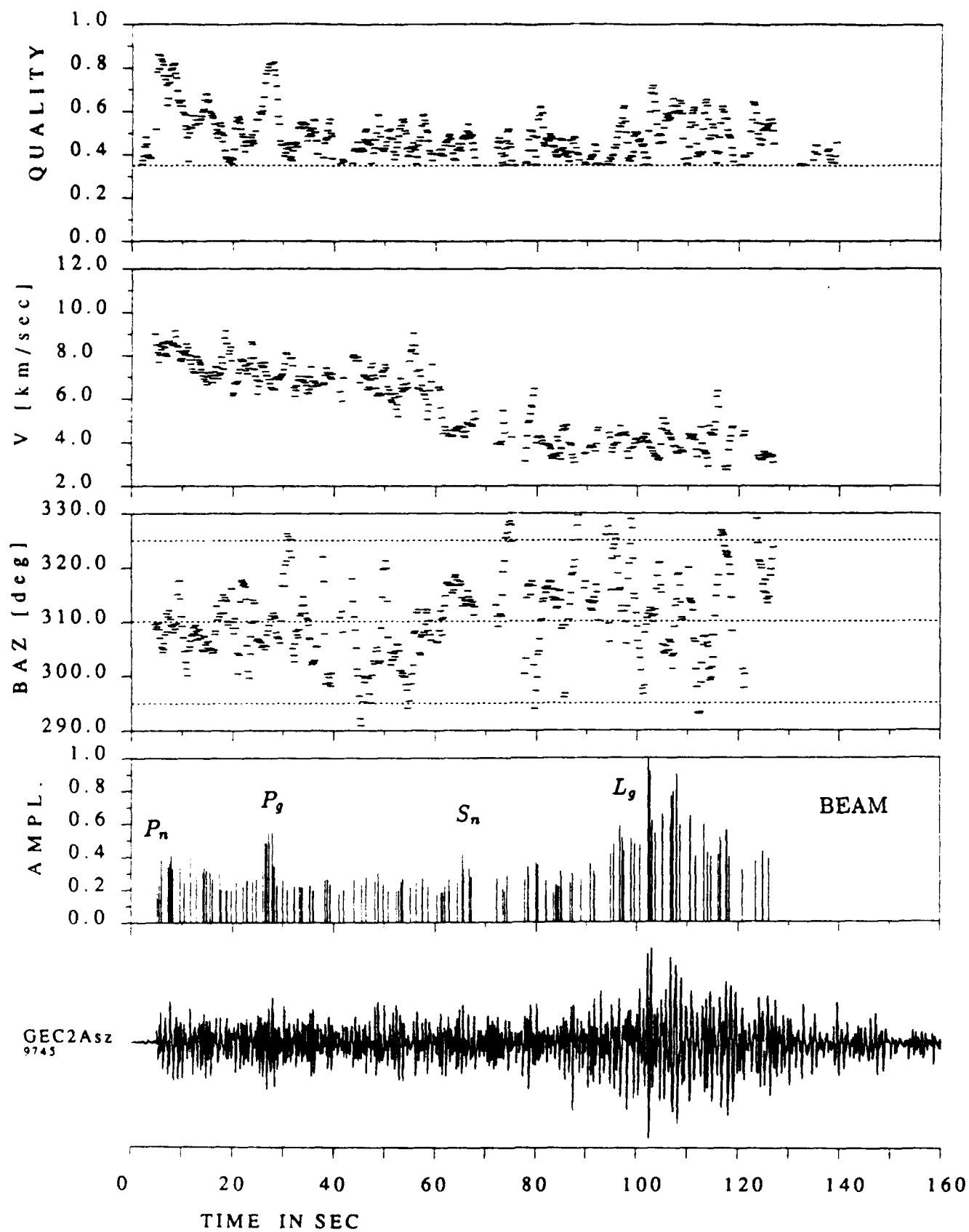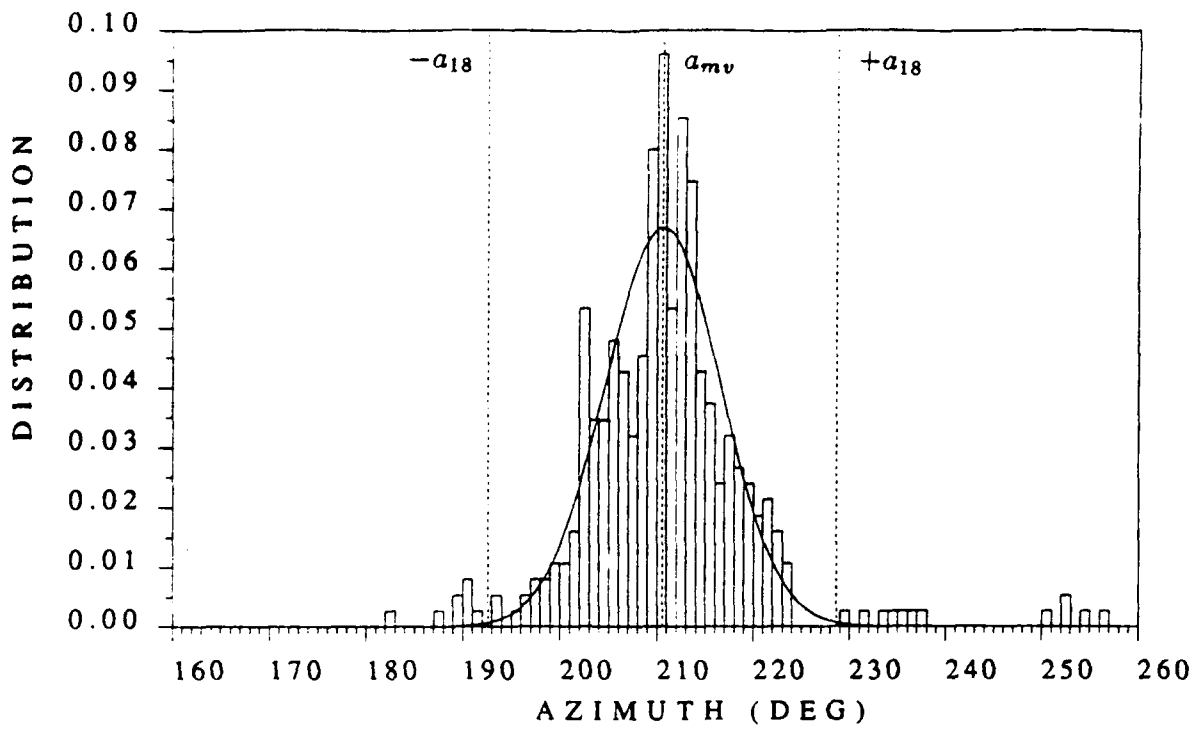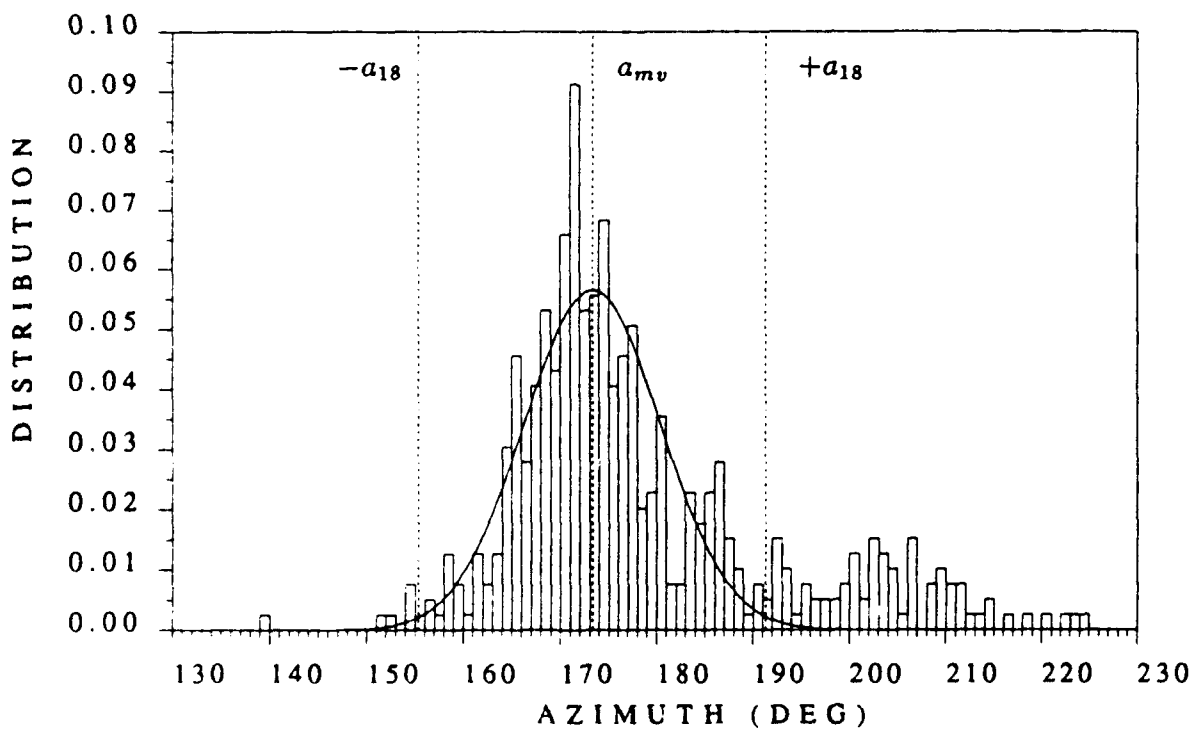
Figure 5.1
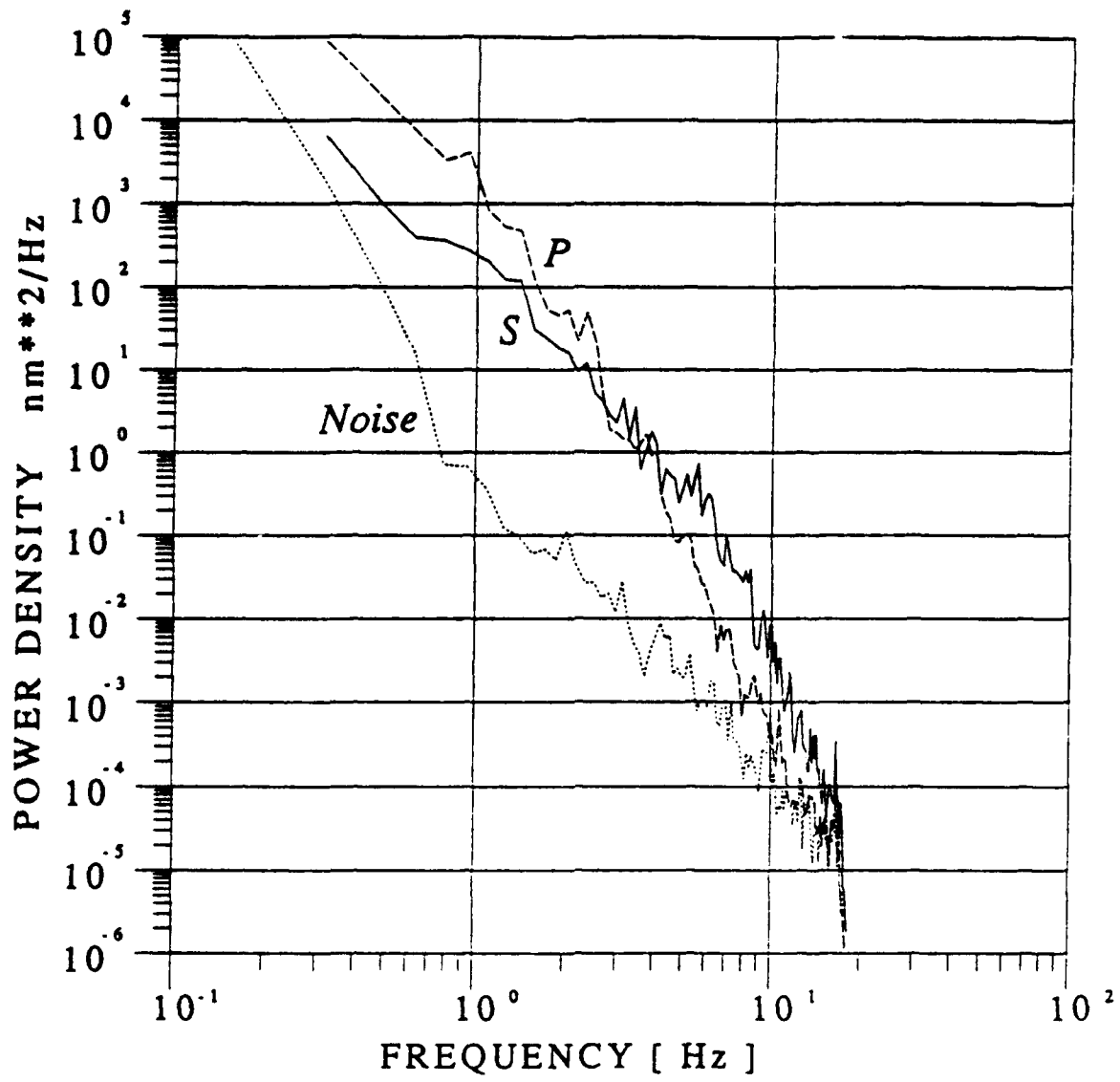
Figure 5.2

Figure 5.3

Figure 5.4

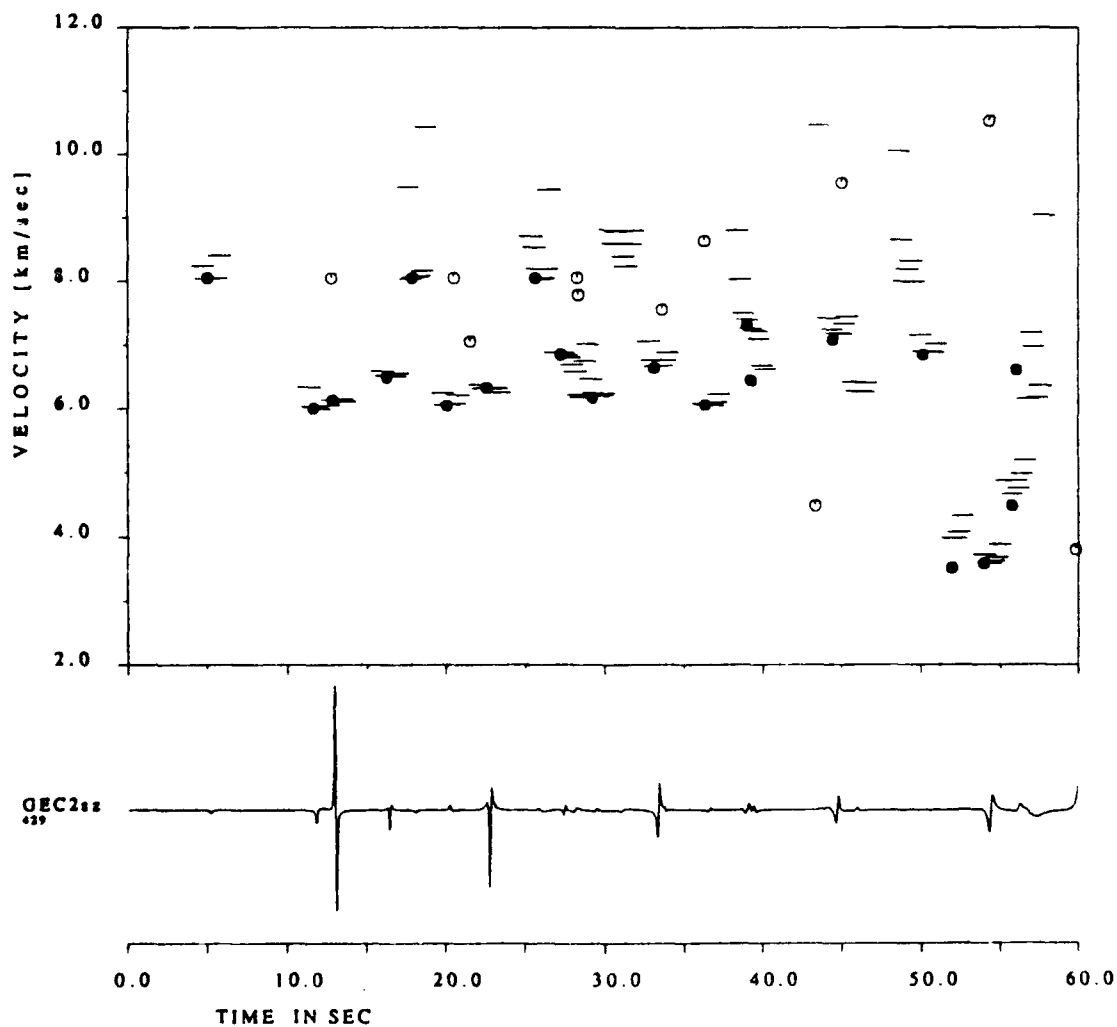| V_p (km/sec)	V_s (km/sec)	ϱ (g/cm^3)	z (km)
6.00	3.50	2.9	35
8.04	4.47	3.2	∞

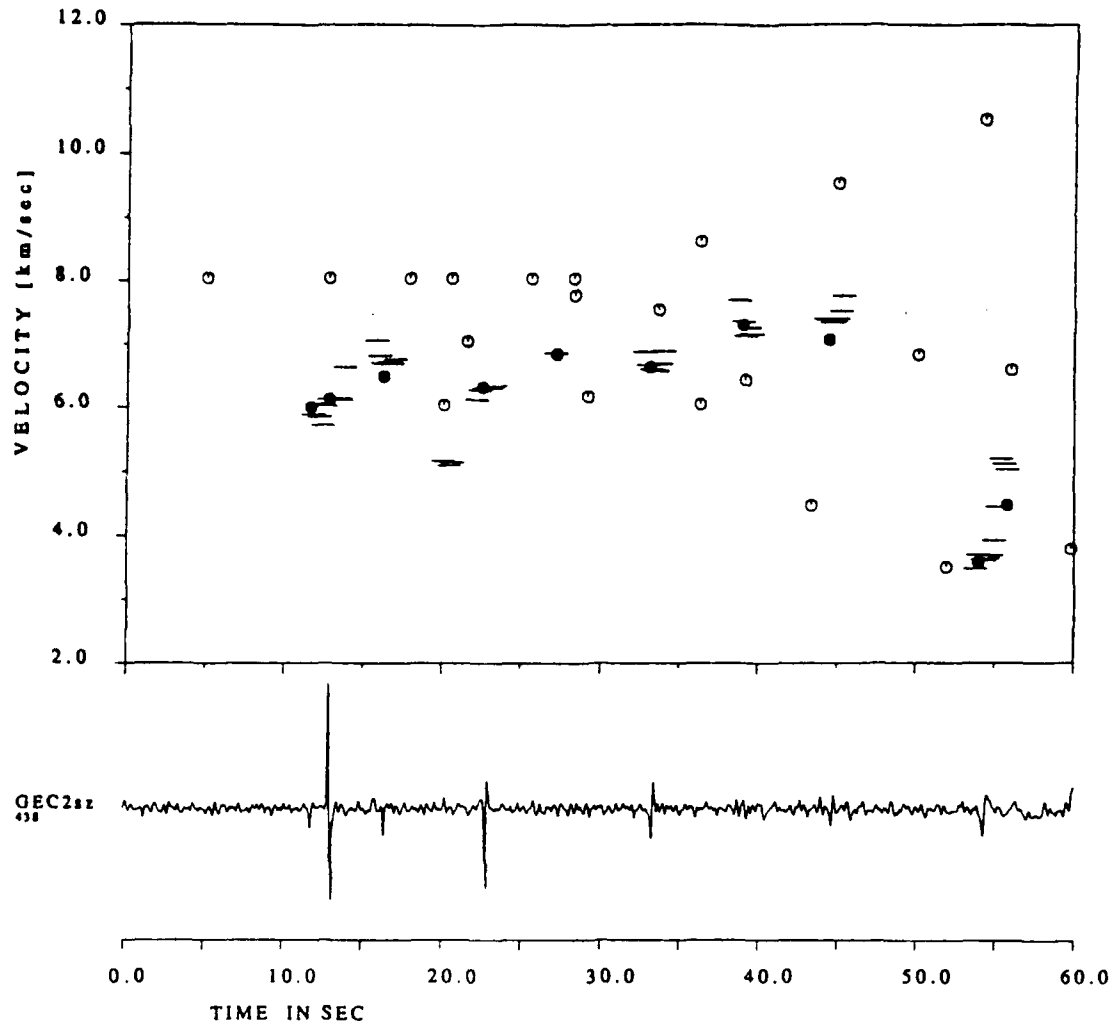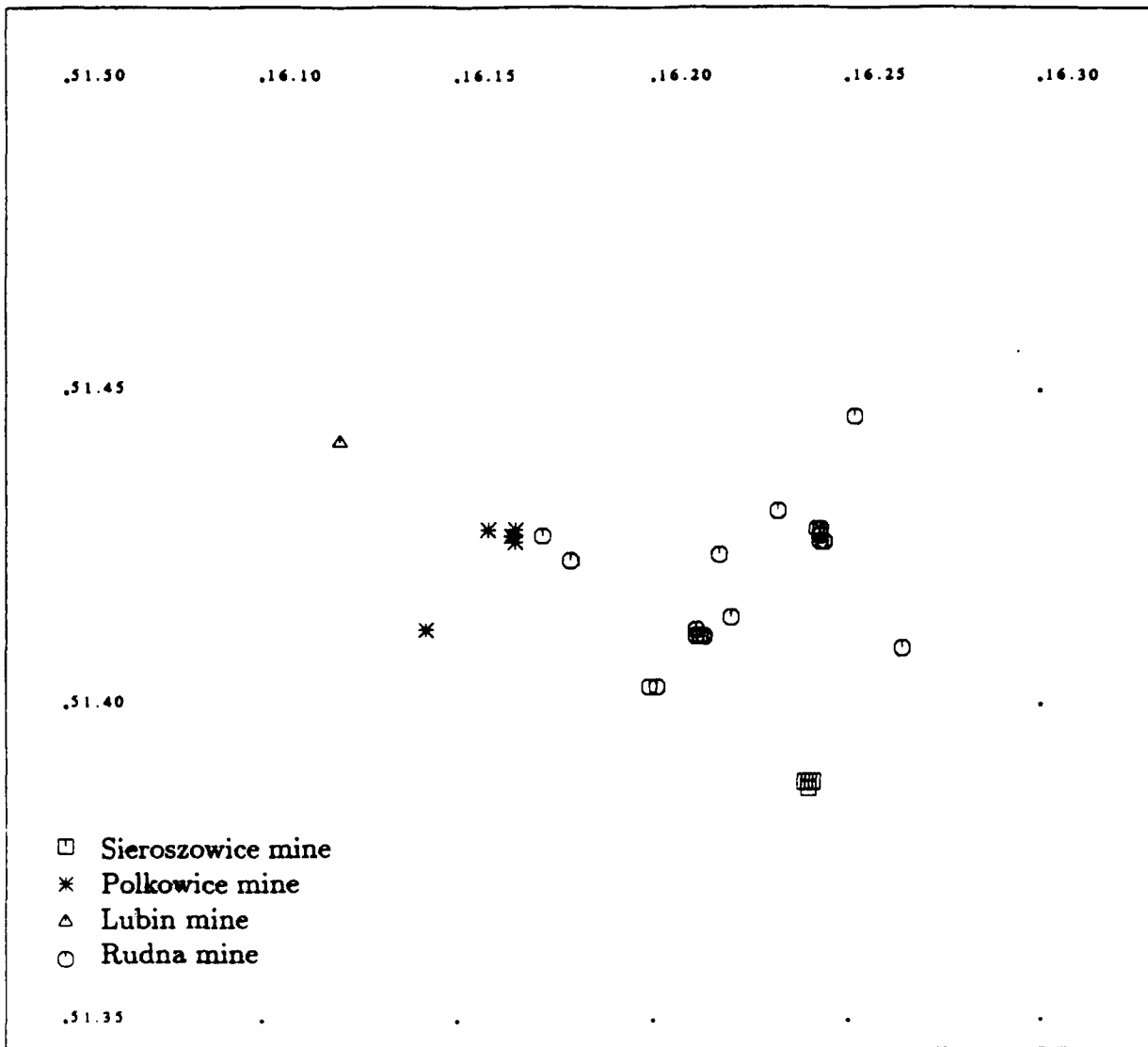Table 5.2 Parameters of the model used for the theoretical seismogram calculation.
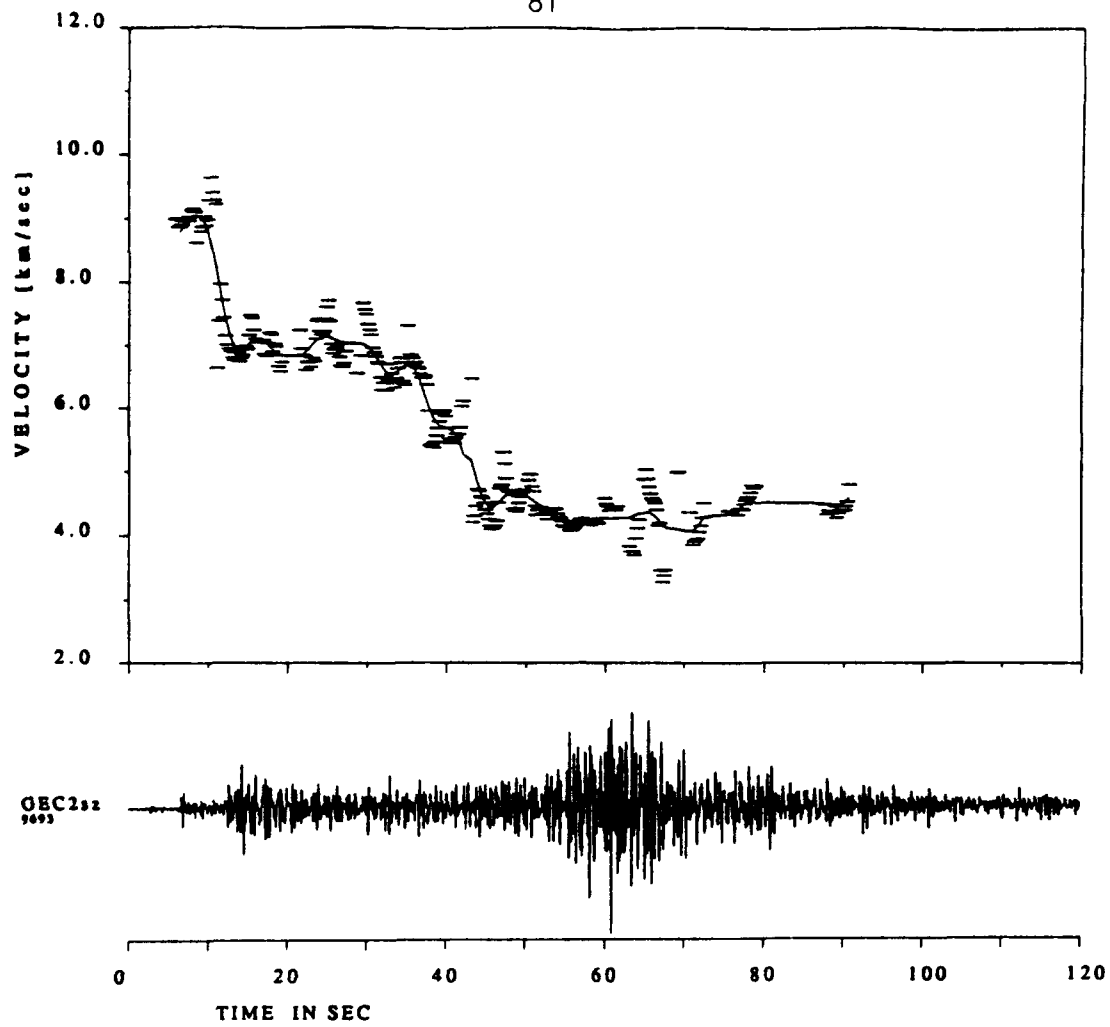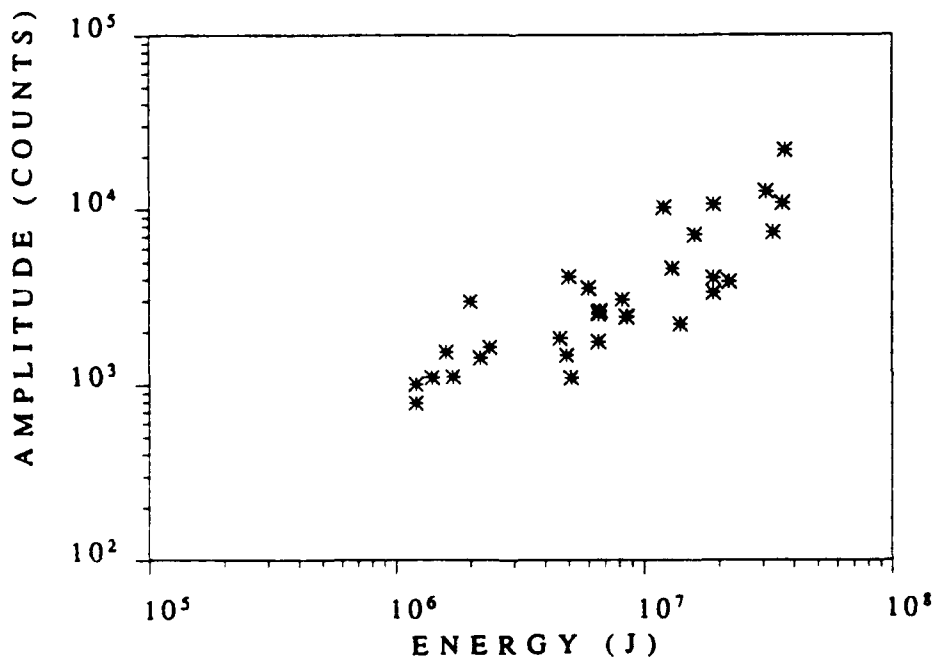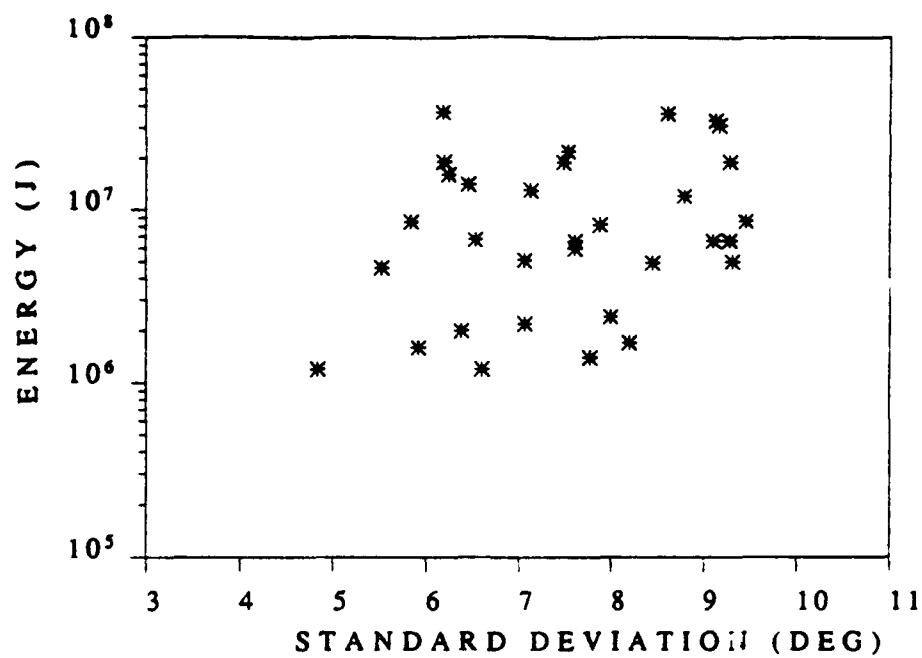

Figure 5.5

Figure 5.6

Figure 5.7

Figure 5.8

Figure 5.9

Figure 5.10

Figure 5.11

Figure 5.12

TIME IN SEC

FREQUENCY [Hz]

BEAM

TIME [sec]
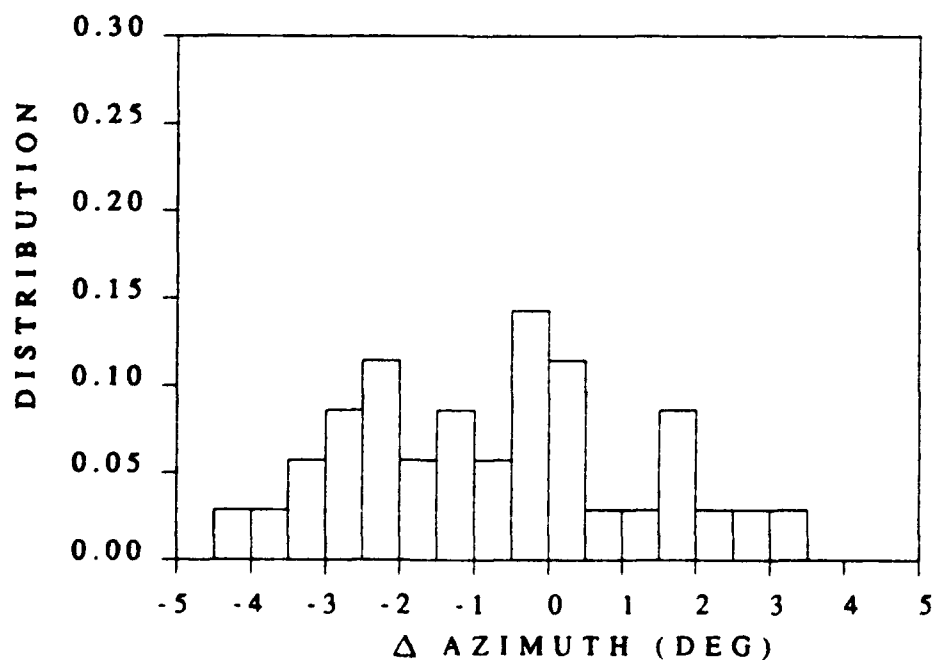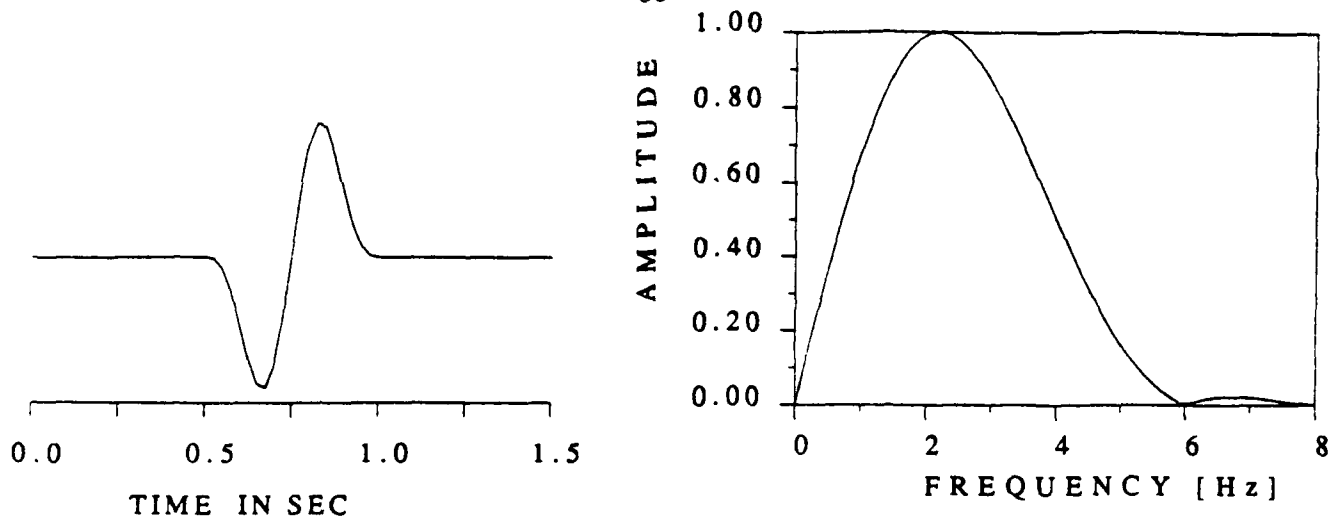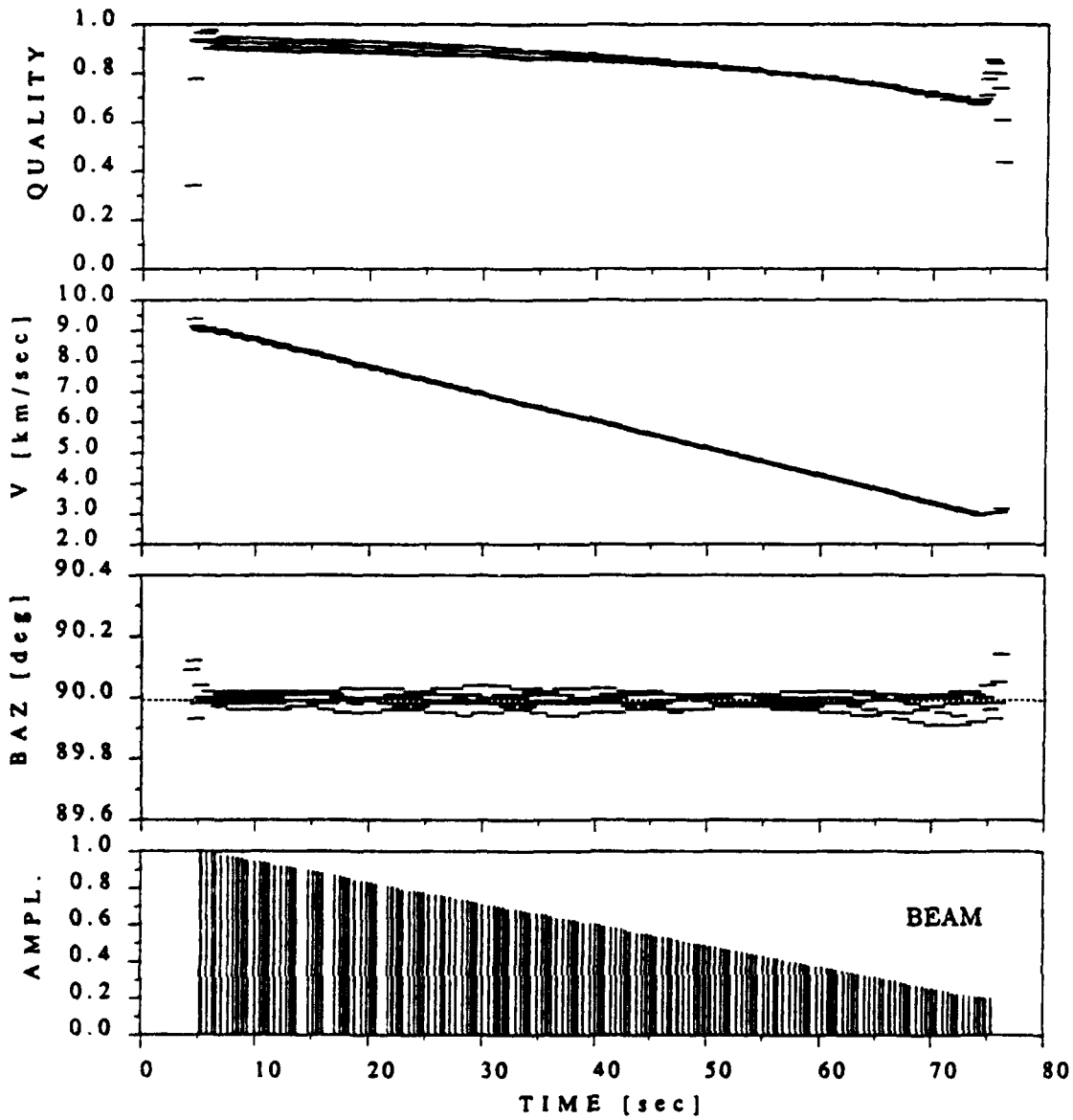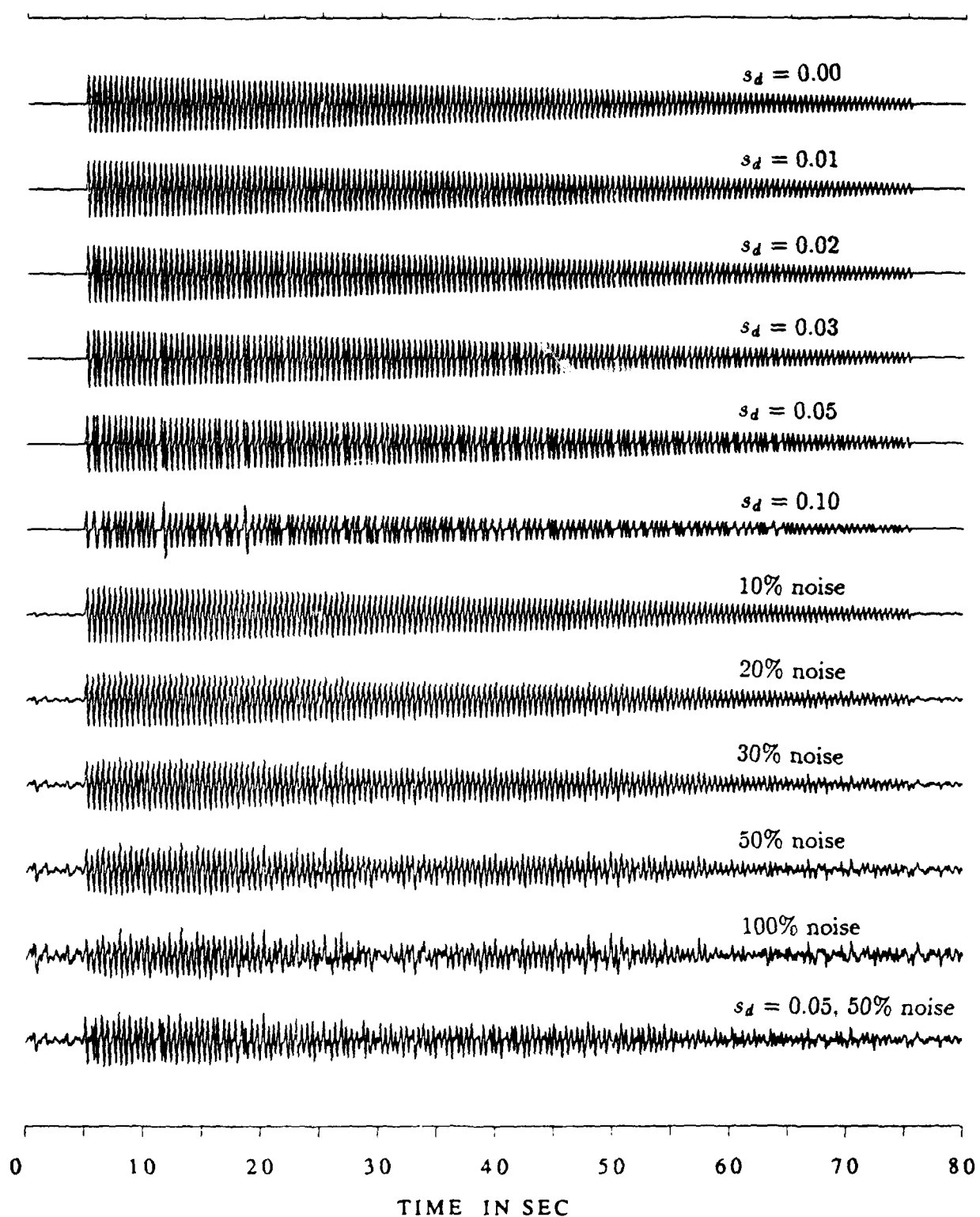
Figure 5.14

Figure 5.13

s_d in sec	noise amplitude in %	s_a in deg
0.00	-	0.03
0.01	-	0.46
0.02	-	0.93
0.03	-	1.42
0.05	-	2.34
0.05	50	2.62
0.10	-	5.82

Table 5.3 Correlation between the standard deviation s_d of random time delays with Gaussian distribution added to the synthetic signals (described in the text) and the standard deviation s_a of azimuth variations derived from the results of the moving-window f,k analysis. In one case noise (in % of the maximal signal amplitude) was added in addition.

noise amplitude in %	s_a in deg
0	0.03
10	0.16
20	0.32
30	0.49
50	0.86
100	1.94

Table 5.4 Correlation between the amplitude of noise (in % of the signal amplitude) added to the synthetic signals (described in the text) and the standard deviation s_a of azimuth variations, derived from the results of the moving window f-k analysis.

Figure 5.15

Figure 5.16

Figure 5.17
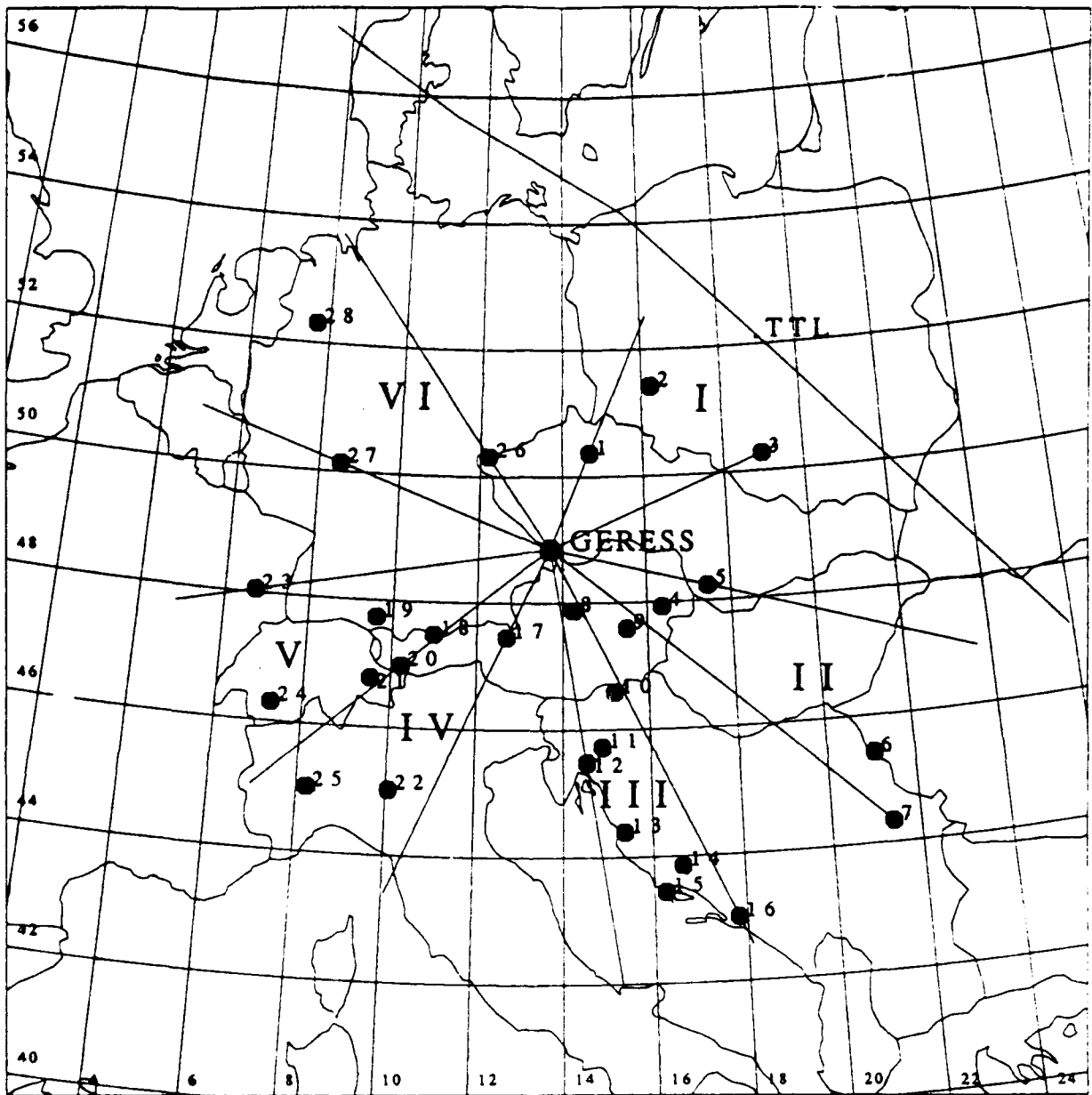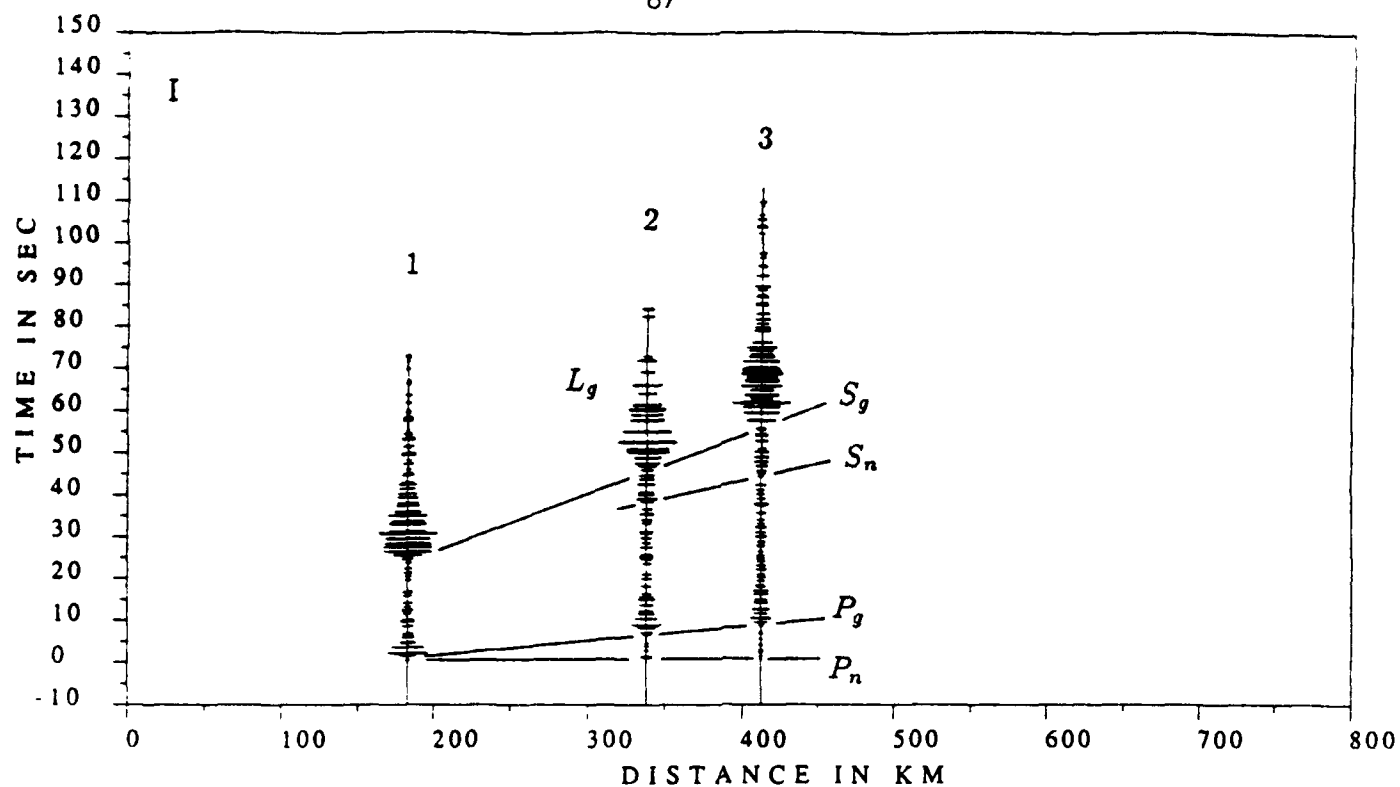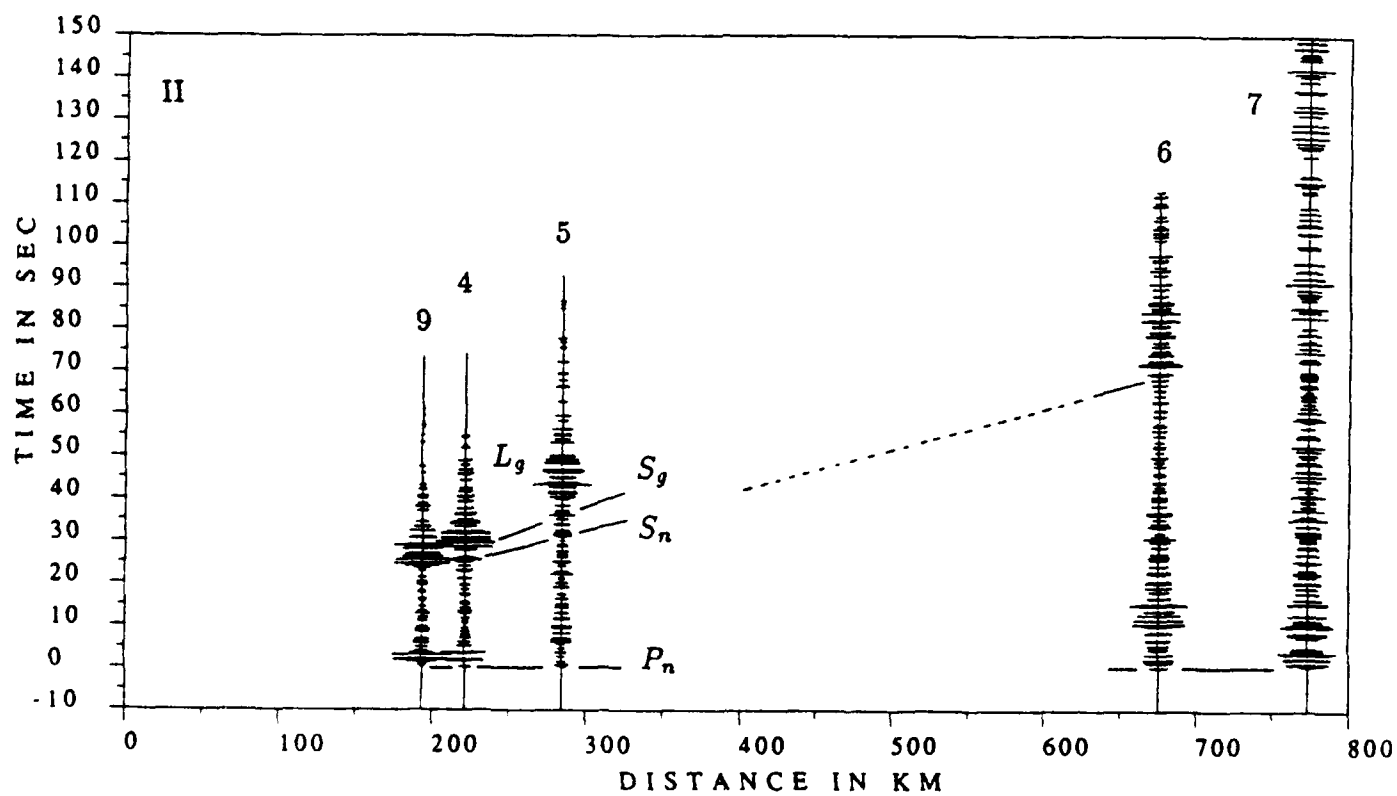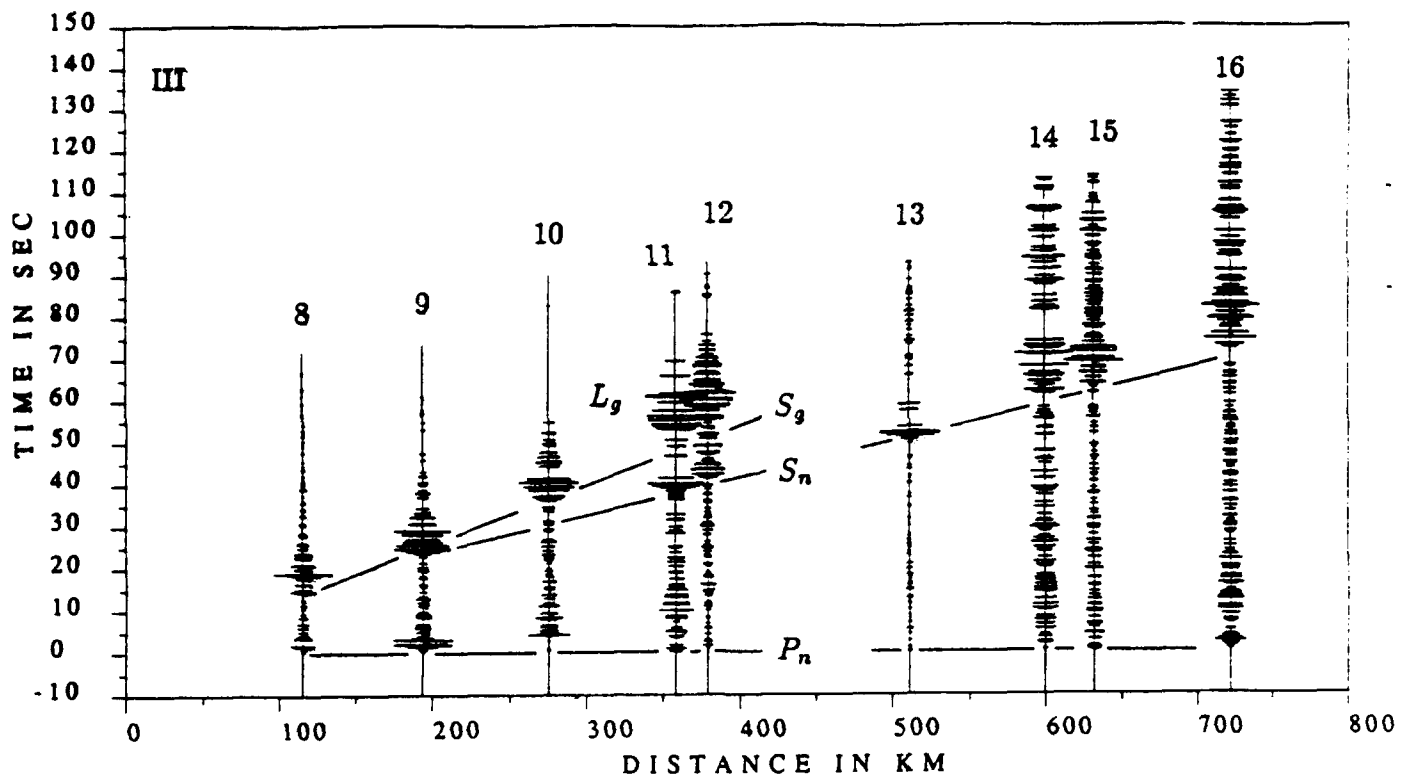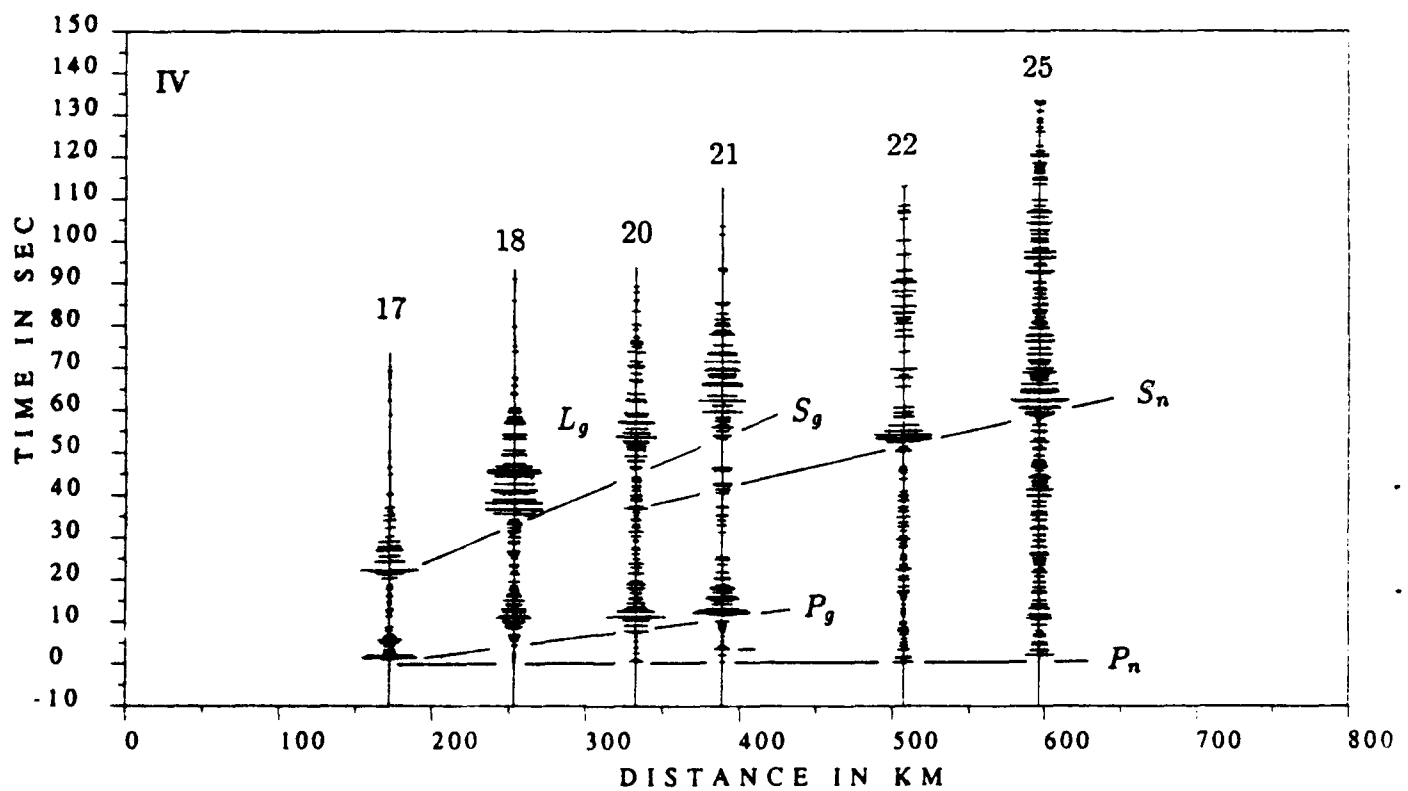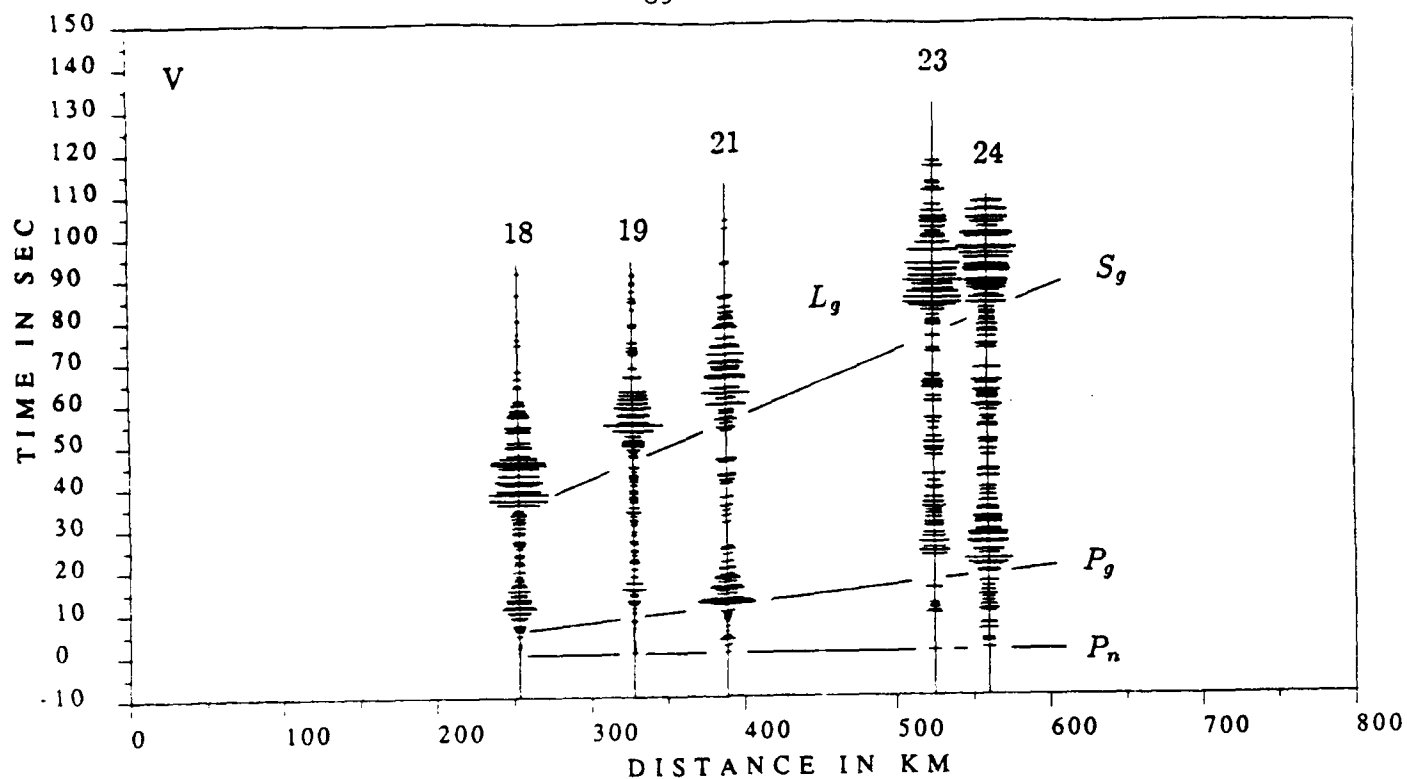
88

Figure 5.18

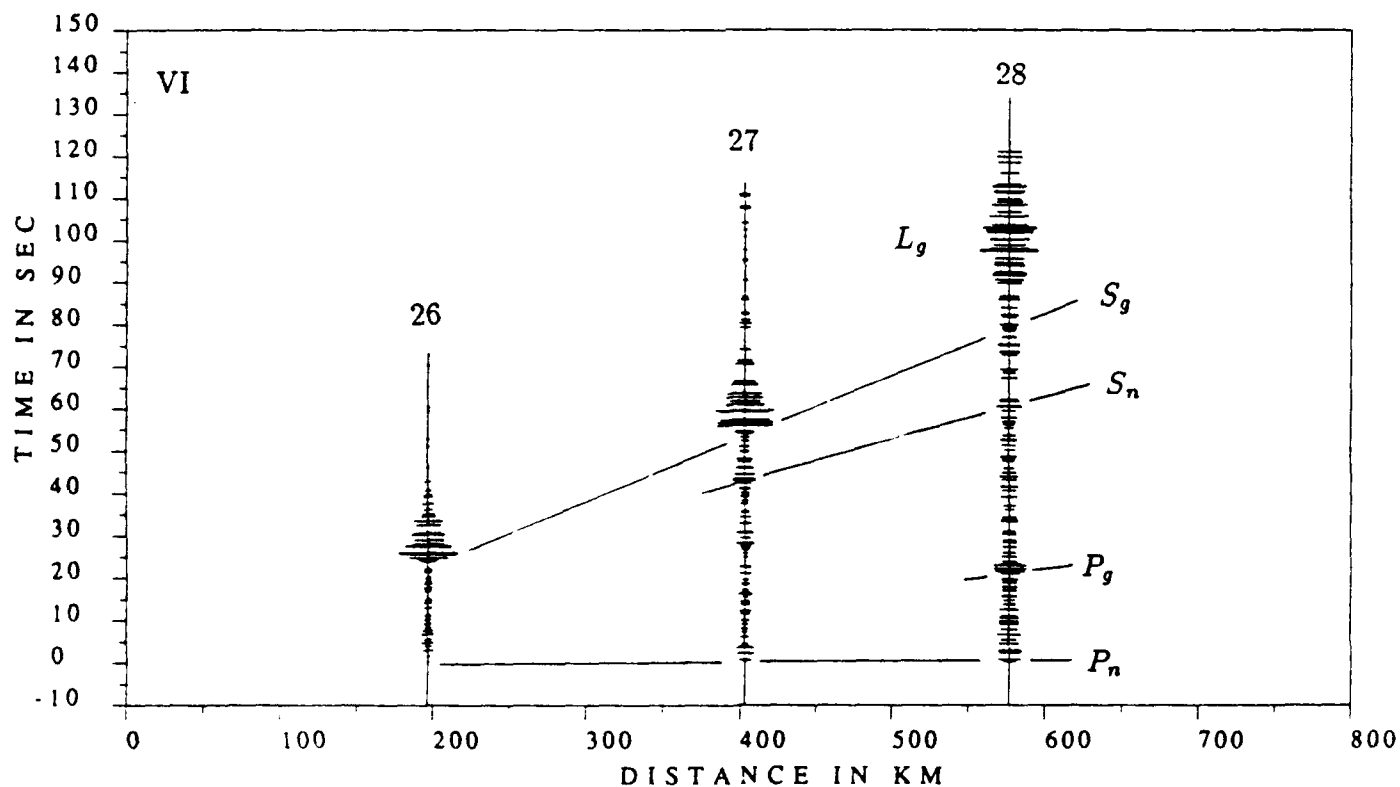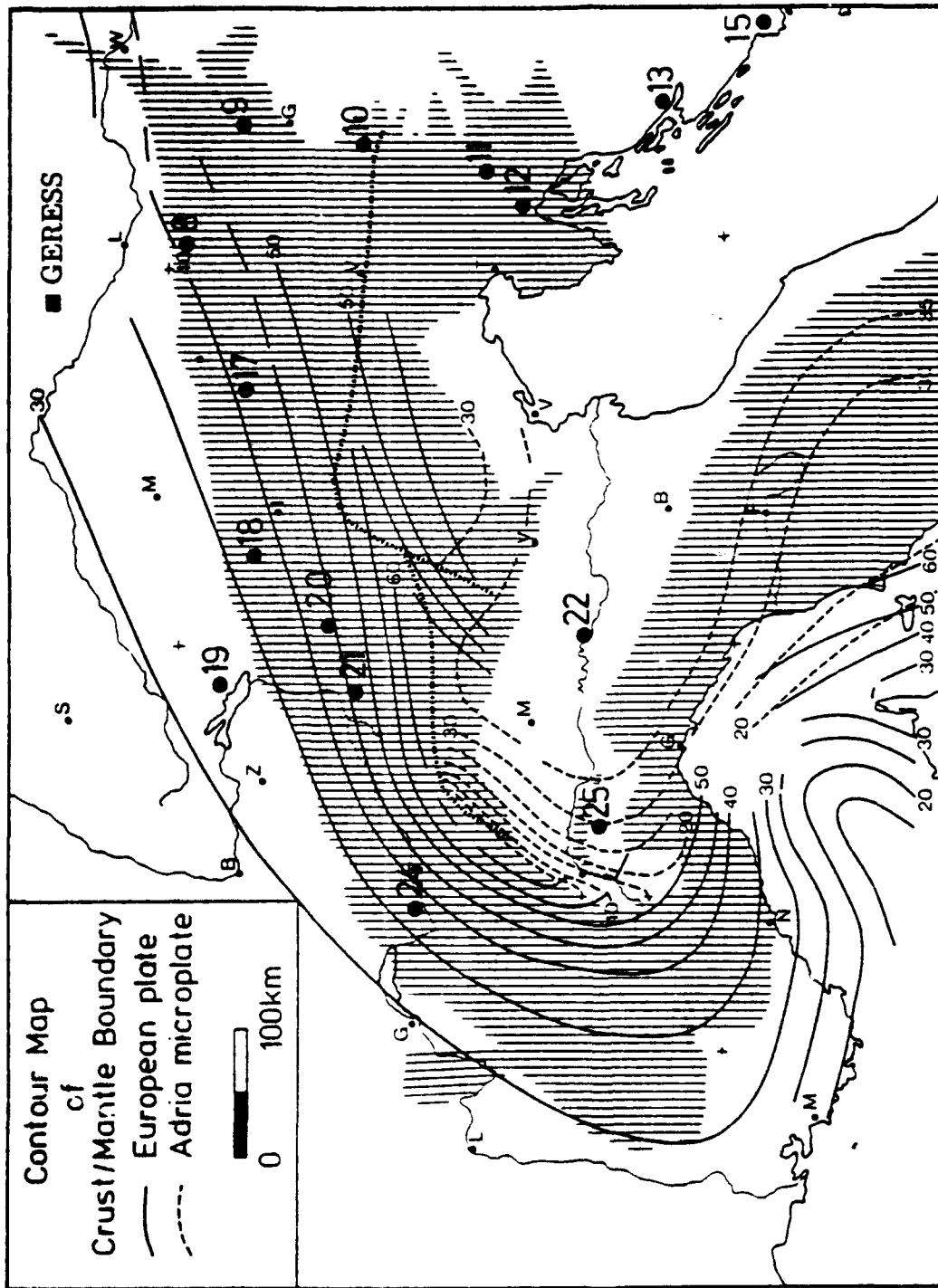

Figure 5.19

Figure 5.20

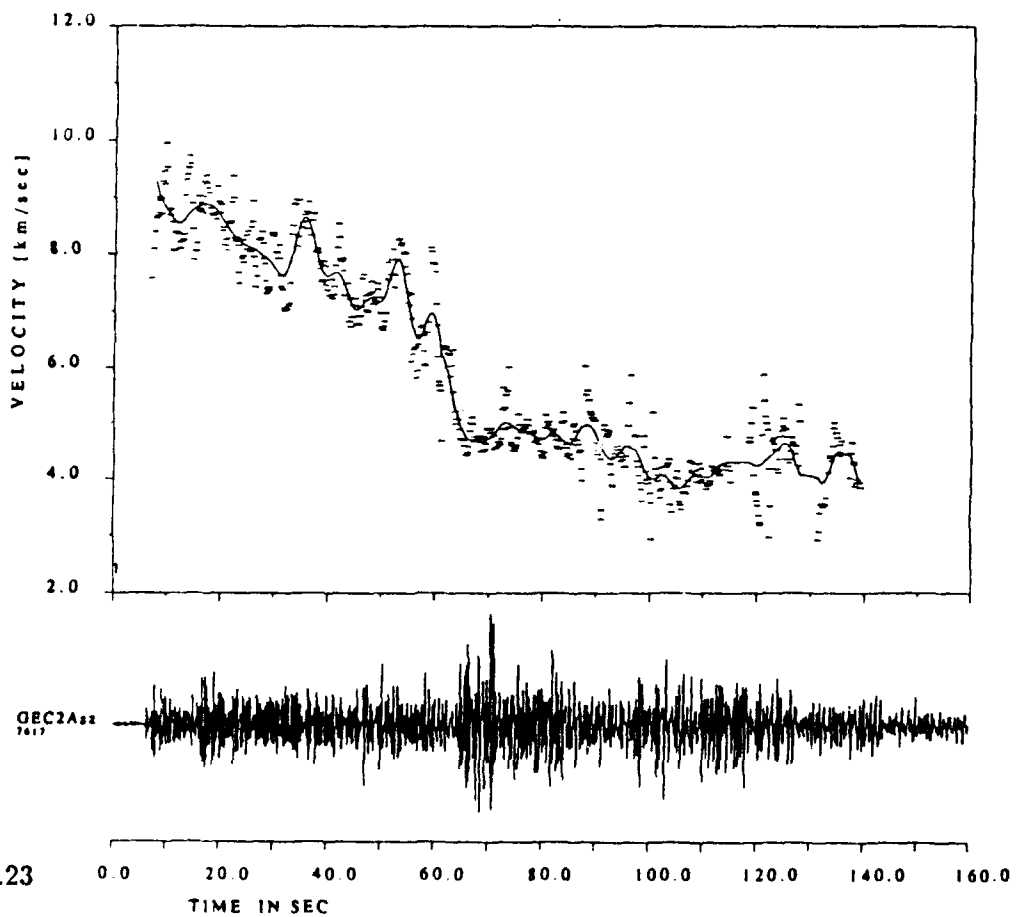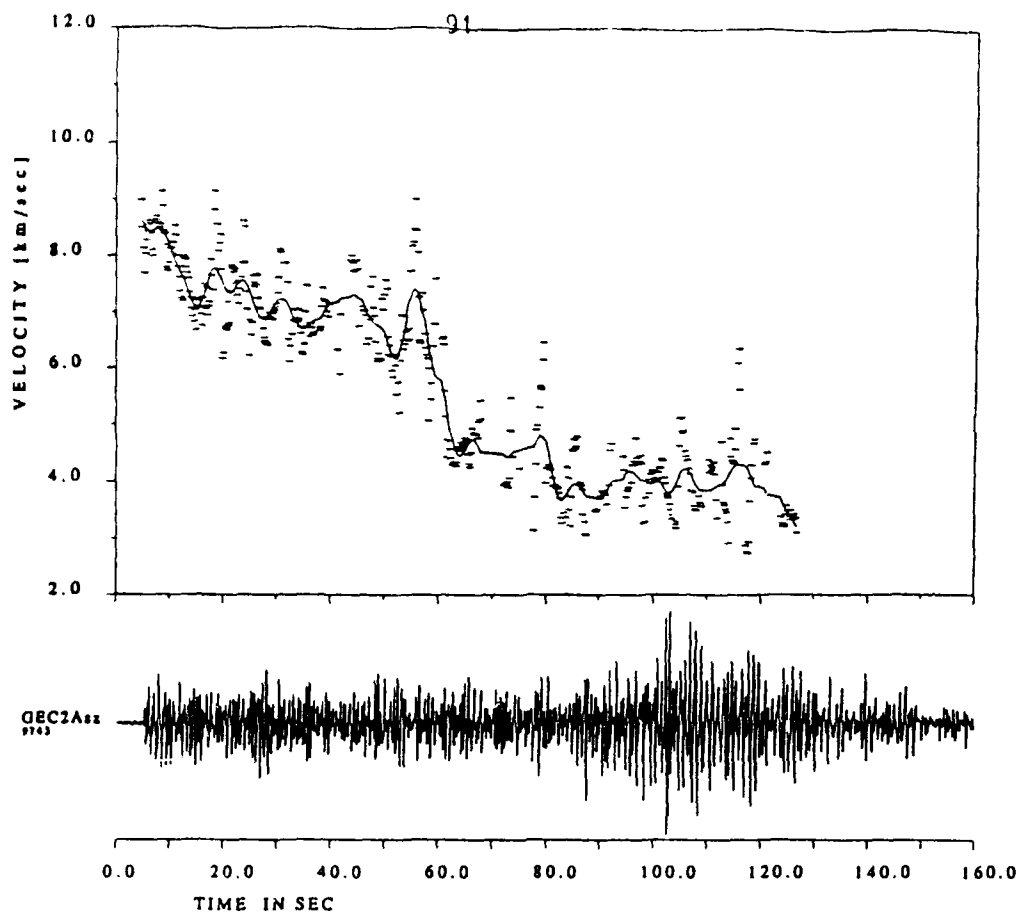Figure 5.21

Figure 5.22

Figure 5.23

6 Discrimination of tectonic earthquakes and quarry blasts at regional distances from GERESS

Jan Wüster

6.1 Introduction

In the Vogtland area, about 180 km to the NW of the GERESS regional seismic array, both natural and artificial seismicity is observed. The region extends on both sides of the German/Czechoslovakian border between 50° and 50° 30' northern latitude and 12° and 13° eastern longitude (see the map sketch (fig. 1.))

Natural seismicity occurs mainly in the form of earthquake swarms. The last major swarm took place in December 1985 and January 1986 and was studied extensively (Results were compiled by Bormann, 1989), but two smaller swarms and several single events have been recorded since the GERESS array became operational in 1990. Several German and Czech institutions operate seismic stations in or near the area and a common earthquake bulletin (Neunhöfer et al., in prep.) is being published. *Artificial seismicity* occurs in the form of quarry blasts, mostly near the town of Karlovy Vary in Western Bohemia. Such blasts do not normally attract the attention of seismological observers. Although recorded by seismographs, these events are usually identified by heuristic criteria and excluded from further processing. Fortunately, the staff at Moxa seismological observatory maintain a list of quarry blasts located with the aid of a local network of four stations (Klinge, pers. comm.)

In a CTB context as well as in the day to day operation of a sensitive regional array such as GERESS, robust procedures are most desirable to identify different types of artificial seismicity (quarry blasts, mining induced events) and to discriminate them from natural seismicity. The Vogtland area offers the opportunity to test various discrimination criteria with a uniform data set of high frequency high resolution digital recordings from GERESS in a setting, which minimizes wave-path and distance effects that usually complicate discrimination studies.

A look at the data will motivate the approaches chosen for discrimination.

In fig. 2, GERESS seismograms[1] of a typical Vogtland earthquake and a typical quarry blast are compared. The earthquake, VB521 (upper trace) was the main shock of an earthquake series occurring on March 24th, 25th and 26th, 1991, it had a local magnitude of $M_L(GEC2) = 2.8$. The quarry blast, VS016 (lower trace), originated close to Karlovy Vary on May 25th, 1991, at 11.01 hrs UT — like most of the blasts it was detonated shortly after 13 hrs local time, which corresponds to 11 hrs UT in summer and 12 hrs UT in winter. Its local magnitude was $M_L(GEC2) = 2.1$.

The most striking differences between the two seismograms are

- the amplitudes of P-wave impulses (much lower in the earthquake seismograms)

- the frequency content of the S-wave group (maximum at higher frequencies in the earthquake seismogram)

- the excitation of surface waves (very clear in the blast seismogram)

These different properties were also among the heuristic criteria for quarry blast discrimination mentioned by German seismological observers at a meeting in Jena on June 24th, 1991. This study aims at substantiating and quantifying these differences in the following way:

i) In the time domain, amplitude ratios between different wave groups are calculated and used as discriminants (section VI.C.1.)

ii) Characteristic properties of S-wave groups in the frequency domain (spectral peaks and slopes) are demonstrated and extracted using ARMA modeling (section VI.C.2.) It is found that very few ARMA parameters are required to achieve a reasonable discrimination down to a magnitude of $M_L(GEC2) = 1.7$.

iii) Application of spectral analysis not only to certain wave groups but to short time windows along the whole seismogram leads over to sonogram methods (section VI.C.3.) The sonogram detector (Joswig 1990) is applied to the data and found to discriminate well, down to even lower magnitudes.

---

[1] unless otherwise indicated the data used for this study were recorded by the GS13 high frequency element at GERESS station GEC2, sampled at 120 Hz. The seismometer response is flat to velocity from 1 ... 48 Hz. For details on seismometer transfer functions and filters see Wüster, 1991.

iv) Finally, sonograms are searched for time independent structures (section VI.C.4) following Hedlin et al. (1989.) The presence of such structures is shown to be a powerful discriminant.

6.2 The data set

A preliminary version of the Vogtland seismological bulletin during the period 01/90 ... 06/91 (VGT, Neunhöfer et al., in prep.) as well as a list of quarry blasts located with the Moxa local network during the period 3/91 ... 6/91 (MOX, Klinge, pers. comm.) were compared to the detection lists produced by the experimental on-line processing system operated at GERESS (see Jost, this report.) Coincident entries with $M_L \geq 1.0$ (except one event with $M_L = 0.7$ to be used as a test for the sensitivity of the methods) were selected, the corresponding waveforms retrieved from the GERESS data archives and placed in online disc storage. The data set thus assembled comprises 22 quarry blasts (see table 1b) of fairly uniform magnitudes around $M_L(\text{GEC2}) = 2.0$ and 39 earthquakes (see table 1a) with magnitudes ranging between $0.7 \leq M_L(\text{GEC2}) \leq 3.0$, with 15 shocks equal or above $M_L(\text{GEC2}) \geq 1.7$. Locations of these events are plotted in fig. 3. (Note that several locations coincide on the map, making the number of epicenter symbols smaller than the number of events in table 1.)

From table 1 the tendency of Vogtland earthquakes to occur in series is confirmed, the largest series having occurred on 24.03 – 26.03.91 (20 members listed) while blasts are usually (with few exceptions) detonated around 13 hrs local time. Blasts also seem to originate from few quarries. While these peculiarities facilitate the a priori association of events with earthquakes and quarry blasts, they also imply a certain uniformity within the two populations of the data set, for example with regard to focal mechanisms and source properties. This uniformity favours the success of discrimination using the Vogtland data set but at the s_me time possibly restricts simple generalization of the methods developed to different wave paths and/or different epicentral areas.

6.3 Discrimination methods

6.3.1 Amplitude ratios

The most extensively used technique for the discrimination between earthquakes and underground nuclear explosions, m_b/M_s and its offsprings (see

Dahlmann & Israelson, 1977, chapter 10) is based on amplitude ratios between different wave groups. However, the amplitudes from which M_s is calculated are measured in the 20 sec passband of long period seismographs or corresponding simulations from broad band digital records. For this reason these techniques are hardly applicable below magnitude $m_b = 4$, because for smaller events long period surface waves are not observed.

Modifications of the of the m_b/M_s-determinants, adapted to smaller events at regional distances, are the L_g/P_g and the L_g/R_g maximum amplitude ratios, reviewed, among others, by Pomeroy et al. (1982) and applied to NTS explosions and western United States earthquakes by Taylor et al. (1989.) The latter authors report the discriminants to perform poorly even for a multi-station average. L_g/P_g ratios tended to be larger for earthquakes than for explosions, but with considerable scatter, and L_g/R_g could not be applied, because these surface waves are hardly observed in the western US.

In order to obtain these discriminants from the Vogtland data set, the following batch process was implemented:

- From each event 4 time-windows of 10 sec duration were used

  window N containing the noise preceding the first onset of the event

  window P containing P_n, P_g and P coda

  window S containing S_n, S_g (L_g) and S coda, and

  window O containing surface waves, presumably R_g [2]

- All time windows are high pass filtered at 0.5 Hz (window O at 0.3 Hz.)

- In each window the maximum absolute amplitude is measured and stored.

- Ratios amp(S)/amp(P) and amp(S)/amp(O) can then be calculated, as well as signal/noise ratios for windows P, S and O.

Figures 4 and 5 illustrate the procedure. Discrimination plots (figures 6 and 7) are obtained by plotting the amplitude ratios against log amp(S), which substitutes local magnitude in the absence of large variations of epicentral

---

[2]Without a clear phase onset, window O starts immediately after the end of window S, i.e. 10 seconds after the first S-onset identified. For an average epicentral distance of 180 km this corresponds to a group velocity window of 2.9 ...2.5 km/s using Jeffreys-Bullen travel times. If the method were to be applied to data sets with greatly varying epicentral distances, proper group-velocity windows would have to be used instead of windows with fixed durations.

distance. The decision lines were drawn by hand without statistical considerations other than minimizing misclassifications (misclassification costs were not weighted.)

The percentages of misclassification are surprisingly small taking into account that discrimination is based on single station data only:

$\frac{amp(S)}{amp(P)}$ for quakes 5.1%, for blasts 4.5%

$\frac{amp(S)}{amp(O)}$ for quakes 7.7%, for blasts 9.1%

However, the "impressive success" is actually a result to the uniformity of the data set discussed above (for example uniformity in radiation characteristics of the foci as well as in propagation characteristics along the wave paths and magnitudes of the blasts). Most probably the results could not easily be generalized to less homogenous data. It is expected, that spectral discriminants will be more robust in this respect.

6.3.2 Spectral properties of S-wave groups

It is well-known, that the spectral content of certain wave groups can be used to discriminate earthquakes from nuclear explosions. The classical approach consists in arbitrarily choosing two relatively narrow frequency bands and calculate the energy contained in these bands for suitably delimited wave groups. An energy ratio between the upper and lower frequency band within one wave group serves as the discriminant. The energy content is either extracted by Fourier transforming the wave group and averaging the spectral components which fall into the defined bands (following Bakun & Johnson, 1970) or bandpass filtering the wave group according to the defined bands and estimating the remaining energy content based on maximum or average absolute amplitude (like Stevens & Day, 1985.)

The conclusions from these studies vary considerably: while Bakun & Johnson (1970) find explosion spectra to be relatively richer in high frequency energy, Murphy & Bennet (1982) and Taylor et al. (1988) report the opposite. Results obtained by Chael (1988) using high frequency data indicate that the contrast between the frequency content of earthquake and explosion L_g arrivals increases with frequency, because the explosion spectral slopes are much steeper.

A similar result is found using GERESS data of Vogtland earthquakes and quarry blasts. An example of two spectra is shown in fig. 8: the earthquake S-wave groups are relatively richer in high frequency energy than those from

the quarry blasts. A discrimination parameter could now be obtained by taking spectral averages in two frequency bands (e.g. 0-5 and 5-10 Hz) and calculating their ratios, or by manually determining spectral slopes. It is clear, that a large amount of arbitrariness is involved in both procedures, especially for weak events, in case of which only limited portions of the spectrum surpass the noise level. Alternatively, all 256 Fourier components could be used as inputs to a discrimination algorithm based on multivariate analysis (see Glaser et al., 1986), which provides the necessary weighting.

The approach subsequently pursued combines an objective procedure free of personal judgement with a managable number of discrimination parameters extracted.

Following a study by Harjes (1978), an ARMA-process is used to model the S-wave groups of Vogtland earthquakes and blasts. Assuming linearly spaced time-sampled data, such a process can be written as an equation of polynomials in z^{-1}:

$$Y(z) = G(z) \cdot E(z) = \frac{A(z)}{B(z)} \cdot E(z) \quad .$$

In this equation $E(z)$ symbolizes a sequence of normally distributed random numbers with mean 0 and variance 1, driving the system $G(z)$, which in turn is symbolized by a quotient of polynomials in z^{-1}: $\frac{A(z)}{B(z)}$. The effect of the multiplication in the z-domain corresponds to filtering in the time domain: forward convolution in the case of $A(z)$ (moving average = MA terms) and recursive filtering in the case of $B(z)$ (autoregressive = AR terms.) The result of this process $Y(z)$ is desired to resemble most closely $X(z)$, the z-form of the time series to be modelled. The task of modelling thus consists of adjusting the parameters of the polynomials $A(z)$ and $B(z)$ such that the distance (applying a suitable norm) between $X(z)$ and $Y(z)$ is minimized:

$$\| X(z), Y(z) \| = \min!$$

This non-linear regression problem can be solved with an iterative Gauss-Newton search (see Ljung, 1987.) Calculations were carried out using the System Identification Toolbox (Ljung, 1991.)

The degrees of the polynomials $A(z)$ and $B(z)$ and, accordingly, the number of free parameters are arbitrary but finite. Generally speaking, the approximation improves with the number of free parameters fitted, but at the same time the computational effort increases. Also, with an eye to discrimination, the number of parameters should be kept at a minimum.

In a first step, 20 free parameters (10 AR, 10 MA) will be allowed. The P and S wave groups of quarry blast VS016 as well as the noise window

preceding the event are to be modelled. The correspondence between $X(z)$ and $Y(z)$ is most conveniently checked in the frequency domain, because, as the random series $E(z)$ is a stationary process, all phase information is lost in the modelling. Seismic wave-groups, being of markedly transient nature, can not be ARMA-modelled satisfactorily in the time domain. This is, however, of no concern at this point, since we aim at extracting amplitude spectral properties only.

The spectrum of $E(z)$ being white by definition, all spectral properties of $Y(z)$ must be contained in the polynomial quotient $G(z)$. To extract them, $G(z)$ is evaluated on the upper unit semicircle in the complex plane substituting z by $e^{i\omega}$. The amplitude spectrum of $Y(z)$ is thus given by

$$P_{ARMA}(\omega) = \mid G(e^{i\omega}) \mid \quad , \quad \omega = [0 \ldots 2\pi \cdot f_{Nyquist}]$$

These ARMA spectra are displayed for each wave group of event VS016 in turn, in fig. 9. The solid lines are conventional (Welch) amplitude spectra (i.e. computed as the average of overlapping, tapered FFT-windows of 512 samples each.) The coincidence achieved is quite remarkable, given the fact, that the number of parameters describing the spectral properties has been reduced by more than a factor 10 (Welch-spectrum: 256 coefficients, ARMA: 20 coefficients.)

But there is still a margin for a further reduction of parameters, as witnessed by fig. 10a, which displays the ARMA-parameters for the S-wave group in the form of poles and zeroes of the function $G(z)$ in the z-plane: two complex conjugate pairs of poles and zeroes cancel within their ellipses of uncertainty, and uncertainties for two zeros (one real and one complex conjugate) are rather large, indicating redundancy in the model. A display of the loss function (fig. 10b), a quadratic norm measuring the closeness of $X(z)$ and $Y(z)$ against different numbers of AR-parameters used in the modelling (setting the number of MA-parameters to zero) indicates, that beyond 3 AR-parameters the fit improves only slightly with the number of parameters. For this reason, the number of AR- and MA-parameters is reduced to 3 and 1, respectively. Fig. 11 shows that the selected model order ARMA(3,1) is capable of extracting the typical features of S-group amplitude spectra of one earthquake and one quarry blast, namely corner frequency and spectral slope. The number of parameters is thus reduced to 4, which can again be displayed in a pole/zero-plot.

Looking at fig. 12 it is evident that the greatest potential for discrimination lies in the position of the complex conjugate pole, while the positions of the zeroes are almost identical and the real poles are quite close within

uncertainty limits. This impression is confirmed by further analyses of S-groups of further members of the data set. Fortunately, the position of the complex conjugate pole allows a simple interpretation: its closeness to the unit circle (i.e. its reciprocal absolute value) is a measure of the steepness of spectral slope, while its argument can be converted to an equivalent frequency which is indicative of the corner frequency of the spectrum. Thus the number of potential discrimination parameters is reduced to two, which is desirable because it is the maximum number which can be displayed in a plane graph.

The ARMA discrimination technique is implemented, in a batch process which consists of the following stages:

- S-wave groups of 10 sec duration are cut from the events of the data set

- an ARMA(3,1) model is fitted to each wave group

- the resulting $G(z)$ is expressed in terms of poles and zeroes

- the upper complex conjugate pole is selected in each case and is displayed on a graph with the axes equivalent to frequency and absolute value.

The process is applied to all events in the data set with $M_L(\text{GEC2}) \geq 1.7$. The restriction is necessary because below this level, ARMA spectra tend to be dominated by properties of the noise.

The discrimination plot (fig. 13) shows that a separation is indeed achieved, although there is a certain overlap close to the decision line, which was again drawn manually. The misclassification percentages are 0% for earthquakes and 14% for blasts. It is interesting to note, in which cases discrimination fails: the two blasts most drastically misclassified as earthquakes (VS003 and VS004) both have high frequency onsets within the S-wave group, as revealed by the high pass filter in fig. 14, probably due to an interfering small quarry blast much closer to GERESS. This mixed event situation is not successfully handled by the implemented discrimination procedure. A feasible counter-measure consists in the use of beamforming prior to ARMA-modeling. This would, however, restrict the usable frequency band to 0 ... 16 Hz, because normal GERESS array elements other than the hf-element are sampled at 40 Hz only.

Bearing in mind this restriction the above process is repeated, this time using 40 Hz single station data. The separation achieved (see the discrimination plot in fig. 15) is even clearer, but the misclassification percentages

(including the known failures VS003 and VS004, which have been excluded from fig. 16) have risen somewhat to 26 % for blasts and 7% for earthquakes.

Further experiments conducted include higher order ARMA-models and the use of P-wave groups. Higher order models do not lend themselves to obvious interpretation of parameters, but have potential, in connection with multivariate analysis, to reduce misclassifications. The P-wave groups of many earthquakes in the data set have very poor signal/noise ratios, making ARMA-modelling of the signal difficult. Again this problem could be tackled with beamforming.

It is expected that discrimination methods using spectral properties of one wave-group are less susceptible to variation in focal mechanism and radiation pattern. Simple distance corrections might suffice to generalize the methods to variable epicentral distances.

6.3.3   The sonogram detector

A sonogram is the graphic representation of spectral analysis on consecutive time-windows along a time series. Sonograms are used in the related field of phoneme recognition in automatic speech processing. The approach has been transferred to the pattern recognition problem of a small local network of seismic stations (BUG) monitoring the strongly clustered mining induced seismicity of the Ruhr district (Joswig, 1990.)

The discrimination between Vogtland earthquakes and quarry blasts poses a similar problem: basically it is the quantification of the pattern recognition, which is accomplished, in part subconsciously, by the human observer. It was therefore decided to apply the sonogram detector to the discrimination data set. The following is a short resumé of the working principles of the detector. For details, the reader is referred to Joswig (1990)

As a first step, master events are defined. These events should be regarded as "typical" for their class and their recordings should possess a sufficiently high signal/noise ratio. The master time series (including the master event and pre- and post-event noise windows) are then divided into time windows of equal length, each of which is spectral analyzed. The significant spectral range is divided into 11 logarithmically spaced bins, and the average spectral density over such a bin, corrected for noise offset, is stored in a sonogram matrix of frequency bin vs. time window. Together with an indication of noise level over each spectral bin, the sonogram matrices are stored in a master event library.

In discrimination mode each time series is treated in the same way and

tested for resemblance to the master events. The resulting test matrix is cross-correlated two-dimensionally with each of the individually adapted master event matrices from the library. Two parameters result from this process : the *fit*, which is the maximum amplitude of the cross-correlation function and the *percentage* of the actual master matrix contributing to CCF values above a certain threshold. According to the values of these parameters the following judgements are inferred about the resemblance between master event and test event:

DEFINITE for fit > 0.9 and percentage > 80%
PROBABLE for fit > 0.6 and percentage > 60%
POSSIBLE for fit > 0.4 and percentage > 20%

For the lowest category, POSSIBLE, two "guesses" are allowed by the algorithm, while in case of the higher categories only a single nomination is permitted. If none of the master events yields at least the category POSSIBLE, the test event is judged as noise: "no detection found".

For the Vogtland discrimination, the events VB521 and VS016 (see fig. 2) are used as master events. Fig. 16 shows a screendump taken during matrix generation for the quarry blast VS016 and a printout of the internal storage form of the generated matrix.

Then a batch process was implemented and all events of the data set were processed, including three completely alien events from different epicentral regions. Fig. 17 may serve as an example of the processing: a quarry blast, VS018, is being identified as a POSSIBLE Sprengung (= German term for blast.) In the following the discrimination performance of the detector is summarized.

- Of 39 earthquakes, 33 were identified as earthquakes (4 DEFINITE including the master event itself, 6 PROBABLE, 23 POSSIBLE.) Not a single quake was misclassified as blast. In 6 cases, no detection was found, all of these were low magnitude events with $M_L(\text{GEC2}) \leq 1.5$. Therefore the misclassification percentage is 0%.

- Of 23 quarry blasts, 16 were classified as blasts (2 DEFINITE including the master event itself), 11 PROBABLE, 3 POSSIBLE), 4 were classified both as POSSIBLE blast and POSSIBLE quake and 2 were misclassified as POSSIBLE quakes. Regarding the unsettled cases as "no detection found" we get a misclassification percentage of 10.5%.

- The alien events were classified as follows:
  quake from Switzerland – no detection found

quake from Austria – PROBABLE quake
mining event from Lubin – no detection found
mining event from Lubin – P-group identified as PROBABLE quake
                                       S-group identified as PROBABLE blast.

Thus the performance of the sonogram detector in a discrimination situation can be judged as excellent, taking into account that no particular care was taken in the selection of the master events and that a few events even below $M_L(\text{GEC2}) = 1.5$ were correctly discriminated.

In the current version, the sonogram detector is only applicable to closely spaced events. A further weakness from a geophysical point of view lies in the fact, that it does not give any clue as to the physical basis of the phenomena used in discrimination, in fact it was developed for automatic recognition in situations, in which no physical interpretation is available. The final discrimination method considered in this study claims both independence of epicentral distance and a physical explanation.

6.3.4 Time independent structures in sonograms

During the 1998 US/USSR joint verification experiment (JVE), chemical calibration explosions were recorded as well, close to Kasakh test site and Nevada test site, with high-frequency seismometers (Holly, 1990). Besides the calibration explosions, numerous events were recorded which are supposed to be artificial (mine blasts or quarry blasts.) Hedlin et al. (1989) calculated sonograms of the data and observed time-independent structures, i.e. patterns of spectral energy above or below a smoothed spectral average, spanning more than one seismic phase. Such patterns were identified in virtually all of the events except the calibration explosions, which were known to be single source events. The authors interpret the structures as an effect of the ripple firing technique used in mines and quarries and substantiate the hypothesis with a theoretical derivation of frequency structures to be expected from a simple ripple firing model. Alternatively, the regular modulation of spectra could be explained by multiple reflections in the uppermost layers of the crust.

The Vogtland data set was investigated for the occurrence of similar structures, closely following the approach of the named authors. To this end, the following batch process was implemented:

- The seismogram traces are numerically differentiated to make them comparable to the acceleration proportional recordings of the Kasakh

stations.

- The traces are divided into time windows of 2 sec length, overlapping by 1 sec on either side.

- The time windows are padded with zeroes on both sides, extending them to 4 sec each.

- the 4-sec-windows are frequency analyzed, averaging 7 overlapping tapered subwindows of 256 FFT-points each.

- the resulting 128 equally spaced averaged FFT components are squared and entered into a sonogram matrix.

- this matrix, the power spectrum vs. time, is displayed in a perspective graph (figs. 18 and 19, upper half)

- the square root of the matrix, corresponding to the amplitude spectrum vs. time is displayed as contour plot (figs. 18 and 19, lower half) together with the seismogram trace for comparison.

Figures 18 and 19 show the results of the process for the two events VB521 and VS016. The perspective plots give a good impression of the distribution of energy in frequency space and time, but without the chance to shift the viewpoint (as it is possible on the screen), it is difficult to discern patterns or structures. The situation improves somewhat with the contour plot: in the quarry blast sonogram (fig. 19), spectral peaks at approx. 2, 8, 12, 15 and 20 Hz are found both in the P and in the S-phase, and most of them can also be tracked in the P-coda. (Note that the spectral peaks at 5 Hz and 23 Hz are independent of the seismogram and must be disregarded as noise.)

In order to improve the visibility of structures, local peaks and troughs must be plotted, rather than absolute ones. This can be achieved by smoothing the spectral estimates using two different smoothing windows and taking the difference between the short range and the long range smoothed estimate as an indication of local peak if positive and local trough if negative. In effect this amounts to bandpass filtering the sonogram data in the frequency direction. Fig. 20 shows 4 cross-sections through the sonogram of event VS016 in frequency direction around the P-onset at $t = 10$ sec. Spectral estimates, raw and smoothed (short range filtered at a "wavelength" of 2 Hz, long range at 6 Hz) are plotted for each section. In the bottom line a black star is printed for local troughs, leaving white blanks for local peaks.

These white and black elements are stored into a digital matrix, which is printed for every event. Figure 21 shows the digital matrices for two

earthquakes (left) and two blasts (right.) While for the blasts horizontally connected white bands are observed spanning the seismogram from $t = 10$ to $t = 50$ sec, such structures are absent from the matrices obtained from earthquakes (disregarding noise bands.)

The number of non-noise bands was counted for all events of the data set, which leads to the following results:

- Of 29 earthquakes analyzed, 24 show no bands, 4 show 1 band and one was too noisy to be analyzed.

- Of 20 quarry blasts analyzed, 4 show more than 3 bands, 7 show 2 bands, 1 shows 1 band and 1 show no band.

Taking therefore a number of bands greater than 1 as an indication for quarry blasts, we get a misclassification percentage of 10% for blasts. Nothing comparable can be said about the earthquakes, because only negative evidence is available. It is desirable to automatize the search for structures as well. One possible solution, again following a paper by Hedlin et al. (1990) would be a second, 2-dimensional, Fourier analysis of the sonogram matrix, a method adjacent to cepstral analysis.

Further studies should aim at explaining the spectral modulation encountered in quarry blast seismograms, either by confirming the use of ripple fire techniques with blast delays compatible with the modulations observed or by computing and analyzing theoretical seismograms using repetitive sources and/or realistic crustal layering capable of generating multiple reflections for very shallow sources.

6.4 Synopsis of discrimination results and discussion

Five different methods of discrimination have been applied to the Vogtland data set. The results obtained are summarized in table 2. Certainly one cannot expect to achieve perfect discrimination with the application of any single criterion. An effective approach will have to make use of several discriminants. In table 2 a simple scheme of majority voting has been adopted. Each discriminant has one vote, unability to apply the discriminant to a certain event (e.g. for reason of poor signal/noise ratio) or inconclusiveness is counted as abstention.

Under this joint discrimination scheme, by far the most cases (93%) give rise to a comfortable majority (difference > 2), in most cases (77%) unanimity

is achieved among the votes cast. Majority voting reduces the number of misclassified earthquakes to 0 and the number of misclassified blasts to 1 (4.5%.) Moreover, the one quarry blast misclassified as an earthquake even after voting (VS011) is one of the 3 blasts in the data set not detonated shortly after 12 hrs local time, but instead at 10:57 hrs local time. Thus event VS011 might indeed be an earthquake, which was erroneously listed among the blasts for its proximity in origin time and epicentre to the rest of the blasts, but the majority is merely by 1 vote and should not be overstressed.

Extensions of this study are both necessary and obvious. For one, other promising discriminants can be tried on the data set, for example the coda decay rate advocated by Su et al. (1991) and successfully applied to a suite of Southern California earthquakes and quarry blasts. Also, the array capabilities of GERESS have as yet not been taken advantage of. Apart from increasing the signal/noise ratio by beamforming, stacking of the digital sonogram matrices obtained from each channel could be tried, as proposed by Hedlin et al. (1990) for the NORESS array, leading to a quantitative evaluation of structures in frequency space.

The data set needs to be enlarged to include also quarry blasts with $M_L(GEC2) \neq 2$ and single events independent of clusters and series, if such events can be found. As a first step towards generalization of the discrimination methods, the same set of events may be studied using seismograms from different stations. German Regional Network stations CLZ, TNS and WET are available for this purpose, as well as a newly installed Czech local area digital network at Kraslice (Firbas, pers. comm.)

Finally a full generalization of discrimination methods will hardly be possible without an explanation of their functioning and at times "failing" in terms of the underlying physical principles.

Acknowledgements

References

Bakun, W.H. & Johnson, L.R. (1970)
Short period spectral discriminants for explosions. Geophys. J. R. astr. Soc. 22, 139-152.

Bormann, Peter [Ed.] (1989)
Monitoring and analysis of the earthquake swarm 1985/86 in the region Vogtland/Western Bohemia. Zentralinstitut für Physik der Erde. Veröffentlichung Nr. 110, ISSN 0514-8790. Potsdam, 1989.

Chael, Eric P. (1988)
Spectral discrimination of NTS explosions and earthquakes in the southwestern United States using high-frequency regional data. Geophys. Res. Lett. 15 No 6, 625-628.

Dahlmann, O. & Israelson, H. (1977)
Monitoring Underground Nuclear Explosions. Amsterdam (Elsevier), 1977.

Glaser, Ronald E. et al. (1986)
Regional discrimination of NTS explosions and western U.S. earthquakes: multivariate discriminants. Lawrence Livermore National Laboratory UCID 20930. Livermore, CA, Nov 17th, 1986.

Harjes, Hans-Peter (1978)
Spektralanalytische Interpretation seismischer Aufzeichnungen. Geologisches Jahrbuch /E 17. Hannover (Bundesanstalt für Geowissenschaften und Rohstoffe), 1978.

Hedlin, A.H., Minster, J.B. & Orcutt, J.A. (1989)
The time-frequency characteristics of quarry blasts and calibration explosions recorded in Kazakhstan, USSR. Geophys. J. Int. 99, 109-121.

Hedlin, A.H., Minster, J.B. & Orcutt, J.A. (1990)
An automatic means to discriminate between earthquakes and quarry blasts. Submitted to Bull. Seismol. Soc. Am.

Given, Holly K. et al. (1990)
High-frequency seismic observations in Eastern Kasakhstan, USSR, with emphasis on chemical explosion experiments. J. Geophys. Res. 95 No B1, 295-307.

Jost, Michael M. (1992)
GERESS Status Report April 1991 – February 1992 (contained in this report).

Joswig, Manfred (1990)
Pattern recognition for earthquake detection. Bull. Seism. Soc. Am. 90 No 1, 170-186.

Joswig, M. & Schulte-Theis, H. (1992)
Master event correlation of weak local earthquakes by dynamic waveform matching. Submitted to Geophys. J. Int.

Ljung, Lennart (1987)
> System Identification, Theory for the User. Englewood Cliffs, NJ (Prentice-Hall), 1987.

Ljung, Lennart (1991)
> System Identification Toolbox for Use with MATLAB™ . Natick, MS (The Mathworks, Inc.), 1991.

Murphy, J.R. & Bennet, T.J. (1982)
> A discrimination analysis of short-period regional seismic data recorded at Tonto Forest Observatory. Bull. Seism. Soc. Am. 72 No 4, 1351-1366.

Neunhöfer, H. et al.
> Bulletin of microearthquakes from the Vogtland region; period 1987-1990, in preparation.
> and:
> Preliminary Bulletin of Vogtland microearthquakes 1991, first half year, manuscript.

Pomeroy, P.W., Best, J.W. & Mc Evilly, Th.V. (1982)
> Test ban treaty verification with regional data — a review. Bull. Seism. Soc. Am. 72 No 6, S89-S129.

Stevens, L.S. & Day, St.M. (1985)
> The physical basis of m_b : M_S and variable frequency magnitude methods for earthquake/explosion discrimination. J. Geoph. Res. 90 No B4, 3009-3020.

Su, F., Aki, K. & Biswas, N. (1991)
> Discrimination of quarry blasts from earthquakes using coda waves. Bull. Seism. Soc .Am. 81 No 1, 162-178.

Taylor, St.R., Sherman, N.W. & Denny, M.D. (1988)
> Spectral discrimination between NTS explosions and western United States earthquakes at regional distances. Bull. Seism. Soc. Am. 78 No 4, 1563-1579.

Taylor, Steven R. et al. (1989)
> Regional discrimination between NTS-explosions and earthquakes. Bull. Seism. Soc. Am. 79 No 4, 1142-1176.

Wüster, Jan (1991)
> Signal transfer functions and sensitivities for GERESS seismometers in: Advanced Waveform Research, Methods for GERESS Recordings. Annual Report 15 Feb 1990 – 14 Feb 1991. Lehrstuhl für Geophysik Prof. Dr. H.-P. Harjes. Bochum (Ruhr-Universität), 15 April 1991.

108

Table and figure captions

Fig. 6.1

The Vogtland area in the German/Czechoslovakian border region. The epicenters of two events (VB521 and VS016) mentioned in the text are indicated. The GERESS regional array is situated at approx. 180 km distance to the SE.

Fig. 6.2

A typical Vogtland earthquake (VB521) and a typical quarry blast from Karlovy Vary (VS016) recorded at GEC2.

Tab. 6.1a

List of earthquakes used in this study

Tab. 6.1b

List of quarry blasts used in this study

Fig. 6.3

Epicenters of earthquakes (polygonal symbols) and quarry blasts (stars) used in this study. Locations were taken from the preliminary Vogtland Bulletin (Neunhöfer et al., in prep.) for the quakes and from a list maintained at Moxa seismological observatory (Klinge, personal comm.) for the blasts.

Fig. 6.4

10 sec time windows N (pre-event noise), P (P-wave group), S (S-wave group) and O (surface-wave group) cut from quarry blast VS016. Traces are normalized, but the maximum amplitudes in digital counts are indicated on the left margin.

Fig. 6.5

The same display as in Fig. 6.4, using earthquake VB521.

Fig. 6.6

Amplitude ratio discrimination plot. Maximum S-amplitude/max. P-amplitude plotted against the logarithm of max. S-amplitude. The decision line was drawn by hand.

Fig. 6.7

Amplitude ratio discrimination plot. Maximum S-amplitude/max. surface-wave amplitude plotted against the logarithm of max. S-amplitude. The decision line was drawn by hand.

Fig. 6.8

The S-group power spectra (obtained by conventional spectral analysis) are plotted subtracting the respective pre-event noise spectra. Spectral slopes can be estimated (dashed lines) and used for discrimination. Alternative discriminants could be the spectral maximum or the ratio between average spectral densities over two suitably selected frequency bands. All these methods comprise a great deal of arbitraryness.

Fig. 6.9

Conventional power spectra (solid line) of the P- and S-wave groups and a pre-event noise window of event VS016 are compared to ARMA (10,10) spectral estimates. The fit is remarkable taking into account that the number of parameters is reduced by a factor of 10 using the ARMA-method.

Fig. 6.10a (upper half)

Pole/zero plot of the ARMA(10,10)-model of the S-group of event VS016. Poles (x) and zeros (o) are depicted in the complex z-plane, their uncertainties (2σ–ellipses) are indicated. As required for a stable system, all poles are within the unit circle. Since the zeroes are within the unit circle as well, the system is also minimum phase. Pole/zero cancellations as well as large error ellipses indicate that there is head-room for a further reduction in the number of parameters.

Fig. 6.10b (lower half)

As a test for the necessary model order, the minimum loss function (an indication for the quality of fit of the model) is plotted against the number of AR-parameters. Beyond 3, the improvement of the fit is only slight.

Fig. 6.11

Conventional S-group power spectra of typical quake (VB521) and typical blast (VS016) (upper plot) compared to ARMA(3,1) spectral estimates of the same data (lower plot) It is clear that the ARMA-model (using 4 parameters only) can extract "typical" information suitable as a discriminant.

Fig. 6.12

Pole/zero-plot of earthquake (upper half) and quarry blast (lower half) S-group ARMA(3,1) spectral estimate.

Fig. 6.13

Discrimination plots using parameters derived from ARMA(3,1)-poles.

On the upper graph, the position of the real pole is plotted against
the equivalent frequency of the imaginary pole. On the lower graph,
the absolute value of the imaginary pole is used instead. Decision lines
were drawn manually. In the end the lower graph was preferred for
discrimination because of the interpretation of the y-axis (see text).

Fig. 6.14

Application of a HP-filter reveals a high frequency onset within the
S-wave group of event VS003 and explains, why the event was misclas-
sified by the ARMA-discriminant.

Fig. 6.15

Discrimination plot equivalent to Fig. 6.13, lower half. This time, 40
Hz-Data were used.

Fig. 6.16

Screendump during master-event mask generation for event VS016. The
sonogram mask (upper window) is calculated from the seismogram
(middle window). Onsets are found using STA/LTA-detection (lower
window) which is irrelevant for the present application. The sonogram
matrix, displayed on the screen on a colour scale (which is transferred
to a grey-scale in the screendump) is stored away in the form printed
below. Each letter is an indication of spectral power (a...z) over a spec-
tral bin (y-axis: 0.3...15 Hz) within a time window of 1.5 sec duration
on the time (x) axis. The first column is an indication of noise offset
for the respective bins obtained by analyzing pre- and post-event noise
windows.

Fig. 6.17

Screendump during discrimination mode on event VS018. The addi-
tional window at the bottom shows the result of cross-correlating the
sonogram matrix of the actual event (upper window) with each of the
matrices from a master-event library. In this case the result is POSSI-
BLE Sprengung (blast) while the CCF for Beben (quake) never exceeds
the threshold.

Fig. 6.18

Sonogram of event VB521. In the perspective plot (upper half), the
time-axis extends from the left foreground (t=1 sec) to the right back-
ground (t=99 sec). The P-onset is set to t=10 sec. The linearly spaced
frequency axis is rectangular to the time axis with small frequency val-
ues in the background. Elevation is proportional to spectral power. In

the contour plot (lower half), the square root of spectral power (spectral amplitude) is displayed with 20 linearly spaced contour lines in the time/frequency plane. The seismogram trace is displayed for reference.

Fig. 6.19

The same plot as in the preceding Figure 18, for event VS016. The sonogram reveals time-independent structures at approx 2, 8, 12, 15 and 20 Hz in the seismograms. Note that structures observed at 5 Hz and 23 Hz are noise.

Fig. 6.20

Four cross-sections through the sonogram for event VS016. The noise spectrum is displayed in the first window at t=9 sec, with spectral peaks at 5, 9 and 22 Hz. In the following windows the P-onset (spectral peaks at 11 and 20 Hz) is seen surpassing the noise. Two different smoothing filters are applied (dashed and dotted lines) and the short range smoothed spectrum subtracted from the long range smoothed one. If the result is positive, the structural trace at the bottom is left blank, otherwise a star is printed. The structural trace is thus indicative of local peaks and troughs of the sonogram.

Fig. 6.21

Digital matrices composed from the structural traces (explained in previous figure caption). In the quarry blast-matrices on the right, time-independent structures [white horizontal bands extending from t=10 sec (P-onset) to t=60 sec (S-coda)] can be observed, which are absent from the earthquake matrices on the left. Note that structures starting at t=0 sec and extending past t=70 sec are noise.

Tab. 6.2

Results of application of individual discriminants on the data set (table 2a on the quakes and table 2b on the blasts). Circles stand for the discrimination result "earthquake", while stars indicate the result "quarry blast". A dash is printed in cases, when the individual discriminant could not be applied, and a question mark indicates that results were inconclusive. The last column lists the vote taken and the final verdict. Only one event (VS011) is misclassified, but may well have been misplaced on the blast list in the first place for reasons given in the text.
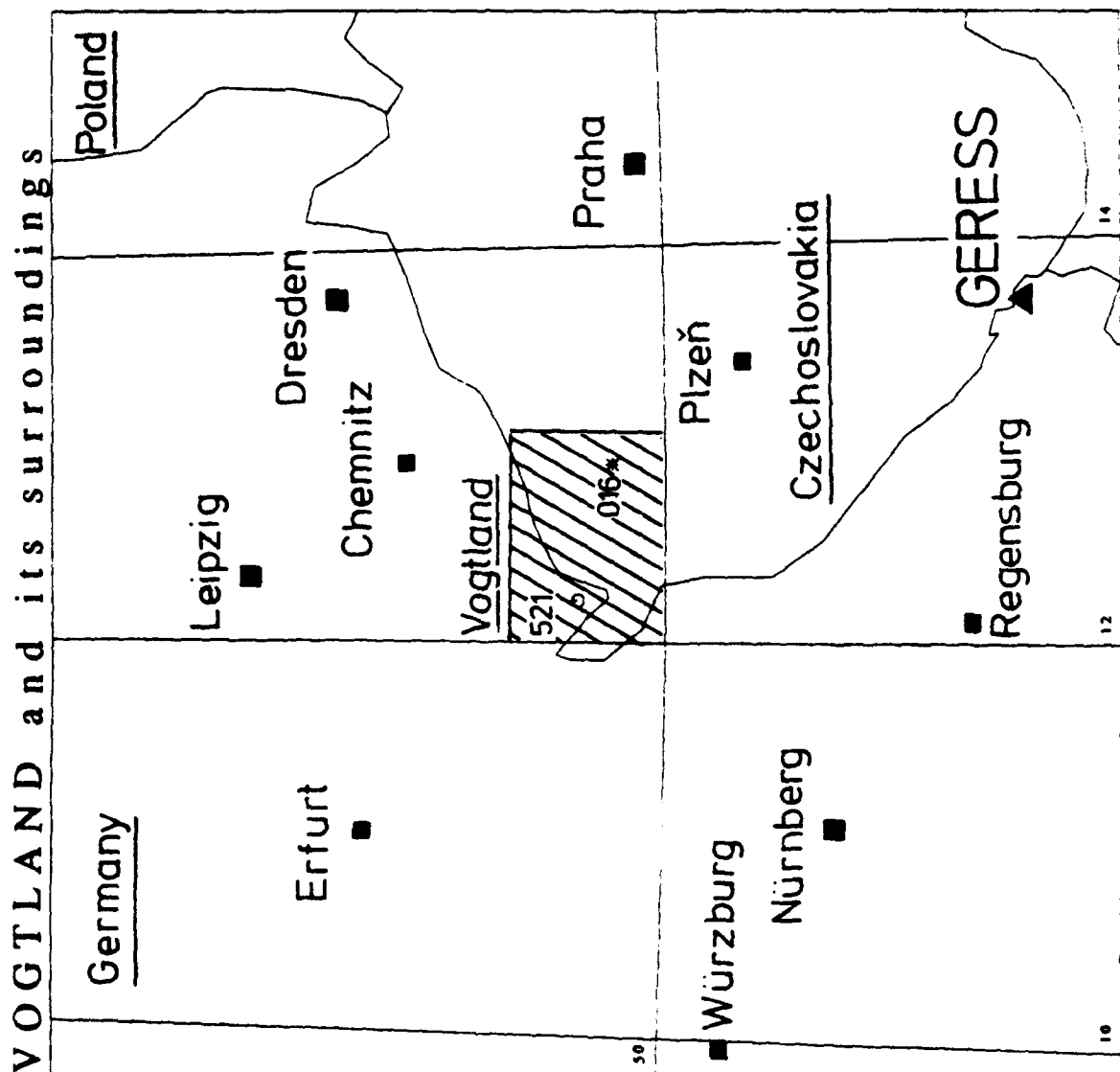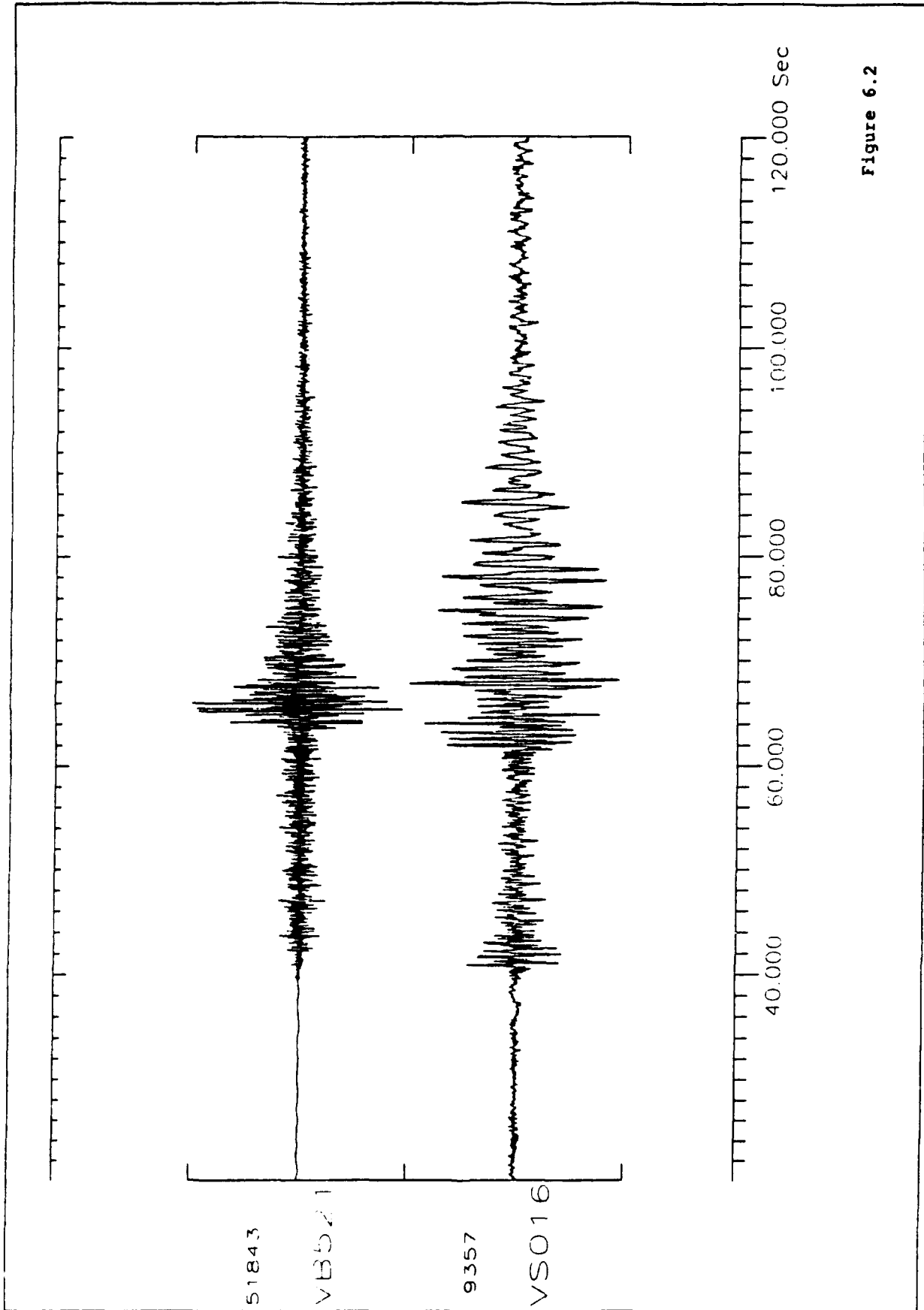
112

VOGTLAND and its surroundings

Germany

Poland

Leipzig

Dresden

Chemnitz

Erfurt

Vogtland
521
516*

Würzburg

Nürnberg

Plzeň

Praha

Czechoslovakia

Regensburg

GERESS

Figure 6.1

Figure 6.2

event #	date	GEC2 arrival	epicentre	M_L
VB504	20.05.90	06:36:06.7	50.363N 12.459E	1.31
VB505	03.06.90	00:40:05.6	50.251N 12.492E	1.25
VB506	03.06.90	01:55:18.7	50.242N 12.479E	1.07
VB507	22.08.90	18:30:40.4	50.418N 12.164E	2.35
VB508	23.09.90	20:15:57.2	50.463N 12.175E	1.47
VB509	23.09.90	20:28:51.1	50.462N 12.179E	1.12
VB510	23.09.90	23:26:25.5	50.427N 12.104E	1.07
VB511	27.09.90	16:18:31.1	50.457N 12.210E	1.70
VB512	15.11.90	07:59:10.3		1.08
VB513	15.11.90	23:23:07.9	50.254N 12.817E	1.52
VB514	17.11.90	18:18:36.2	50.263N 12.301E	1.90
VB515	13.02.91	03:34:23.5	50.43 N 12.04 E	1.33
VB516	24.03.91	05:05:35.9	50.28 N 12.21 E	2.62
VB517	24.03.91	05:35:50.3	50.28 N 12.22 E	1.64
VB518	24.03.91	06:58:31.4	50.31 N 12.22 E	1.52
VB519	24.03.91	09:32:41.5	50.31 N 12.22 E	1.31
VB520	24.03.91	09:39:05.0	50.31 N 12.22 E	1.81
VB541	24.03.91	09:47:31.2		0.94
VB521	24.03.91	14:33:59.5	50.28 N 12.21 E	3.00
VB522	24.03.91	14:36:28	50.31 N 12.22 E	1.31
VB523	24.03.91	15:01.15.4	50.28 N 12.22 E	2.06
VB524	24.03.91	15:41:35.1	50.28 N 12.22 E	1.88
VB525	25.03.91	14:41:41.9	50.31 N 12.22 E	1.35
VB526	25.03.91	14:54:45.1	50.28 N 12.21 E	2.63
VB527	25.03.91	15:40:06.2	50.31 N 12.22 E	1.81
VB528	25.03.91	16:26:18.1	50.31 N 12.22 E	1.77
VB529	25.03.91	17:51:57.8	50.31 N 12.22 E	1.47
VB530	25.03.91	18:46:57.5	50.31 N 12.22 E	1.33
VB531	25.03.91	21:11:10.9	50.31 N 12.22 E	1.41
VB532	25.03.91	22:32:18.5	50.31 N 12.22 E	1.71
VB533	26.03.91	08:54:32.4	50.29 N 12.22 E	1.77
VB534	26.03.91	09:03:43.4	50.31 N 12.22 E	1.33
VB535	22.04.91	22:25:40.7	50.35 N 12.14 E	1.37
VB536	05.05.91	17:15:39.8		1.11
VB537	10.05.91	20:03:57.3	50.790N 12.070E	1.43
VB538	19.05.91	03:22:41.7	50.35 N 12.40 E	2.91
VB539	03.06.91	23:05:08.0	50.00 N 12.23 E	1.25
VB540	30.06.91	05:06:59		0.68
VB542	30.06.91	04:24:25.7	50.49 N 12.16 E	1.21

Table 6.1a

event #	date	GEC2 arrival	epicentre	M_L
VS001b	11.03.91	12:03:52.7	50.170N 13.050E	1.98
VS003	14.03.91	12:05:01.8	50.170N 12.860E	1.83
VS004	15.03.91	12:15:01.4	50.230N 12.970E	1.93
VS005	18.03.91	12:04:53.2	50.160N 12.900E	2.02
VS006	20.03.91	12:05:48.8	50.160N 12.920E	1.94
VS007	21.03.91	12:04:43.4	50.170N 12.920E	2.05
VS008	22.03.91	12:23:45.0	50.190N 12.810E	1.94
VS009	22.03.91	12:33:53.7	50.160N 12.890E	2.03
VS010	23.03.91	12:01:24.2	50.200N 12.820E	1.99
VS011	03.04.91	09:57:41.9	50.160N 12.600E	1.81
VS012	02.05.91	11:06:38.7	50.185N 12.760E	1.93
VS013	02.05.91	12:48:28.3	50.184N 12.186E	2.03
VS014	08.05.91	11:15:06.3	50.177N 12.823E	2.00
VS015a	23.05.91	11.01.33.3	50.130N 12.887E	2.12
VS016	25.05.91	11:01:57.2	50.170N 12.900E	2.13
VS017	26.05.91	11:01:00.8	50.140N 12.850E	2.14
VS018	28.05.91	11:04:19.8	50.196N 12.741E	2.01
VS019	11.06.91	11:02:59.9	50.160N 12.862E	2.08
VS020	20.06.91	11:01:44.8	50.160N 12.900E	1.96
VS021	20.06.91	11:46:04.6	50.250N 12.830E	1.80
VS022	22.06.91	10:59:03.1	50.180N 12.800E	2.15
VS023	27.06.91	11:05:08.1	50.170N 12.930E	1.93

Table 6.1b

VOGTLAND Data Set

Figure 6.3

BUMP(0.8,0.8)   11.01.45.100

BUMP(0.3,0.3)   11.01.56.600

BUMP(0.8,0.8)   11.02.19.000

BUMP(0.3,0.3)   11.02.29.000

506 N

4192 P

9280 S

7510 O

0.000   5.000   10.000 Sec

1991-145   VSO16   Figure 6.4

118

Figure 6.5

amplitude ratio discrimination
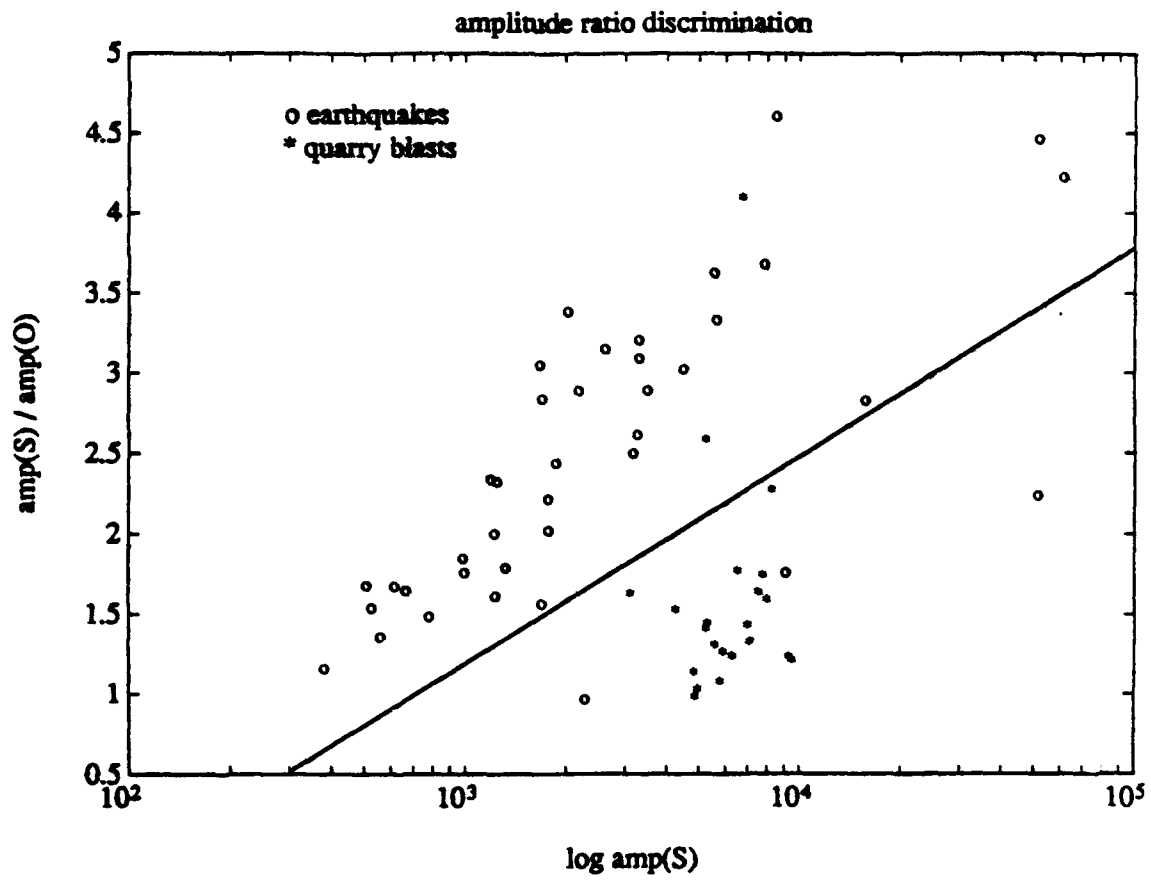
Figure 6.6

Figure 6.7

S-group power spectra ./. noise spectra
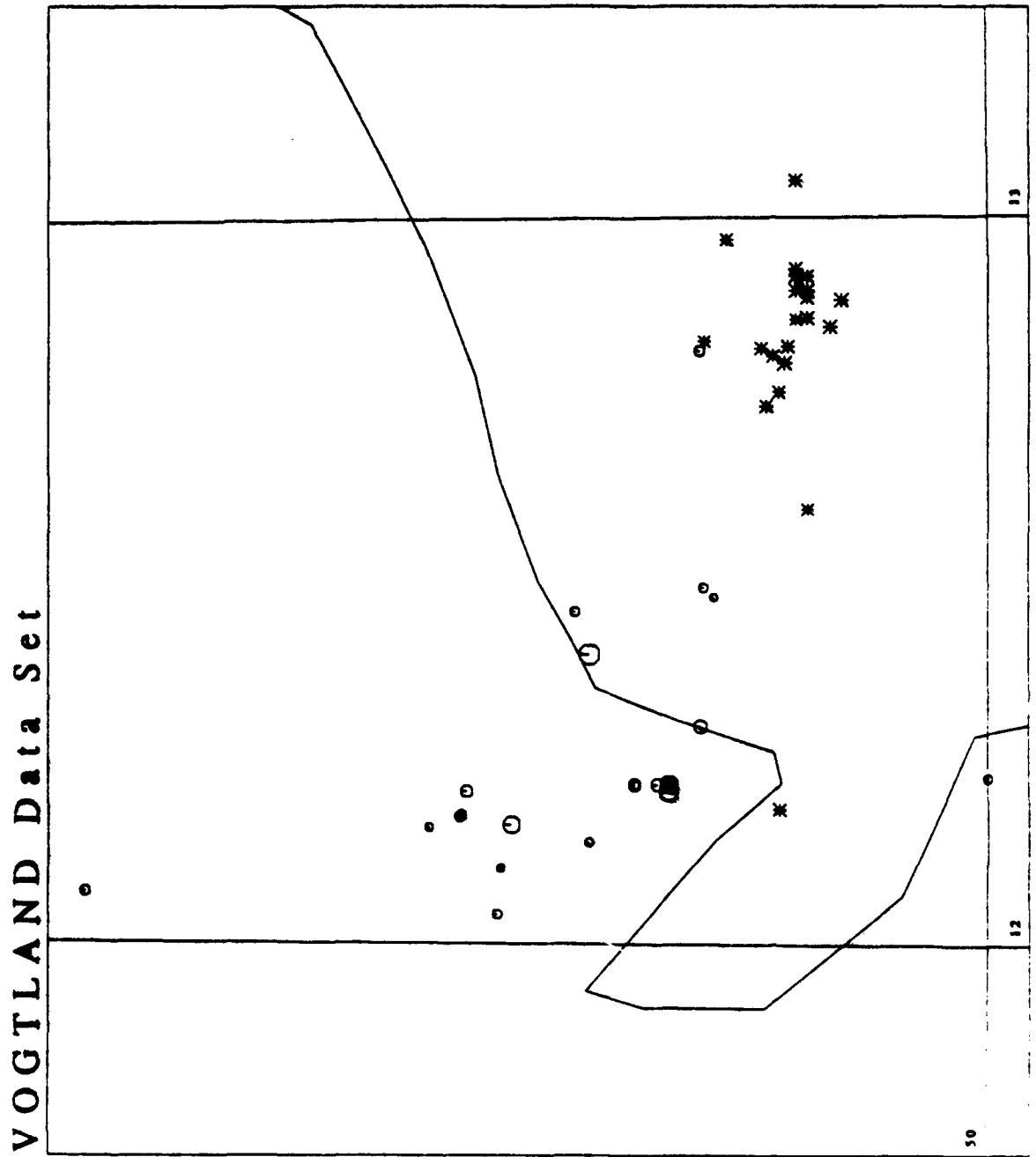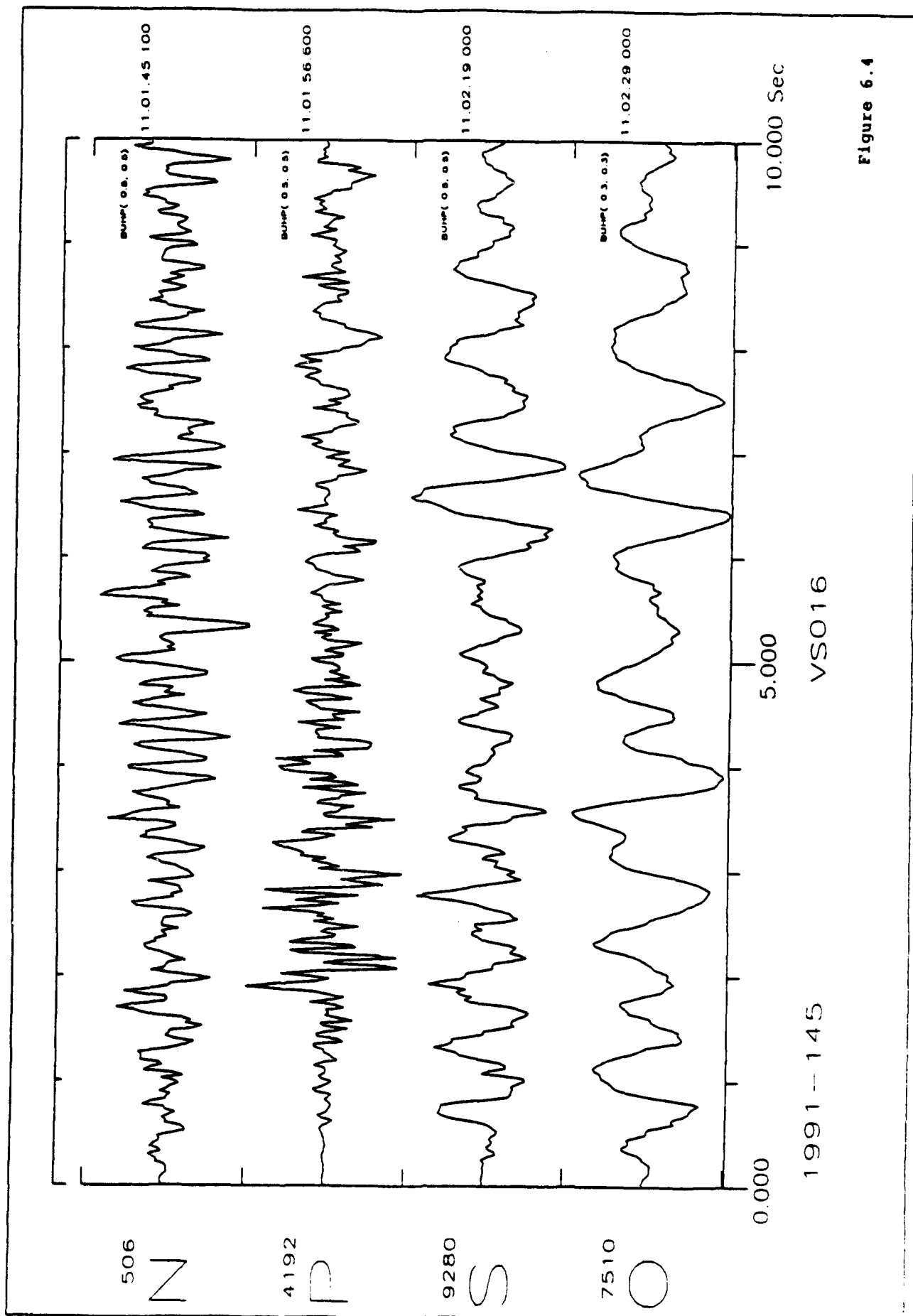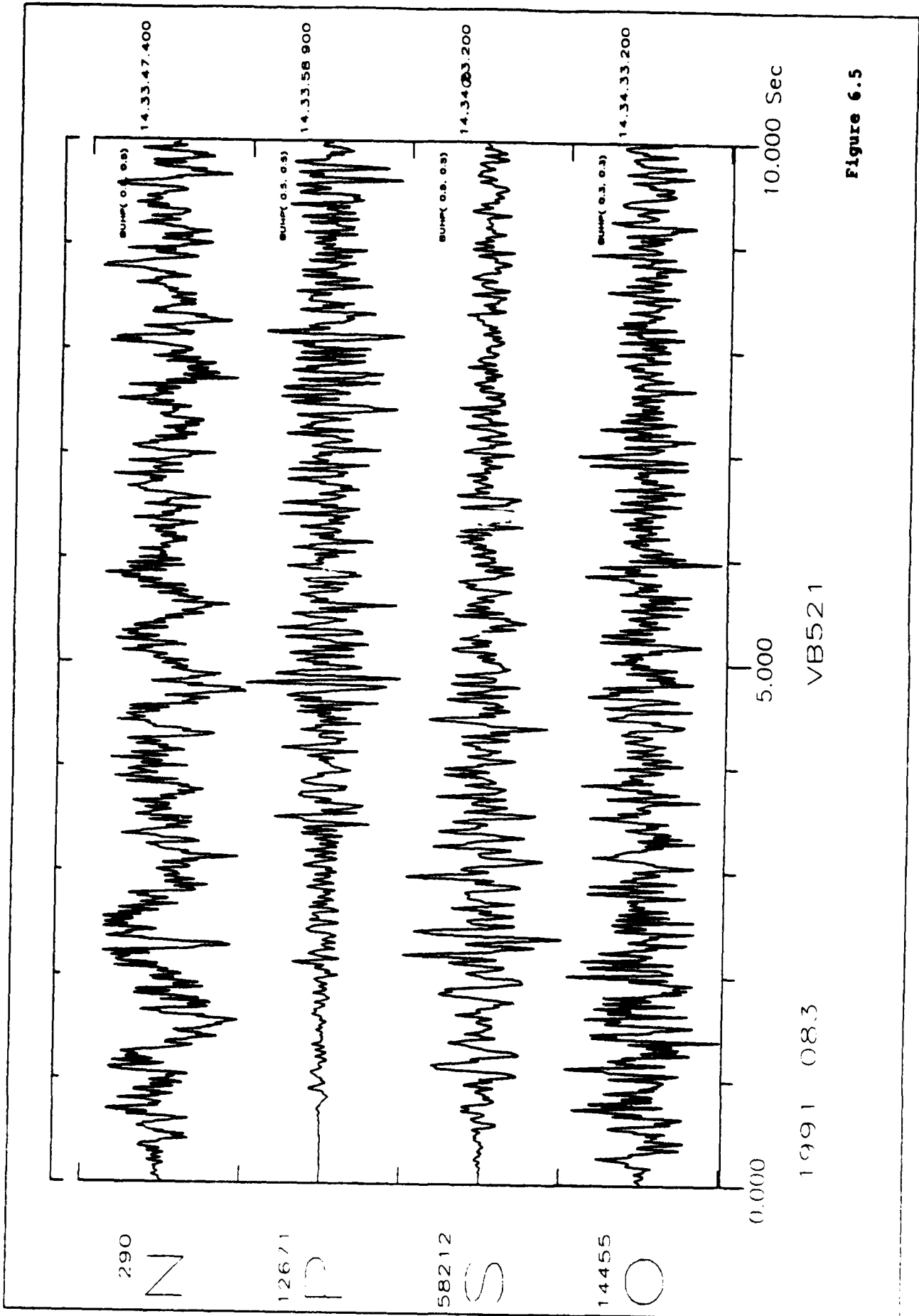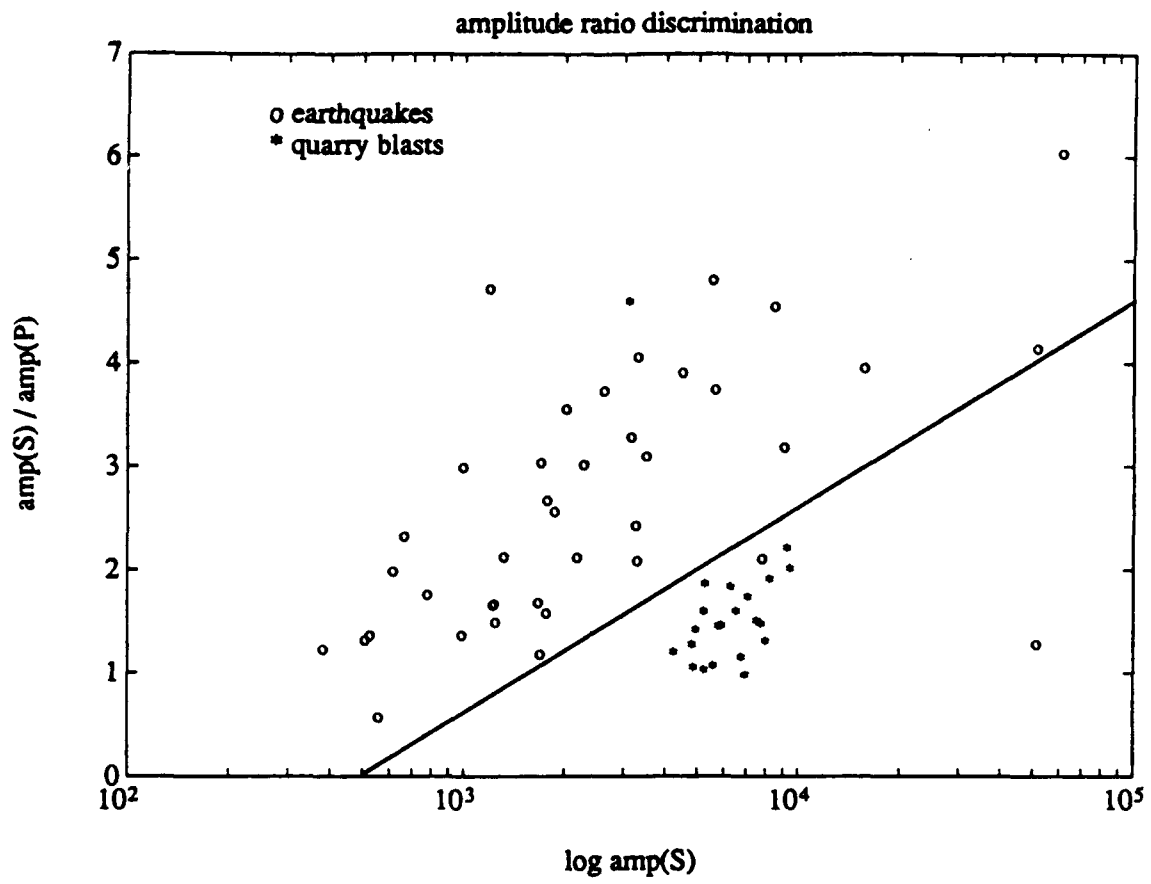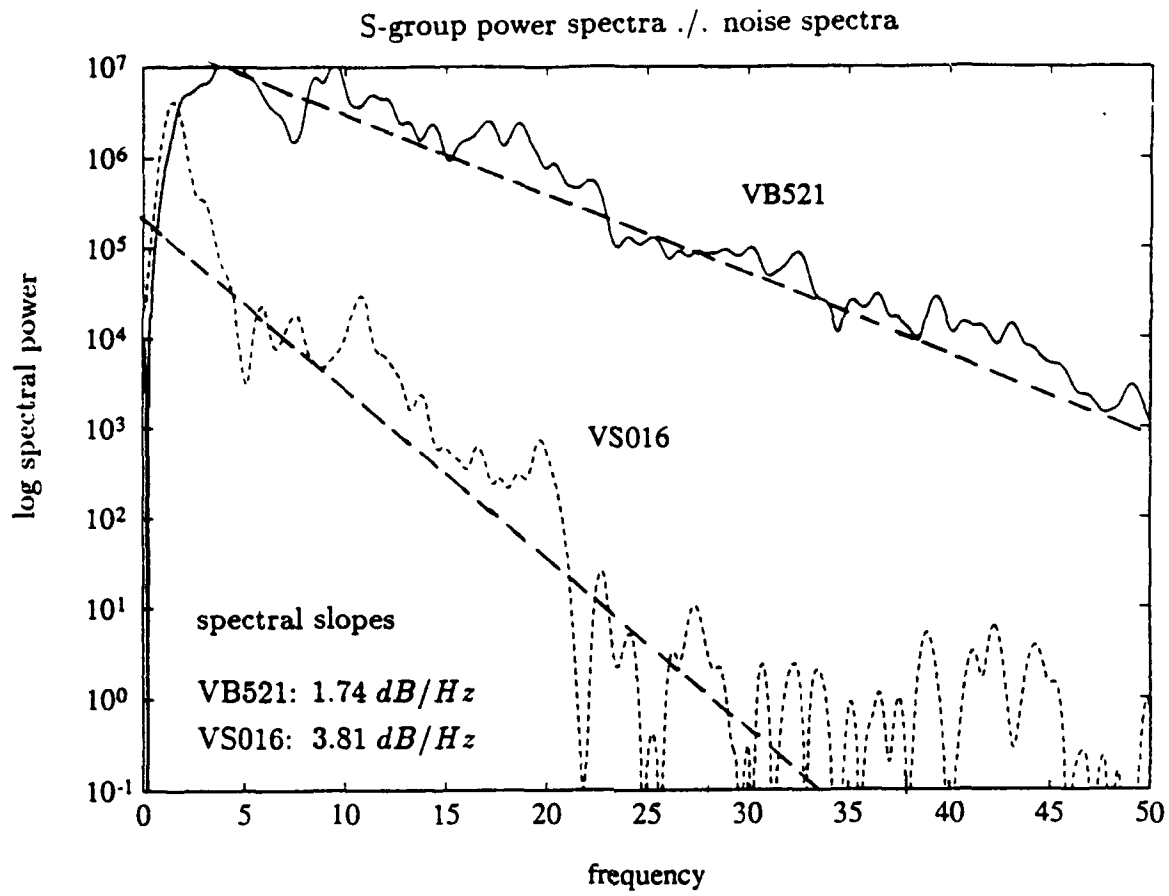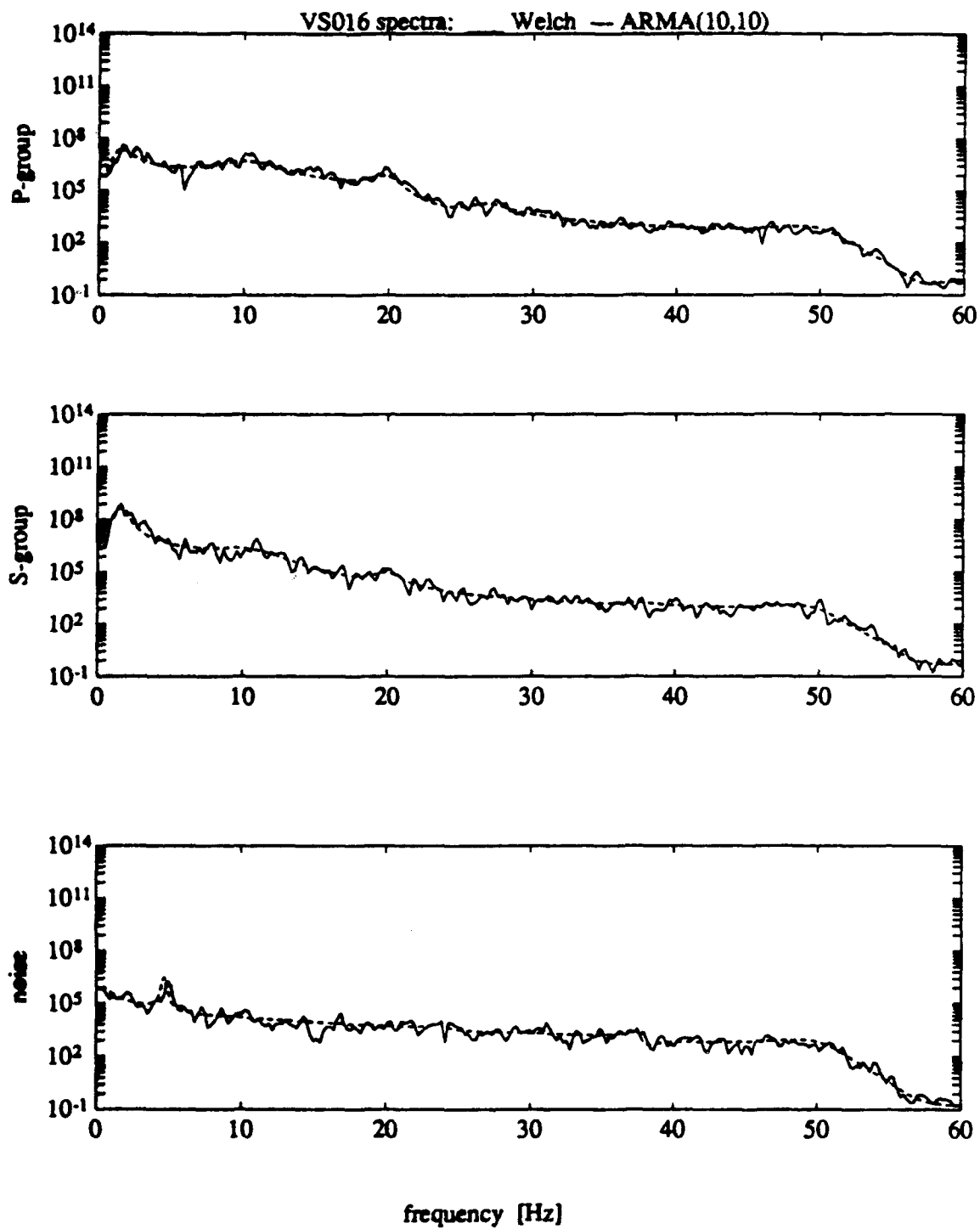

Figure 6.8

Figure 6.9

VB521, ARMA(10,10)

Figure 6.10a

SS model order selection

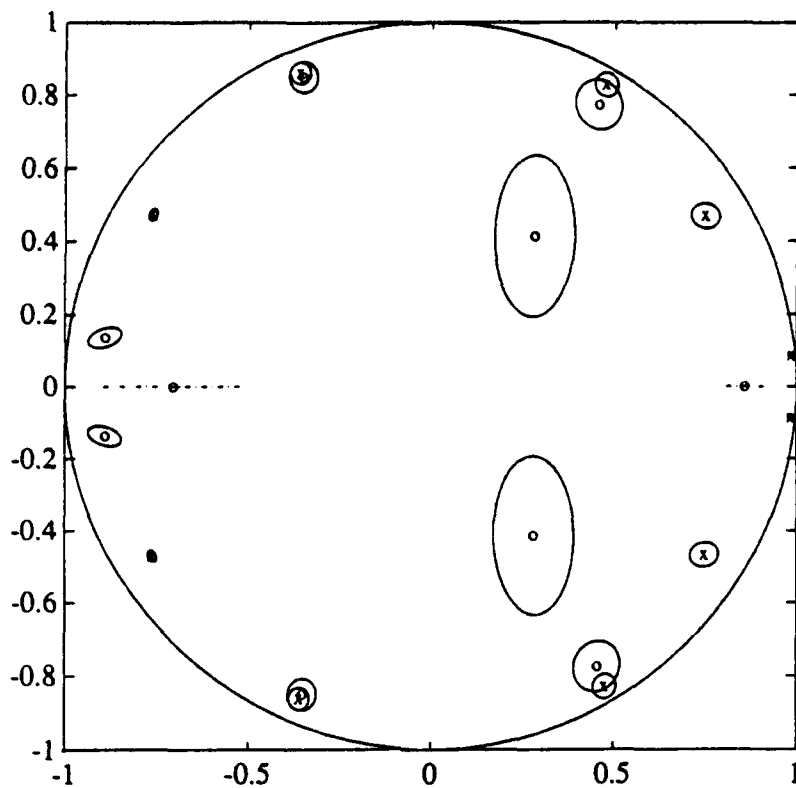
Figure 6.10b

no. of AR-parameters

comparing S-group spectra

comparing S-group ARMA(3,1)-models

frequency [Hz]

Figure 6.11

Figure 6.12

combined discrimination

combined discrimination

Figure 6.13

UNFILTERED

4910

BUMP:20.0.20.0)

2002

FILTERED WITH HP 20 HZ

1991 O73:12.03.00.000   GEC2B.sz

145.000   150.000   155.000 Sec

VS003

Figure 6.14

Figure 6.15

SONOGRAM-Detector

quit | move window | auto-move | [ ] | patternbase | new trace | new data

transfer: • Fourier half...
display : • log(psd-noise...
basestep: • log2
blanking: • mean + varia...
scaling : • prewhitened

25.05.91 11:01:00   11:01:30   11:02:00   11:02:30   11:03:00   11:03:30

actual para...

15.0 Hz

0.3 Hz

dynamic range in log2...

colormap: color
2Dfilter: • none

GEC2A sz

1000nm/sec I

f_up: none
f_lo: none

gain: 1.0

25.05.91 11:01:00   11:01:30   11:02:00   11:02:30   11:03:00   11:03:30

24.

STA/LTA

f_up: 4.0 Hz thre: 2.5
f_lo: 1.0 Hz lta+: slu
STA : 50 smp rise: 2 5
LTA : 50 STA fall: 2 5

```
h|-----rsqpponpooomopprqoooonlmlllmkklkkhikjjhkjjihjjhi.hh
h|-----sqpooonnmnnoooopppopnmnlmmkljkkkikiijji.jjji..jjji..
i|-----qqqmknmnnomnnprrronnmnnmlnjlkkllkkkk.k.jkjjkl.l..ki
m|-----no.pm......n.oppqqpo.o..m..n.n..n....m.o.nnno.o.on.
i|-----qqqqpponpooloptttrqrpqpqoonmlkmkl..lnkjlmm.mkj.kkll
j|-----rrnprqppo.nmnqsusssrrqrqpqqllnno.nolnlnmmmmmkk.lm.k
i|-----qrnqrponqkpooovuvTWTUVtvtuqsprrppoqooqpjmoomljmmpln
i|-----qqnoqponplooplttqSWVrUuusssprqnrlqrrojkjomlllk.nkm
h|-----nnmnponnnnjoomqqprUUqtvuuvuusutrtrqpropolqkmomnoonj
j|-----klllom.mlkkmnmnppors.stvrvttqutrrrroqppnnpm.noopook
j|-----.....m.lmi..lm.jklkmnpoqrrqqppqqpnopooojnml.mjnk.nn.
```

Figure 6.16
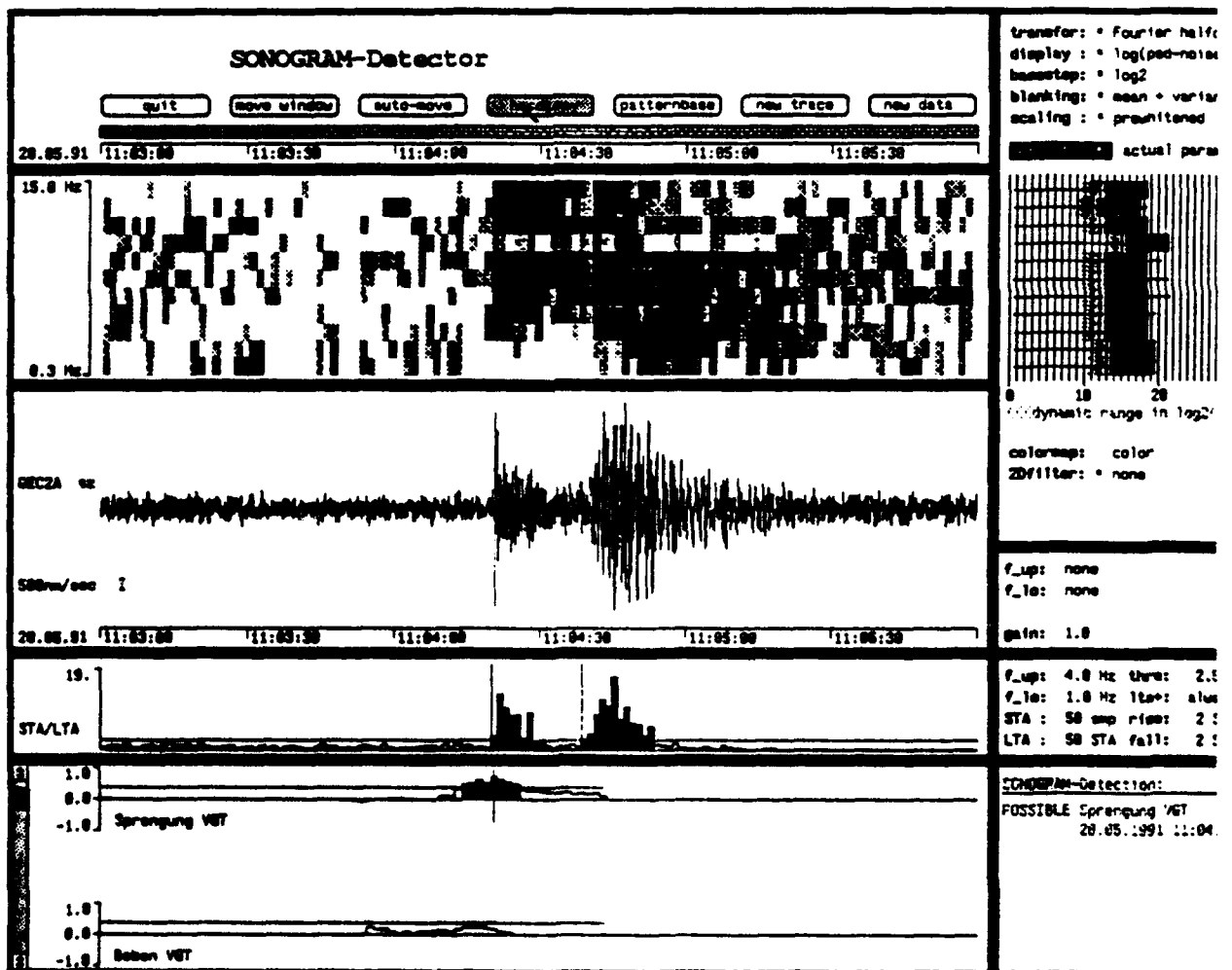
Figure 6.17

sonogram of VB521

f = 0.4688 Hz

t = 99 sec

t = 1 sec

f = 60 Hz

contours of spectral amplitude

seismogram trace

frequency [Hz]

time [sec]
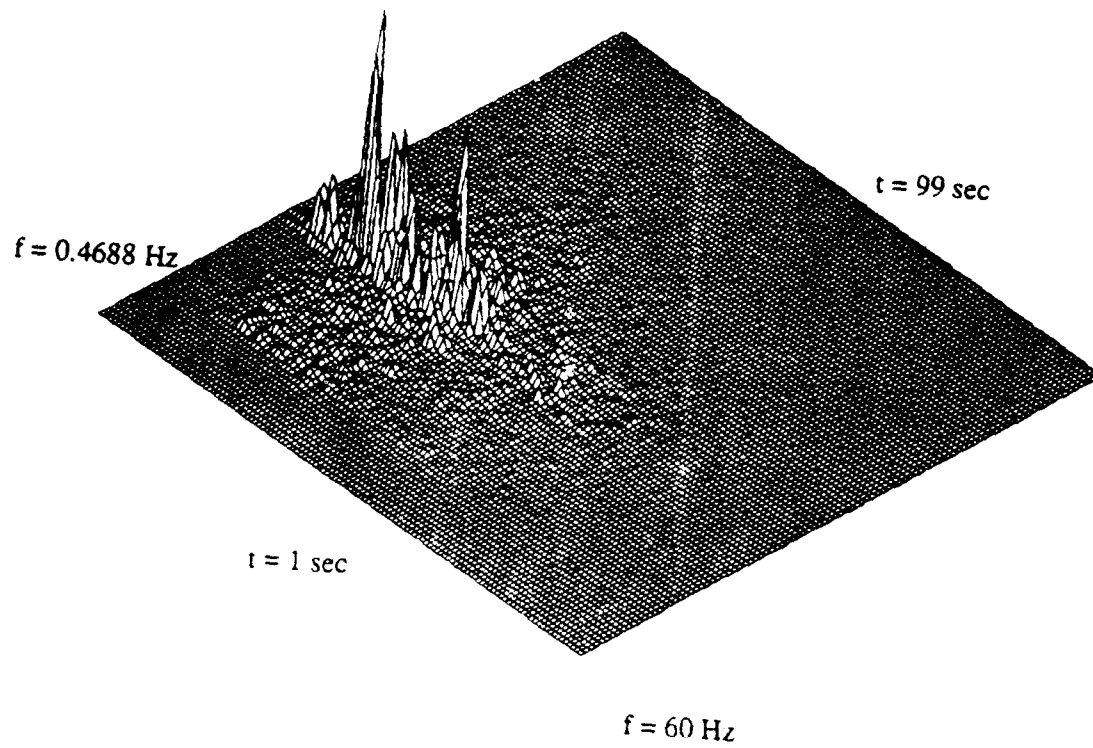
Figure 6.18

sonogram of VS016

f = 0.4688 Hz

t = 99 sec

t = 1 sec

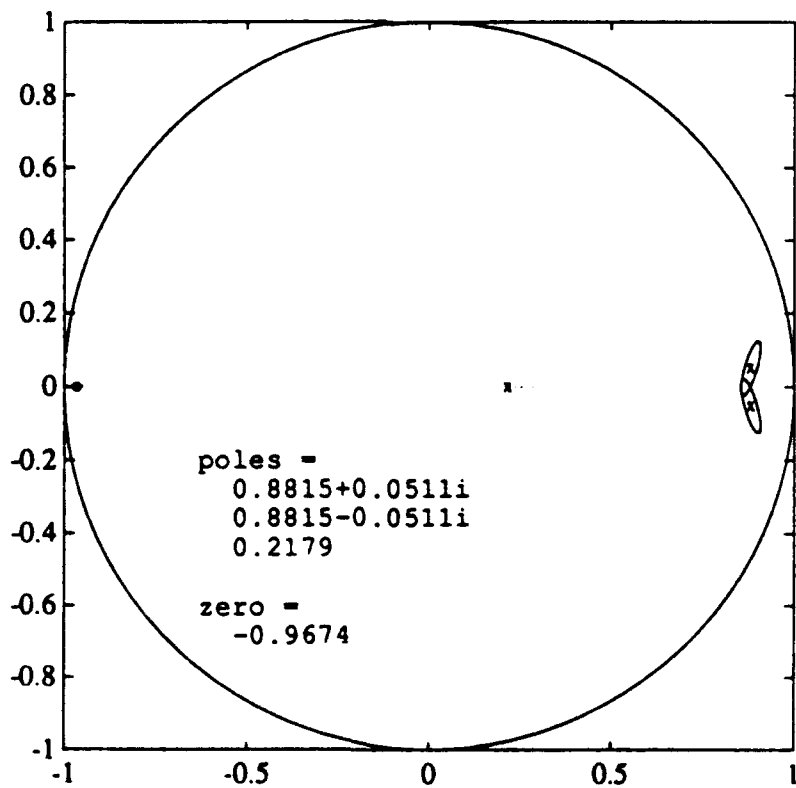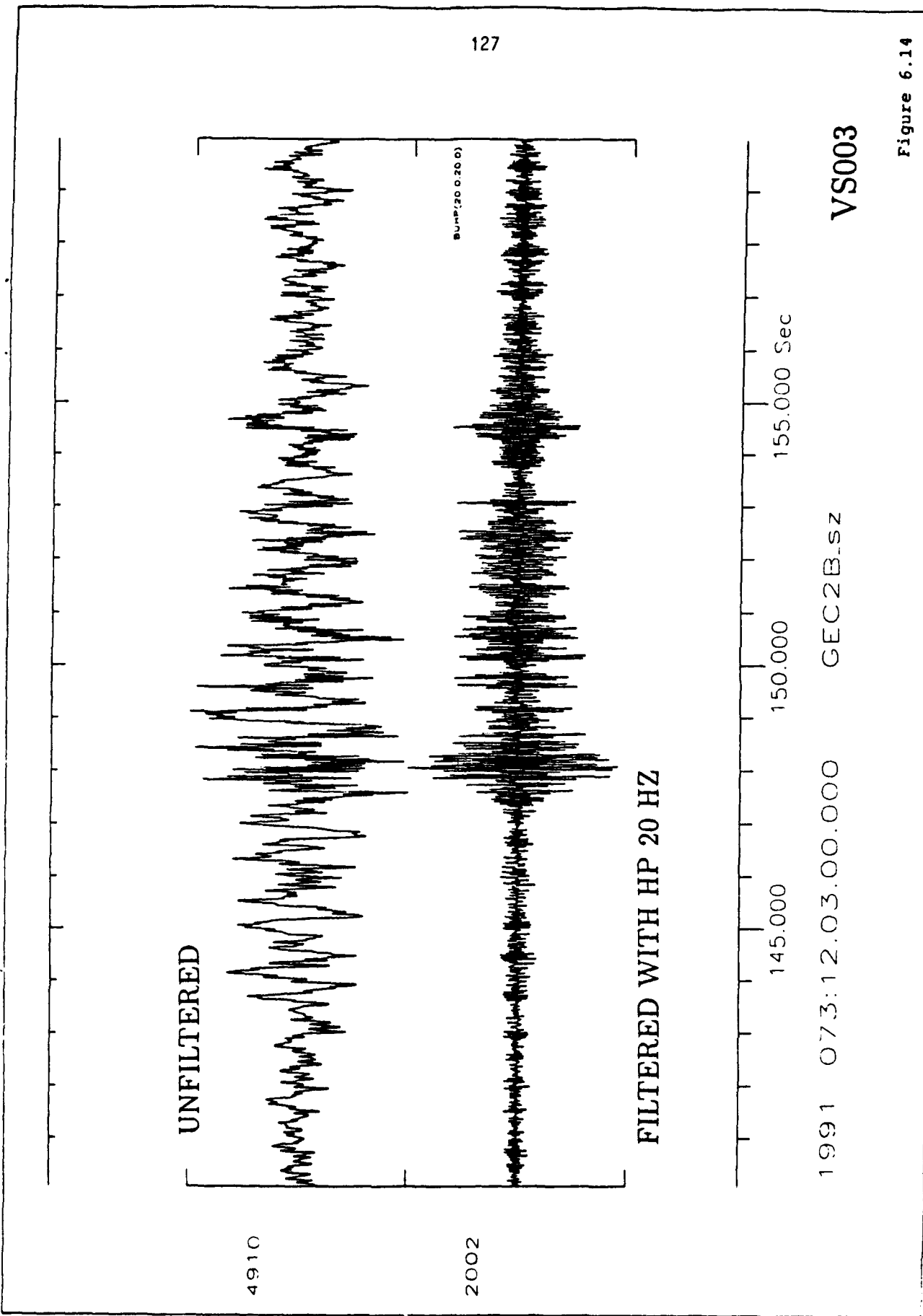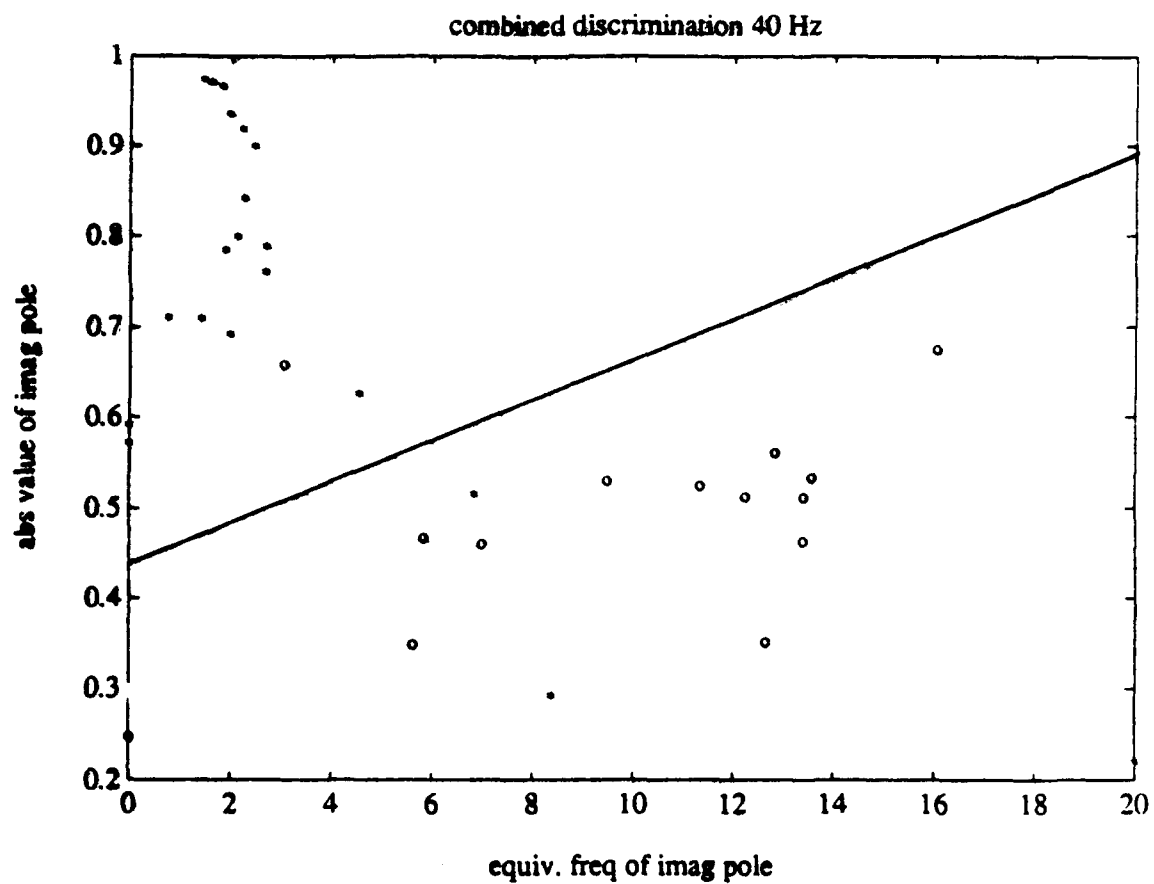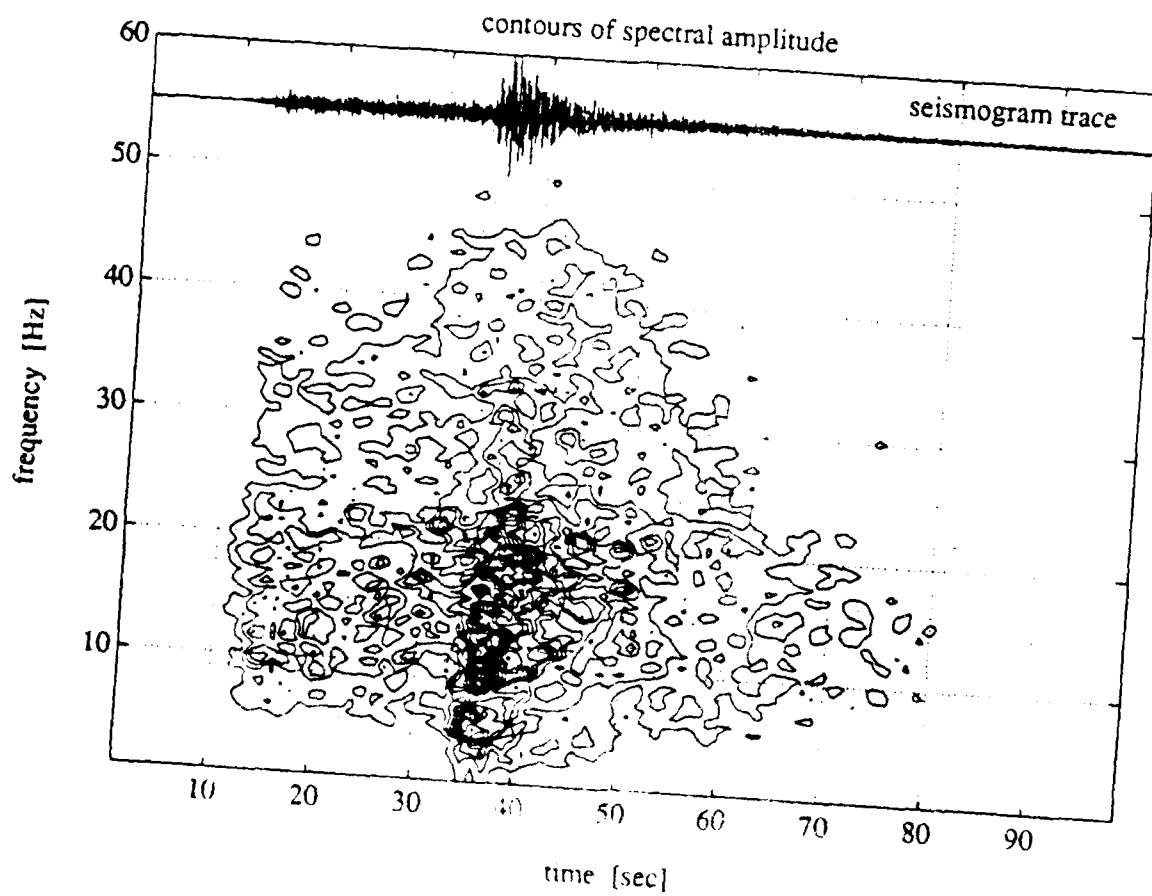f = 60 Hz

contours of spectral amplitude

seismogram trace

frequency [Hz]

time [sec]
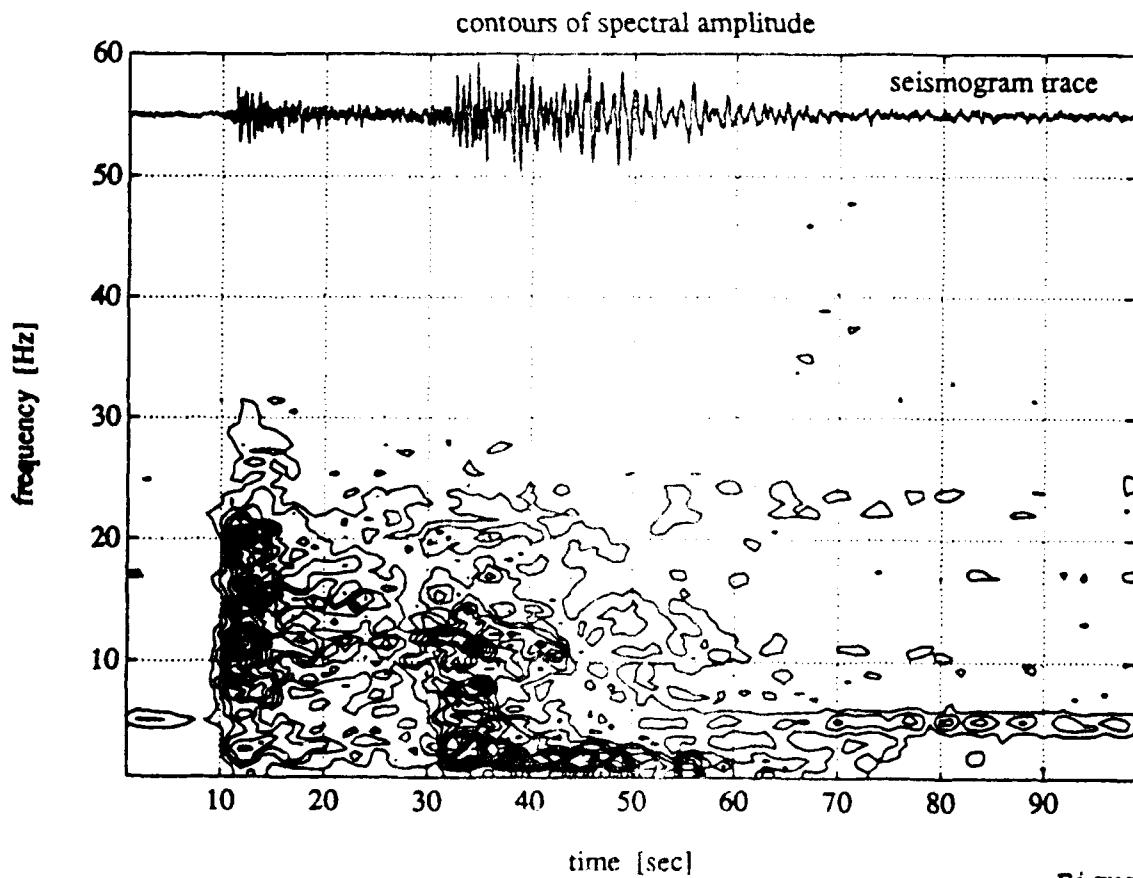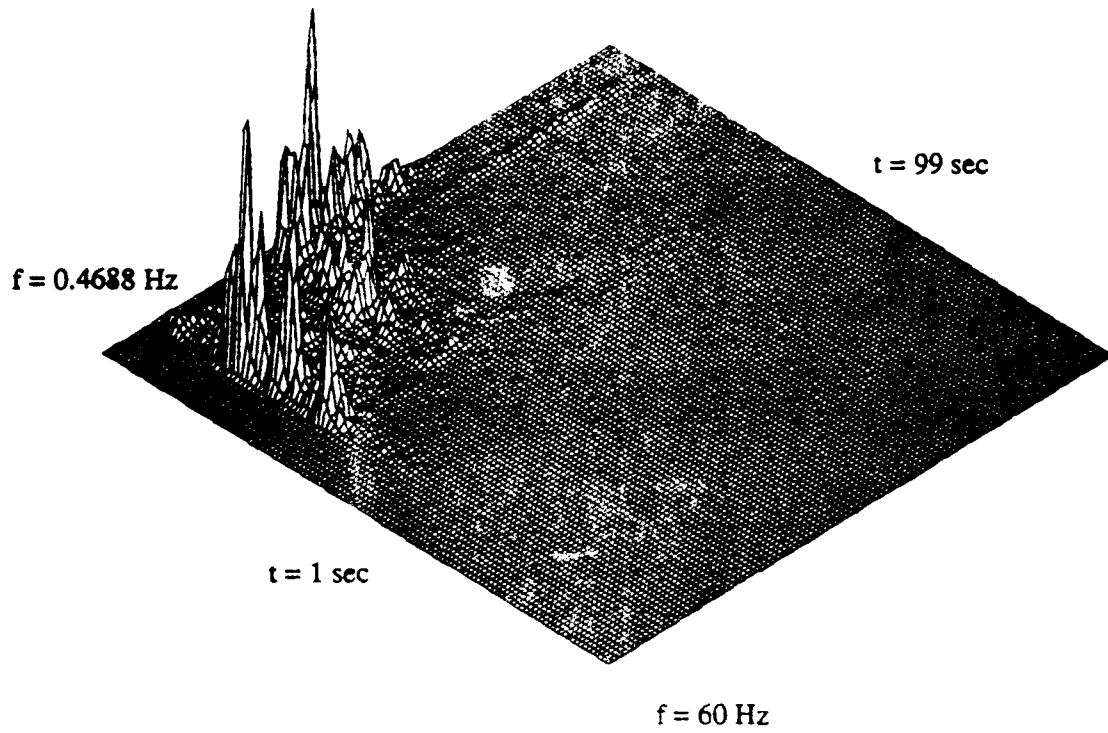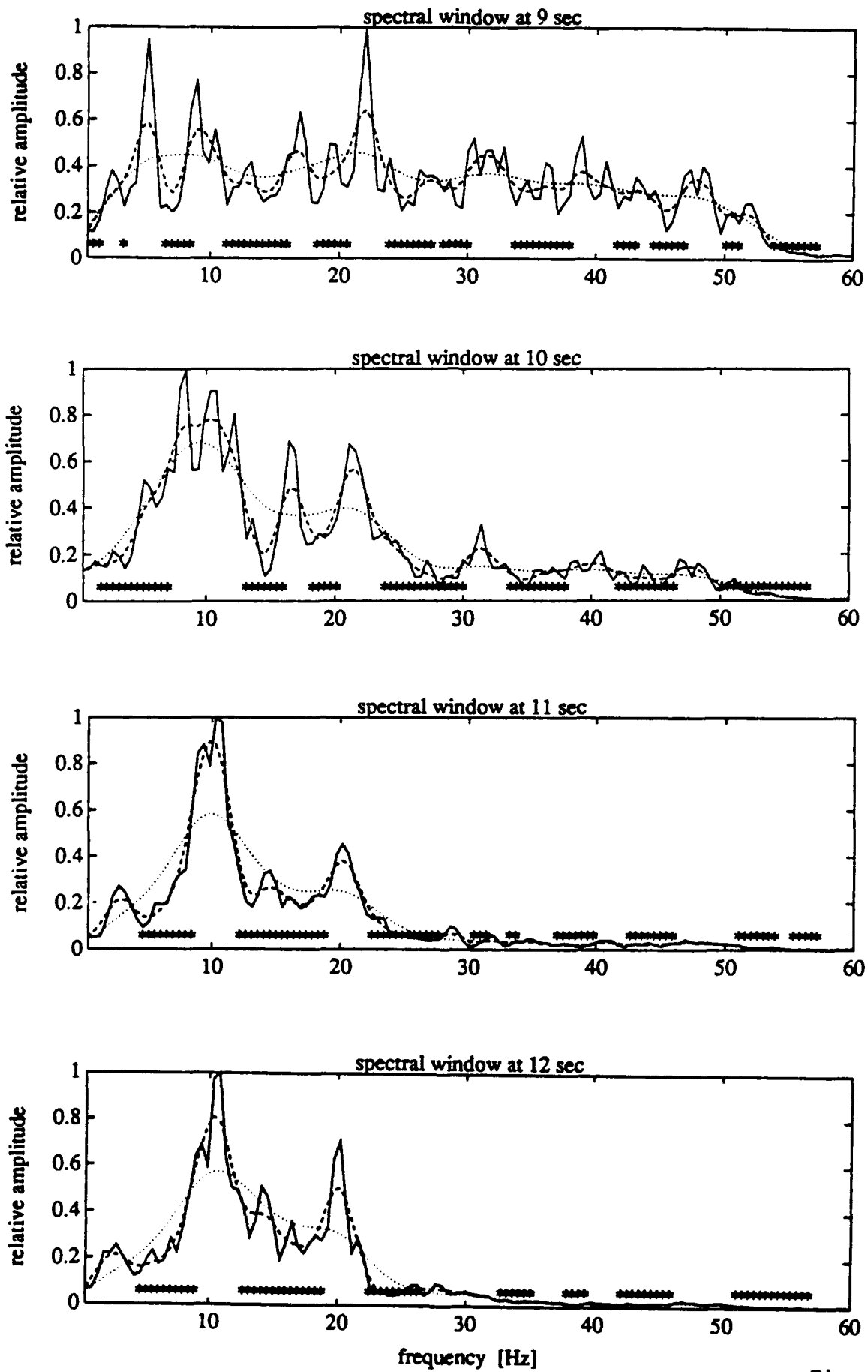
Figure 6.19

Figure 6.20

Figure 6.21

135
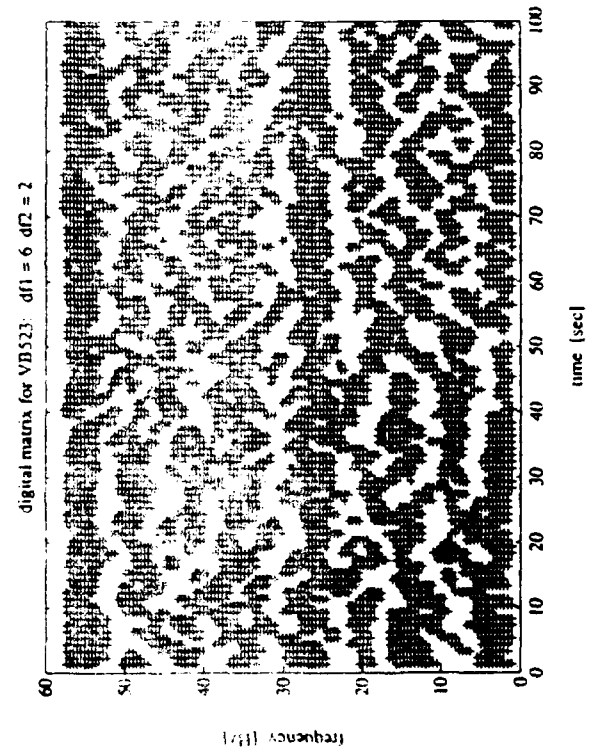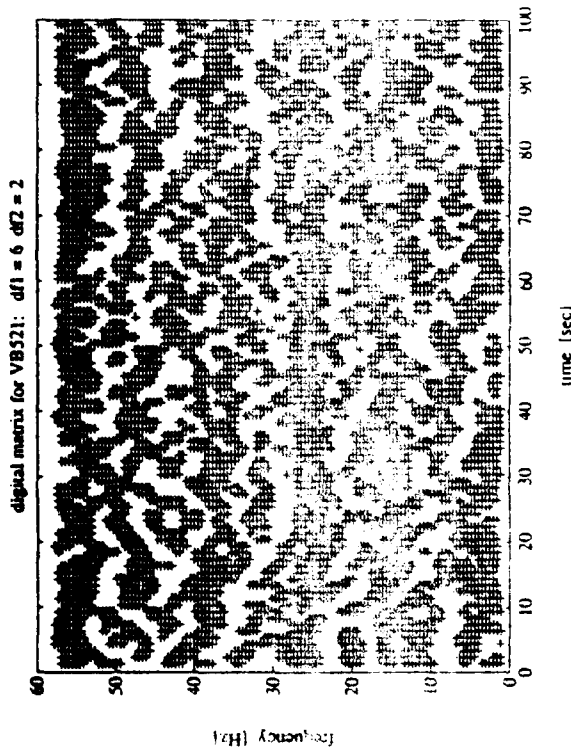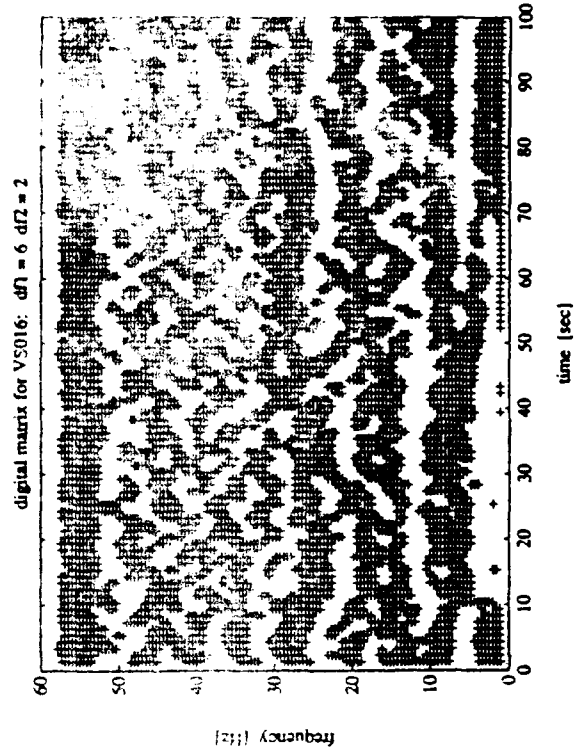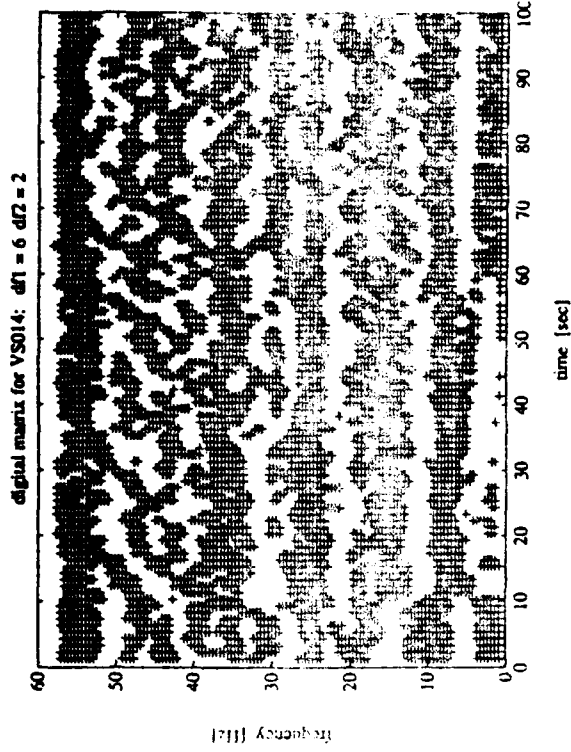
Event		Discriminants					Result	
#	M_L	S/P	S/O	ARMA	Sono	Str	vote	verdict
VB504	1.3	o	o	-	-	o	3:0	quake
VB505	1.3	o	o	-	-	o	3:0	quake
VB506	1.1	o	o	-	-	o	3:0	quake
VB507	2.4	o	*	o	o	-	3:1	quake
VB508	1.5	o	o	-	-	o	3:0	quake
VB509	1.1	-	o	-	o	-	2:0	quake
VB510	1.1	-	o	-	o	-	2:0	quake
VB511	1.7	o	o	o	o	o	5:0	quake
VB512	1.1	o	o	-	-	o	3:0	quake
VB513	1.5	o	o	-	o	o	4:0	quake
VB514	1.9	*	o	o	o	o	4:1	quake
VB515	1.3	o	o	-	o	-	3:0	quake
VB516	2.6	o	o	*	o	o	4:1	quake
VB517	1.6	o	o	-	o	o	4:0	quake
VB518	1.5	o	*	-	o	o	3:1	quake
VB519	1.3	-	o	-	o	-	2:0	quake
VB520	1.8	o	o	o	o	o	5:0	quake
VB521	3.0	o	o	o	o	o	5:0	quake
VB522	1.3	-	o	-	-	-	1:0	quake
VB523	2.1	o	o	o	o	o	5:0	quake
VB524	1.9	o	o	o	o	o	5:0	quake
VB525	1.4	o	o	-	o	o	4:0	quake
VB526	2.6	o	o	o	o	o	5:0	quake
VB527	1.8	o	o	o	o	o	5:0	quake
VB528	1.8	o	o	o	o	o	5:0	quake
VB529	1.5	o	o	-	o	o	4:0	quake
VB530	1.3	o	o	-	o	o	4:0	quake
VB531	1.4	o	o	-	o	o	4:0	quake
VB532	1.7	o	o	o	o	o	5:0	quake
VB533	1.8	o	o	o	o	o	5:0	quake
VB534	1.3	-	o	-	o	o	3:0	quake
VB535	1.4	o	o	-	o	o	4:0	quake
VB536	1.1	o	o	-	o	o	4:0	quake
VB537	1.4	-	o	-	o	-	2:0	quake
VB538	2.9	*	*	o	o	o	3:2	quake
VB539	1.3	o	o	-	o	o	4:0	quake
VB540	0.7	o	o	-	-	o	3:0	quake
VB541	0.9	-	o	-	o	-	2:0	quake
VB542	1.2	-	o	-	o	o	3:0	quake

Table 6.2a

136

Event		Discriminants					Result	
#	M_L	S/P	S/O	ARMA	Sono	Str	vote	verdict
VS001b	2.0	*	*	*	o	*	1:4	blast
VS003	1.8	*	*	o	?	*	1:3	blast
VS004	1.9	*	*	o	*	*	1:4	blast
VS005	2.0	*	*	*	*	*	0:5	blast
VS006	1.9	*	*	*	*	*	0:5	blast
VS007	2.1	*	*	*	*	*	0:5	blast
VS008	1.9	*	*	?	?	o	1:2	blast
VS009	2.0	*	*	*	*	*	0:5	blast
VS010	2.0	*	*	*	*	*	0:5	blast
VS011	1.8	*	o	o	o	*	3:2	quake!
VS012	1.9	*	*	*	*	*	0:5	blast
VS013	2.0	o	*	*	*	-	1:3	blast
VS014	2.0	*	*	?	?	*	0:3	blast
VS015a	2.1	*	*	*	*	*	0:5	blast
VS016	2.1	*	*	*	*	*	0:5	blast
VS017	2.1	*	*	*	*	*	0:5	blast
VS018	2.0	*	*	*	*	*	0:5	blast
VS019	2.1	*	*	*	*	*	0:5	blast
VS020	1.9	*	*	*	*	*	0:5	blast
VS021	1.8	*	o	*	?	*	1:3	blast
VS022	2.2	*	*	*	*	*	0:5	blast
VS023	1.9	*	*	*	*	o	1:4	blast

Table 6.2b

Prof. Thomas Ahrens
Seismological Lab, 252-21
Division of Geological & Planetary Sciences
California Institute of Technology
Pasadena, CA 91125

Prof. Keiiti Aki
Center for Earth Sciences
University of Southern California
University Park
Los Angeles, CA 90089-0741

Prof. Shelton Alexander
Geosciences Department
403 Deike Building
The Pennsylvania State University
University Park, PA 16802

Dr. Ralph Alewine, III
DARPA/NMRO
3701 North Fairfax Drive
Arlington, VA 22203-1714

Prof. Charles B. Archambeau
CIRES
University of Colorado
Boulder, CO 80309

Dr. Thomas C. Bache, Jr.
Science Applications Int'l Corp.
10260 Campus Point Drive
San Diego, CA 92121 (2 copies)

Prof. Muawia Barazangi
Institute for the Study of the Continent
Cornell University
Ithaca, NY 14853

Dr. Jeff Barker
Department of Geological Sciences .
State University of New York
 at Binghamton
Vestal, NY 13901

Dr. Douglas R. Baumgardt
ENSCO, Inc
5400 Port Royal Road
Springfield, VA 22151-2388

Dr. Susan Beck
Department of Geosciences
Building #77
University of Arizona
Tuscon, AZ 85721

Dr. T.J. Bennett
S-CUBED
A Division of Maxwell Laboratories
11800 Sunrise Valley Drive, Suite 1212
Reston, VA 22091

Dr. Robert Blandford
AFTAC/TT, Center for Seismic Studies
1300 North 17th Street
Suite 1450
Arlington, VA 22209-2308

Dr. G.A. Bollinger
Department of Geological Sciences
Virginia Polytechnical Institute
21044 Derring Hall
Blacksburg, VA 24061

Dr. Stephen Bratt
Center for Seismic Studies
1300 North 17th Street
Suite 1450
Arlington, VA 22209-2308

Dr. Lawrence Burdick
Woodward-Clyde Consultants
566 El Dorado Street
Pasadena, CA 91109-3245

Dr. Robert Burridge
Schlumberger-Doll Research Center
Old Quarry Road
Ridgefield, CT 06877

Dr. Jerry Carter
Center for Seismic Studies
1300 North 17th Street
Suite 1450
Arlington, VA 22209-2308

Dr. Eric Chael
Division 9241
Sandia Laboratory
Albuquerque, NM 87185

Prof. Vernon F. Cormier
Department of Geology & Geophysics
U-45, Room 207
University of Connecticut
Storrs, CT 06268

Prof. Steven Day
Department of Geological Sciences
San Diego State University
San Diego, CA 92182

1

Marvin Denny
U.S. Department of Energy
Office of Arms Control
Washington, DC 20585

Dr. Zoltan Der
ENSCO, Inc.
5400 Port Royal Road
Springfield, VA 22151-2388

Prof. Adam Dziewonski
Hoffman Laboratory, Harvard University
Dept. of Earth Atmos. & Planetary Sciences
20 Oxford Street
Cambridge, MA 02138

Prof. John Ebel
Department of Geology & Geophysics
Boston College
Chestnut Hill, MA 02167

Eric Fielding
SNEE Hall
INSTOC
Cornell University
Ithaca, NY 14853

Dr. Mark D. Fisk
Mission Research Corporation
735 State Street
P.O. Drawer 719
Santa Barbara, CA 93102

Prof Stanley Flatte
Applied Sciences Building
University of California, Santa Cruz
Santa Cruz, CA 95064

Dr. John Foley
NER-Geo Sciences
1100 Crown Colony Drive
Quincy, MA 02169

Prof. Donald Forsyth
Department of Geological Sciences
Brown University
Providence, RI 02912

Dr. Art Frankel
U.S. Geological Survey
922 National Center
Reston, VA 22092

Dr. Cliff Frolich
Institute of Geophysics
8701 North Mopac
Austin, TX 78759

Dr. Holly Given
IGPP, A-025
Scripps Institute of Oceanography
University of California, San Diego
La Jolla, CA 92093

Dr. Jeffrey W. Given
SAIC
10260 Campus Point Drive
San Diego, CA 92121

Dr. Dale Glover
Defense Intelligence Agency
ATTN: ODT-1B
Washington, DC 20301

Dr. Indra Gupta
Teledyne Geotech
314 Montgomery Street
Alexanderia, VA 22314

Dan N. Hagedon
Pacific Northwest Laboratories
Battelle Boulevard
Richland, WA 99352

Dr. James Hannon
Lawrence Livermore National Laboratory
P.O. Box 808
L-205
Livermore, CA 94550

Dr. Roger Hansen
HQ AFTAC/TTR
Patrick AFB, FL 32925-6001

Prof. David G. Harkrider
Seismological Laboratory
Division of Geological & Planetary Sciences
California Institute of Technology
Pasadena, CA 91125

Prof. Danny Harvey
CIRES
University of Colorado
Boulder, CO 80309

Prof. Donald V. Helmberger
Seismological Laboratory
Division of Geological & Planetary Sciences
California Institute of Technology
Pasadena, CA 91125

Prof. Eugene Herrin
Institute for the Study of Earth and Man
Geophysical Laboratory
Southern Methodist University
Dallas, TX 75275

Prof. Robert B. Herrmann
Department of Earth & Atmospheric Sciences
St. Louis University
St. Louis, MO 63156

Prof. Lane R. Johnson
Seismographic Station
University of California
Berkeley, CA 94720

Prof. Thomas H. Jordan
Department of Earth, Atmospheric &
  Planetary Sciences
Massachusetts Institute of Technology
Cambridge, MA 02139

Prof. Alan Kafka
Department of Geology & Geophysics
Boston College
Chestnut Hill, MA 02167

Robert C. Kemerait
ENSCO, Inc.
445 Pineda Court
Melbourne, FL 32940

Dr. Max Koontz
U.S. Dept. of Energy/DP 5
Forrestal Building
1000 Independence Avenue
Washington, DC 20585

Dr. Richard LaCoss
MIT Lincoln Laboratory, M-200B
P.O. Box 73
Lexington, MA 02173-0073

Dr. Fred K. Lamb
University of Illinois at Urbana-Champaign
Department of Physics
1110 West Green Street
Urbana, IL 61801

Prof. Charles A. Langston
Geosciences Department
403 Deike Building
The Pennsylvania State University
University Park, PA 16802

Jim Lawson, Chief Geophysicist
Oklahoma Geological Survey
Oklahoma Geophysical Observatory
P.O. Box 8
Leonard, OK 74043-0008

Prof. Thorne Lay
Institute of Tectonics
Earth Science Board
University of California, Santa Cruz
Santa Cruz, CA 95064

Dr. William Leith
U.S. Geological Survey
Mail Stop 928
Reston, VA 22092

Mr. James F. Lewkowicz
Phillips Laboratory/GPEH
Hanscom AFB, MA 01731-5000(2 copies)

Mr. Alfred Lieberman
ACDA/VI-OA State Department Building
Room 5726
320-21st Street, NW
Washington, DC 20451

Prof. L. Timothy Long
School of Geophysical Sciences
Georgia Institute of Technology
Atlanta, GA 30332

Dr. Randolph Martin, III
New England Research, Inc.
76 Olcott Drive
White River Junction, VT 05001

Dr. Robert Masse
Denver Federal Building
Box 25046, Mail Stop 967
Denver, CO 80225

Dr. Gary McCartor
Department of Physics
Southern Methodist University
Dallas, TX 75275

3

Prof. Thomas V. McEvilly
Seismographic Station
University of California
Berkeley, CA 94720

Dr. Art McGarr
U.S. Geological Survey
Mail Stop 977
U.S. Geological Survey
Menlo Park, CA 94025

Dr. Keith L. McLaughlin
S-CUBED
A Division of Maxwell Laboratory
P.O. Box 1620
La Jolla, CA 92038-1620

Stephen Miller & Dr. Alexander Florence
SRI International
333 Ravenswood Avenue
Box AF 116
Menlo Park, CA 94025-3493

Prof. Bernard Minster
IGPP, A-025
Scripps Institute of Oceanography
University of California, San Diego
La Jolla, CA 92093

Prof. Brian J. Mitchell
Department of Earth & Atmospheric Sciences
St. Louis University
St. Louis, MO 63156

Mr. Jack Murphy
S-CUBED
A Division of Maxwell Laboratory
11800 Sunrise Valley Drive, Suite 1212
Reston, VA 22091 (2 Copies)

Dr. Keith K. Nakanishi
Lawrence Livermore National Laboratory
L-025
P.O. Box 808
Livermore, CA 94550

Dr. Carl Newton
Los Alamos National Laboratory
P.O. Box 1663
Mail Stop C335, Group ESS-3
Los Alamos, NM 87545

Dr. Bao Nguyen
HQ AFTAC/TTR
Patrick AFB, FL 32925-6001

Prof. John A. Orcutt
IGPP, A-025
Scripps Institute of Oceanography
University of California, San Diego
La Jolla, CA 92093

Prof. Jeffrey Park
Kline Geology Laboratory
P.O. Box 6666
New Haven, CT 06511-8130

Dr. Howard Patton
Lawrence Livermore National Laboratory
L-025
P.O. Box 808
Livermore, CA 94550

Dr. Frank Pilotte
HQ AFTAC/TT
Patrick AFB, FL 32925-6001

Dr. Jay J. Pulli
Radix Systems, Inc.
2 Taft Court, Suite 203
Rockville, MD 20850

Dr. Robert Reinke
ATTN: FCTVTD
Field Command
Defense Nuclear Agency
Kirtland AFB, NM 87115

Prof. Paul G. Richards
Lamont-Doherty Geological Observatory
of Columbia University
Palisades, NY 10964

Mr. Wilmer Rivers
Teledyne Geotech
314 Montgomery Street
Alexandria, VA 22314

Dr. George Rothe
HQ AFTAC/TTR
Patrick AFB, FL 32925-6001

Dr. Alan S. Ryall, Jr.
DARPA/NMRO
3701 North Fairfax Drive
Arlington, VA 22209-1714

Dr. Richard Sailor
TASC, Inc.
55 Walkers Brook Drive
Reading, MA 01867

Prof. Charles G. Sammis
Center for Earth Sciences
University of Southern California
University Park
Los Angeles, CA 90089-0741

Prof. Christopher H. Scholz
Lamont-Doherty Geological Observatory
 of Columbia University
Palisades, CA 10964

Dr. Susan Schwartz
Institute of Tectonics
1156 High Street
Santa Cruz, CA 95064

Secretary of the Air Force
(SAFRD)
Washington, DC 20330

Office of the Secretary of Defense
DDR&E
Washington, DC 20330

Thomas J. Sereno, Jr.
Science Application Int'l Corp.
10260 Campus Point Drive
San Diego, CA 92121

Dr. Michael Shore
Defense Nuclear Agency/SPSS
6801 Telegraph Road
Alexandria, VA 22310

Dr. Matthew Sibol
Virginia Tech
Seismological Observatory
4044 Derring Hall
Blacksburg, VA 24061-0420

Prof. David G. Simpson
IRIS, Inc.
1616 North Fort Myer Drive
Suite 1440
Arlington, VA 22209

Donald L. Springer
Lawrence Livermore National Laboratory
L-025
P.O. Box 808
Livermore, CA 94550

Dr. Jeffrey Stevens
S-CUBED
A Division of Maxwell Laboratory
P.O. Box 1620
La Jolla, CA 92038-1620

Lt. Col. Jim Stobie
ATTN: AFOSR/NL
Bolling AFB
Washington, DC 20332-6448

Prof. Brian Stump
Institute for the Study of Earth & Man
Geophysical Laboratory
Southern Methodist University
Dallas, TX 75275

Prof. Jeremiah Sullivan
University of Illinois at Urbana-Champaign
Department of Physics
1110 West Green Street
Urbana, IL 61801

Prof. L. Sykes
Lamont-Doherty Geological Observatory
 of Columbia University
Palisades, NY 10964

Dr. David Taylor
ENSCO, Inc.
445 Pineda Court
Melbourne, FL 32940

Dr. Steven R. Taylor
Los Alamos National Laboratory
P.O. Box 1663
Mail Stop C335
Los Alamos, NM 87545

Prof. Clifford Thurber
University of Wisconsin-Madison
Department of Geology & Geophysics
1215 West Dayton Street
Madison, WS 53706

Prof. M. Nafi Toksoz
Earth Resources Lab
Massachusetts Institute of Technology
42 Carleton Street
Cambridge, MA 02142

5

Dr. Larry Turnbull
CIA-OSWR/NED
Washington, DC 20505

DARPA/RMO/SECURITY OFFICE
3701 North Fairfax Drive
Arlington, VA 22203-1714

Dr. Gregory van der Vink
IRIS, Inc.
1616 North Fort Myer Drive
Suite 1440
Arlington, VA 22209

HQ DNA
ATTN: Technical Library
Washington, DC 20305

Dr. Karl Veith
EG&G
5211 Auth Road
Suite 240
Suitland, MD 20746

Defense Intelligence Agency
Directorate for Scientific & Technical Intelligence
ATTN: DTIB
Washington, DC 20340-6158

Prof. Terry C. Wallace
Department of Geosciences
Building #77
University of Arizona
Tuscon, AZ 85721

Defense Technical Information Center
Cameron Station
Alexandria, VA 22314 (2 Copies)

Dr. Thomas Weaver
Los Alamos National Laboratory
P.O. Box 1663
Mail Stop C335
Los Alamos, NM 87545

TACTEC
Battelle Memorial Institute
505 King Avenue
Columbus, OH 43201 (Final Report)

Dr. William Wortman
Mission Research Corporation
8560 Cinderbed Road
Suite 700
Newington, VA 22122

Phillips Laboratory
ATTN: XPG
Hanscom AFB, MA 01731-5000

Prof. Francis T. Wu
Department of Geological Sciences
State University of New York
 at Binghamton
Vestal, NY 13901

Phillips Laboratory
ATTN: GPE
Hanscom AFB, MA 01731-5000

AFTAC/CA
(STINFO)
Patrick AFB, FL 32925-6001

Phillips Laboratory
ATTN: TSML
Hanscom AFB, MA 01731-5000

DARPA/PM
3701 North Fairfax Drive
Arlington, VA 22203-1714

Phillips Laboratory
ATTN: SUL
Kirtland, NM 87117 (2 copies)

DARPA/RMO/RETRIEVAL
3701 North Fairfax Drive
Arlington, VA 22203-1714

Dr. Michel Bouchon
I.R.I.G.M.-B.P. 68
38402 St. Martin D'Heres
Cedex, FRANCE

6

Dr. Michel Campillo
Observatoire de Grenoble
I.R.I.G.M.-B.P. 53
38041 Grenoble, FRANCE

Dr. Jorg Schlittenhardt
Federal Institute for Geosciences & Nat'l Res.
Postfach 510153
D-3000 Hannover 51, GERMANY

Dr. Kin Yip Chun
Geophysics Division
Physics Department
University of Toronto
Ontario, CANADA

Dr. Johannes Schweitzer
Institute of Geophysics
Ruhr University/Bochum
P.O. Box 1102148
4360 Bochum 1, GERMANY

Prof. Hans-Peter Harjes
Institute for Geophysic
Ruhr University/Bochum
P.O. Box 102148
4630 Bochum 1, GERMANY

Prof. Eystein Husebye
NTNF/NORSAR
P.O. Box 51
N-2007 Kjeller, NORWAY

David Jepsen
Acting Head, Nuclear Monitoring Section
Bureau of Mineral Resources
Geology and Geophysics
G.P.O. Box 378, Canberra, AUSTRALIA

Ms. Eva Johannisson
Senior Research Officer
National Defense Research Inst.
P.O. Box 27322
S-102 54 Stockholm, SWEDEN

Dr. Peter Marshall
Procurement Executive
Ministry of Defense
Blacknest, Brimpton
Reading FG7-FRS, UNITED KINGDOM

Dr. Bernard Massinon, Dr. Pierre Mechler
Societe Radiomana
27 rue Claude Bernard
75005 Paris, FRANCE (2 Copies)

Dr. Svein Mykkeltveit
NTNT/NORSAR
P.O. Box 51
N-2007 Kjeller, NORWAY (3 Copies)

Prof. Keith Priestley
University of Cambridge
Bullard Labs, Dept. of Earth Sciences
Madingley Rise, Madingley Road
Cambridge CB3 OEZ, ENGLAND